University of Studies of Padua

Information Engineering Department
Master Degree in Electronic Engineering

Development of an integrated polarization, conditioning and acquisition system for large Langmuir probe arrays in cold plasmas

Advisor:

Prof. Nicolo' Marconato

Supervisor:

Dr. Roberto Cavazzana, PHD

Student:

Mattia Bevilacqua

ID Number 2087060

Academic Year 2023/2024

Abstract

Plasma physics and its related technological applications are a major research field of growing interest. Covering a broad range of aspects, from the most theoretical ones to the smallest practical case, the progress achieved up until now has been made possible due to both theoretical understanding, supported by the use of numerical simulation, and from the ability to direct measurements, carried out as accurately as possible, of plasma properties. One of the main driving forces that keeps pushing the research on plasmas and their properties, is the field of the long sought nuclear fusion as a source of clean, sustainable and practically unlimited energy. The constant evolution of the analog and digital electronics has enabled the design and realization of plasma diagnostic systems of increasing precision, resolution and quality. Thus the number of simultaneous measurements being needed to be processed increased as well, resulting in new challenging requirements. Nevertheless due to the nature of the plasma itself, which displays property rather different form the usually known states of matter, like temperatures ranging from thousands to million of degrees, plasma diagnostic is always a challenging field, which very rarely falls in the category of routine application.

Among the diagnostic system, one of the simplest and basic method to measure plasma properties is through the use of electrostatic probes, also known as Langumuir probes. Even if at first glance it could appear a simple textbook exercise, transforming this technique into a practical and reliable system for routine plasma diagnostic is far from a trivial task. The purpose of the thesis work is the design and test of two critical parts of an integrated signal conditioning and data acquisition system capable of retrieving information such as the plasma density, the ion and electron saturation current and the electron temperature from large arrays of Langmuir probes.

The thesis is divided into 6 chapters. The first introduction deals with the basic properties of plasmas, within the context of the relevance of nuclear fusion. Then follows a chapter summarizing the relevant aspects of the theory behind Langmuir probe measurements. Chapter 3 describes how the system is composed, while 4 to 5, describe the apparatus and the work done on its main analog parts, briefly summarized later on: 1) Probe's sensing stage, 2) Probe's biasing power supply. Finally, in chapter 6, conclusions are drawn based on the data and the experience collected.

Contents

Chapter 1

Introduction

Since the early studies of the nuclear fusion with the extent to enhance already existent nuclear bombs, a considerable theoretical and experimental effort has been made to develop nuclear fusion for civil purposes. Even if wind and solar energy coupled with storage can provide a substantial contribution to the total energy needs, a baseline predictable and reliable continuous clean source of energy is a fundamental requirement for the energy system. Lately, also wind and solar energy has been introduced in the market, but they're not yet valid alternatives. The road to successfully achieve nuclear fusion is paved with numerous obstacles, even though the late technological advancement has made possible great steps forwards in the understanding of the limits and conditions of such a great achievement.

1.1 Nuclear fusion

Nuclear fusion is the process that powers the core of stars preventing them from collapsing under the effect of gravity. In such process, the nuclei of light atoms fuse together to create heavier atoms, generating high amount of energy. Among all the possible combination of elements through which fusion can be achieved, the most efficient process, that has the potential to be used on Earth as source of clean energy, is the one that involves deuterium and tritium:

$$D + T = 4He(3.5MeV) + n(14.1MeV) = 17.6MeV \tag{1.1}$$

Thus, from nuclear fusion, as a waste helium and a neutron would be obtained whose overall mass is lower than the reacting particles. The mass defect, according to Einstein relation $E = mc^2$, is transformed into energy (heat) during the process, and has the potential to be exploited to generate electric energy. The choice of using deuterium and tritium is due to the simplicity through which such reaction can be achieved: this process has optimum peak temperature at around $200 \cdot 10^6$ degree, which correspond to $20keV$, being the coldest fusion reaction. Moreover, both the elements are easily available: deuterium is found in nature while tritium can be produced on site from the lithium-neutron reaction. Nevertheless, the presence of a not-charged, high-energy particle is troublesome since such particle can make conventional building materials radioactive, via a process called neutron activation [1]. Usually, the temperature is measured in eV, which can be easily converted in degree Kelvin though Boltzman constant k_B:

$$T[K] = \frac{qT[eV]}{k_B\ [J/K]} = \frac{T[eV]}{k_B[eV/K]} \tag{1.2}$$

so $1eV \simeq 11600K$. While the fusion process can be relatively easily realized in laboratory, the main problem in striving for nuclear fusion is represented by the need to have a positive energy balance of the fusion reactor, that is, to have an energy output greater than the energy required to supply the reactor and all its auxiliary systems. The parameters used to estimate this energy balance can be found through the Lawson criterion [2].

1.1.1 Lawson criterion & triple product

Lawson criterion is a figure of merit that, originally, gave a minimum required value for the product of plasma (or electron) density n_e and energy confinement time τ_E that leads to a net energy output. Later, more thorough analysis suggested that a better criterion requires the inclusion of the temperature T_e, obtaining a condition on the triple product:

$$n_e \tau_E T_e \tag{1.3}$$

which also has a minimum required value. Lawson criterion eventually may refer to this value in some literature. Even though reaching a fusion-wise satisfying value for each parameter of the product had been achieved more than 40 years ago, the challenge still lies in reaching such values all together. The central idea of the concept was examining the energy fusion balance of a nuclear fusion reactor. The concept is explained in the formula:

$$\begin{cases} P_{net} = \eta(P_{fusion} - P_{rad-loss} - P_{cond-loss}) \\ P_{fusion} = n_D \cdot n_T \cdot \sigma(T) \cdot E_{ch} \end{cases} \tag{1.4}$$

in which n_D and n_T are densities of deuterium and tritium, $\sigma(T)$, also called cross section, is the probability of a fusion event and E_{ch} is energy released in each fusion event. The estimation results showed the minimum temperature to be $T_{min} = 30 \cdot 10^6\ K = 2.6keV$. When the production rate is higher than the loss rate, then P_{net} will be positive. In this case, if enough power is channeled into the fuel, then the system will become self-sustaining and is said to be ignited.

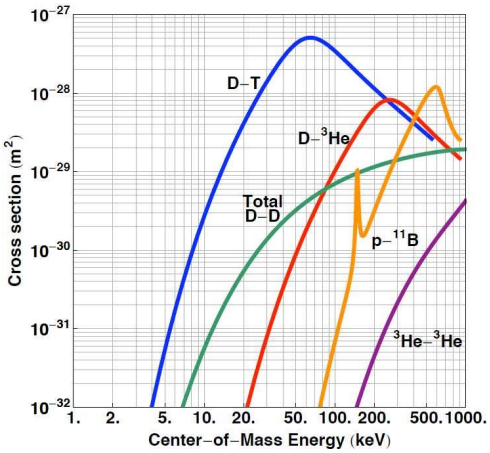

Figure 1.1: Cross section of a nuclear reaction for various kind of fusion.

Earlier in the paragraph was introduced the energy confinement time τ_E. Such value measures the rate at which the system loses energy. It is defined as the energy content per unit volume divided by the rate of energy loss per unit volume:

$$\tau_E = \frac{W}{P_{loss}} \tag{1.5}$$

Now, by doing some math, which explanation is beyond the purpose of this chapter, the Lawson criterion can be estimated as:

$$\begin{cases} W = 3n_e T_e \\ f = \frac{1}{4} n_e^2 \langle \sigma(T_e) v \rangle \rightarrow n_e \tau_E \geq L(T_e) = \dfrac{12 T_e}{E_{ch} \langle \sigma(T_e) v \rangle} \\ f E_{ch} \geq P_{loss} \end{cases} \tag{1.6}$$

in which f denotes the volume rate, i.e., the number of reactions per volume per time and fE_{ch} is the volume rate of heating by fusion. By locating the minimum of the Lawson function, which occurs at $T = 25keV$, the lower limit for the Lawson criterion is found at $n_e\tau_E \geq 1.5 \cdot 10^{20}$ $[s/m^3]$ (see Figure 1.2a). An important consideration has to be done, however, to justify the results obtained. It is assumed that all the species in the plasma have the same temperature, that there are no impurities and no helium ash and that deuterium and tritium are present in a 50-50 mixture.

There are many possible configuration in which nuclear fusion can be achieved, one of them being the *tokamak* configuration (and the most interesting for this case, since it is used in ITER). A review of the main configuration will be given in a following paragraph, bur for now it is beyond the purpose of this discussion. A more interesting figure of merit when dealing with the *tokamak* configuration is the triple product, as define at the beginning of the section. By extending Lawson criterion, one can find:

$$n_e T_e \tau_E \geq \frac{12 T_e^2}{E_{ch}\langle\sigma(T_e)v\rangle} \tag{1.7}$$

form which, assuming the same line of thought of the previous derivation, the lower bound is found at the minimum of the function and is given by $n_e T_e \tau_E \geq 3 \cdot 10^{21} keVs/m^3$, found at a minimum temperature of $T = 14keV$ (see Figure 1.2b). In the case of the *tokamak*, it is

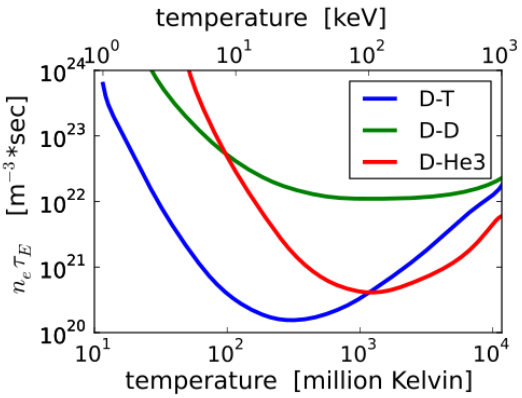

(a) The Lawson criterion, or minimum value of (electron density * energy confinement time) required for self-heating, for three fusion reactions. For DT, $n_e\tau_E$ minimizes near the temperature 25 keV (300 million kelvins) (By Dstrozzi - Own work, CC BY-SA 3.0, https://commons.wikimedia.org/w/index.php?curid=12380921).

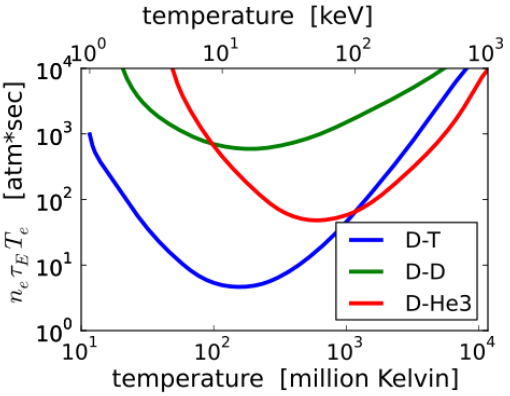

(b) The fusion triple product condition for three fusion reactions (By Dstrozzi - This W3C-unspecified plot was created with Matplotlib., CC BY-SA 3.0, https://commons.wikimedia.org/w/index.php?curid=12153588).

Figure 1.2: Lawson criterion and triple product plots for various reactions.

empirically found that the energy confinement time τ_E is proportional to $n_e^{1/3}/P^{2/3}$, where P is the heating power. In a plasma near the optimum temperature, P is proportional to $(n_e T_e)^2$. Therefore, it follows:

$$\begin{aligned} n_e T_e \tau_E &\propto n_e T_e \frac{n_e^{1/3}}{P^{2/3}} \\ &\propto n_e T_e \frac{n_e^{1/3}}{(n_e^2 T_e^2)^{2/3}} \\ &\propto T^{-1/3} \end{aligned} \tag{1.8}$$

highlighting that the triple product is weakly dependent on the temperature, making it an adequate measure of the efficiency of the confinement scheme. It can be safely said that Lawson criterion and the triple product constitute a necessary condition in order to achieve and perform nuclear fusion with a positive net power output. However, reaching those condition is anything but trivial and lot of effort and time are placed into further developing the knowledge relative to the technology needed [2].

1.1.2 Fusion confinement methods

In the previous discussion, one of the key elements that jump right into the eyes are the high temperature at which the plasma needs to burn in order to sustain nuclear fusion. Being important temperatures, it is quite straightforward to understand that plasma cannot be in contact with any solid material and it has to be created in a vacuum chamber, being its density equivalent to a very rarefied gas (between 10^{-6} and 10^{-5} times the air density). Moreover, a very high base vacuum (10^{-4} Pa or less) is necessary to maintain a very low level of impurities. Even if the latter aspect is easily achievable, maintaining the separation between the chamber walls and plasma is still troublesome. High temperatures usually imply high pressures and the plasma tends to expand rapidly. Fortunately, the temperature gradient is such that a chamber of few meters can be adopted, of course the size is a function of the sought temperature and of the external forces applied to contrast the plasma expansion. The set of external forces used to counterbalance the plasma pressure is exerted by the employed confinement method. There are three main confinement principles, being known as gravitational confinement, magnetic confinement and inertial confinement.

Gravitational confinement

One of the forces capable of allowing for long enough confinement time is the gravitational force. Nonetheless, to have sufficient force there is also the need of a great mass. The amount of mass needed is something found only in stars and the least massive star capable of sustaining fusion are red dwarfs.

Magnetic confinement

The plasma is constituted by ions, that are charged particles. Lorentz's law implies that a charged particle within a strong magnetic filed is bound to the magnetic field lines. In a straight and uniform filed, charged particles follow a helical path around a magnetic line. In particular, the motion can be seen as the composition of two trajectories: the first one spinning around the line with a radius $r_L = v_\perp/\omega_c$ and the second one being a linear motion with velocity $v_\parallel$ along the filed line.

In early configurations, a first approach was to create a magnetic bottle, with the intent to block the drifting particles within the plasma core and therefore to increment the energy confinement time. However, such configuration was later abandoned: particles with small perpendicular velocities were not deflected by the magnetic mirrors, resulting in a depletion of the population of the latter. The direct consequence is that the velocity distribution is not maxwellian anymore leading to plasma instabilities and loss of hotter particles, thus cooling the plasma.

A solution to take care of the depletion problem is to wind up the cylinder in a toroidal configuration. In this way the parallel losses at the two ends of the magnetic path are eliminated. The magnetic field can be simply generated by wrapping coils around the toroidal vacuum chamber. However, in such a way, the magnetic field is stronger in the inner side, creating thus a magnetic field gradient. This leads to particle drift and plasma losses. To avoid that, a poloidal magnetic field is induced so as to produce a field with the structure of a helix shape (similar to the DNA shape). This practice is known in literature as rotational transform. However, if

not suitably designed, this methods can again lead to instabilities and loss of confinement. The safety factor q is a measure of the twisting factor of the magnetic filed used:

$$q = \frac{\text{number of toroidal turns}}{\text{number of poloidal turns}} \tag{1.9}$$

and it is found to be more important in the *tokamak* configuration. More specifically, if $q \leq \frac{1}{2}$, then the plasma is unstable. Historically speaking, two configurations have paved their way to nowadays: the *tokamak* (Figure 1.3a) and the stellarator (Figure 1.3b). Even though they are two valid alternatives from a theoretically point of view, mechanical and technological difficulties to implement the stellarator made him fall second compared to the *tokamak* configuration. It has to be pointed out that whereas the *tokamak* has undergone a selection process throughout the years, culminating in the ITER device ad future demonstration, such convergence has not yet happened for the stellarator configuration. For this reason, a comparison between the two leading to meaningful results is yet to be done and it is waiting for the stellarator to be further developed [3].

Another confinement method worth mentioning is the Reversed Field Pinch (RFP) configuration. It is a configuration that uses a unique magnetic field to contain quasi-thermonuclear plasma and is used to principally study magnetic confinement fusion. The characteristic that distinguishes this configuration from that of the *tokamak* or the stellarator is that, moving out radially from the inner radius of the toroid, the magnetic field changes its direction (from here "reverse field"). Figure 1.4 shown how the magnetic field behave in a RFP configuration [4].

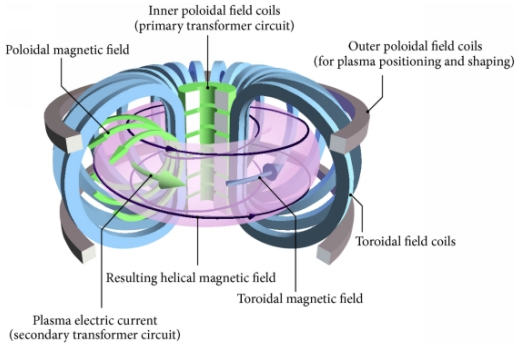

(a) TOKAMAK confinement method (S. Li, H. Jiang, Z. Ren, C. Xu - S. Li et. al. "Optimal Tracking for a Divergent-Type Parabolic PDE System in Current Profile Control" , Abstract and Applied Analysis doi:10.1155/2014/940965, CC BY 4.0, https://commons.wikimedia.org/w/index.php?curid=74679708).

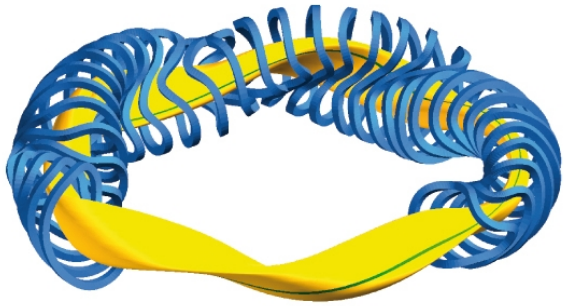

(b) Stellarator configuration (By Max-Planck Institut für Plasmaphysik - Max-Planck Institut für Plasmaphysik, CC BY 3.0, https://commons.wikimedia.org/w/index.php?curid=24388371).

Figure 1.3: Magnetic confinement methods used for fusion-wise nuclear plasma.

Inertial confinement

Inertial confinement is an alternative way to achieve nuclear fusion in which external magnetic fields are not used. Also known as ICF (Inertial Confinement Fusion), it was born within nuclear weapon research and significant part of the researches are classified. The idea is to ignite a small capsule of D-T fuel via high energy lasers or ion beam pulses. The bespoke capsules are heated to a temperature of $10^8 K$ so as to ablate a first layer which then causes the capsule to implode. The high temperature in conjunction with the high pressure resulting from the

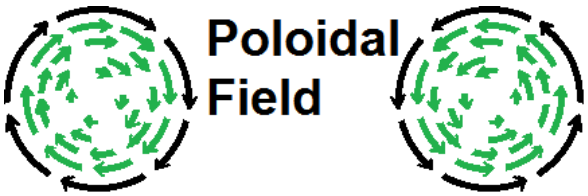

(a) RFP poloidal filed (By WikiHelper2134 at en.wikipedia, CC BY-SA 3.0, https://commons.wikimedia.org/w/index.php?curid=47214119).

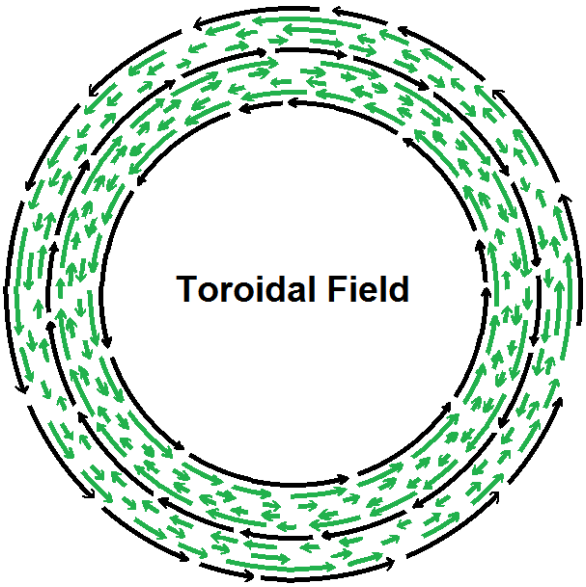

(b) RFP toroidal filed (By WikiHelper2134 - I created this image, CC BY-SA 4.0, https://en.wikipedia.org/w/index.php?curid=59524956).

Figure 1.4: Magnetic confinement methods used for fusion-wise nuclear plasma.

implosion thus creates the basis for fusion to occur. The procedure relies on the fuel mass inertia as a confinement method. There are two different way to heat up the fuel capsule, being namely direct drive and indirect drive approach. The former involves overlapping beams to directly heat the capsule while the latter, by means of an apposite vessel (hohlraum, scientifically speaking), the beams are converted into X-rays and the capsule is isotropically heated. The main obstacle to achieve fusion through ICF is the Rayleigh–Taylor instability: if the fusion fuel isn't heated isotropically in all its surface, high and low pressures spot are created which then eventually lead the capsule to "escape". Such problem is overcome (at least in part) by implementing laser smoothing techniques or by indirect drive approach [5].

1.1.3 Research facilities

Since the first controlled thermonuclear fusion reaction in 1958, numerous research facilities have been built with the aim to study all the various aspect that characterize the a nuclear fusion process. However, even though great results and progress have been made, the idea of having a self-sustaining thermonuclear fusion reactor is yet to become reality. There are few experiments, however, worthy of being mentioned, since they achieved excellent results.

Tore supra, which is a magnetic confinement machine operating with a tokamak configuration, detains the record for the longest plasma duration, 6 minutes 30 seconds, and over $1000MJ$ of energy injected and extracted, allowing researchers to test critical part of equipment and superconducting magnets.

Joint European Torus (JET) was (it has been closed in 2023) a magnetic confinement machine, which primary goal was to obtain an energy gain factor Q close to 1. Over the years it was used to perform various experiments, achieving important results, such as a energy gain factor $Q = 0.67$, which was a record until 2021. It also detains the record for the highest energy impulse: $5s$ during which $69MJ$ were released.

JT-60SA is the largest working *tokamak* with superconductive magnets. Throughout the years it underwent major modifications, which allowed it to achieve an equivalent energy gain factor $Q_{DT}^{eq} = 1.05$. In other words, if the fusion fuel was replaced with a 1:1 DT fuel, the reactor

would have produced an energy output 1.05 greater then the energy used to start the reaction. This record was later shattered, achieving an astonishing $Q_{DT}^{eq} = 1.25$. Moreover it holds the record for both the highest fusion triple product achieved, $n_e T_e \tau_E = 1.53 \cdot 10^{21} keVs/m^3$, and for the highest ion temperature reached, $45keV$, more than 500 million degree. (even though T_e and T_i refer to different temperatures, in this paper they are assumed to be equal $T_e = T_i = T$).

1.2 ITER project

The contribution of the experiments in plasma physics are not indifferent and, through the achieved successes, they also paved the road that leads to the construction of ITER. Despite being still in construction and despite all the setbacks, it is thought that ITER, which stands for International Thermonuclear European Reactor, will be the greatest fusion research facility with the aim not only of achieving fusion but of demonstrating that it is possible to achieve a gain in plasma energy for thousands of seconds, a condition for the plasma and the plant which is practically equivalent to a continuous steady state. Talking about a fusion reactor, the temperature reached to sustain a fusion reaction is set to be $1.5 \cdot 10^8 K$. To achieve such a high temperature, the plasma needs to be heated up: this procedure will be carried out by two different methods, one being via neutral ion beams and the other being a radiofrequency system. The neutral ion beam injector (MITICA experiment) is in construction at the NBTF facility in Padua, at Consorzio RFX. Even if the machine is designed to produce a beam with an energy of $1MeV$, the plasma produced in the source and that of the beam, falls in the category fo the so called cold plasma, in which the temperature is around $1eV$ to $10eV$, nowhere close to the keV range of the fusion plasma core.

1.2.1 Neutral Beam Test Facility - NBTF

The Neutral Beam Test Facility (NBTF) is the laboratory in which is currently under development the 1:1 scale prototype of the negative beam injector of the ITER reactor. The experiment is named MITICA. Moreover, it is home also of the world most powerful negative ion source, SPIDER, that is a component of MITICA. SPIDER is in operation since 2018. MITICA is a machine that should reach standards never reached before, as a continuous beam supply of $1MeV$ for $3600s$, at a delivered power of $16.5MW$. As can be easily deduced, MITICA is a complex experimental system that requires as much as meaningful data as possible to operate properly and verify what is going on inside the system (this statement is valid for all the experiments mentioned so far, including ITER). Data are retrieved by a great variety of measurements. The set of these and their related methods for the measurement of the plasma properties is called plasma diagnostics. Objective of this thesis work is to help developing the electrostatic probe management of MITICA (EPICA) by analyzing the system and find out possible criticalities of the future implementation. Moreover, the system is designed to natively comply with ITER standards regarding data acquisition (DAQ) protocols, implementing the analog/digital interfaces needed to convert the physical measurements in numerical data. The choice to develop a custom system versus using commercial, of-the-shelf components (COTS) is dictated by a number of constraints and consideration discussed later.

Chapter 2

Plasma diagnostic

Controlled thermonuclear fusion is no small achievement. It requires a huge amount of dedication and time, not mentioning the thorough knowledge and understanding of one of its principle participants: fusion plasma. This latter has its own imperatives of temperature, density, confinement and so on, which create a stimulating environment in which plasma research is conducted. A great part of plasma research is devoted in finding new methods to retrieve data from the plasma itself and, not being exactly a textbook exercise, this part of plasma physics faces an high amount of challenges. Furthermore, usually the measurements that are carried out must comply with standards regarding accuracy, sensitivity and robustness of the measurement system which are very often threatened by the environment in which they are carried out and by the measurement system itself: electromagnetic pulses, radio frequency interferences, the length of the transmission lines, etc... are all key factors in the design and construction of the diagnostic apparatus. This part of plasma physics takes the name of plasma diagnostic.

There is a pool of different methods that allows for gaining plasma information. Some of them are standard diagnostic techniques and other are techniques taylored for the specific task they have to carry out. A complete description of those methods goes far beyond the purposes of this work, but an idea of the possible implementations is given in Table 2.1. f_x is the particle

Measurement Type	Parameters
Magnetic	T_e, E, B
Particle flux	f_e, f_i, T_e, T_i, n_e, n_i, E, v_i
Refractive index	n_e, T_e, T_i
Scattering	f_e, n_e, n_i, B
Optical emission	T_e, n_e, n_i
Line Radiation	n_e, n_i, n_0, B, T_e, T_i, v_i

Table 2.1: Plasma diagnostic techniques.

distribution function, T_x is the x-temperature, n_x is the x-density, v_x si the particle velocity, E the electric field and B the magnetic field. Subscript x stands for ions (i), electrons (e) or neutrals (0). It has to be reminded, however, that the particular technique or the combination of multiple techniques chosen for a particular application are a tradeoff among technical requirements such as precision, spatial and temporal resolution to perform the measurement and available resources [6].

The main effort of this thesis work was focused in the analysis and characterization of a diagnostic system that falls in the particle flux measurement type. The main component of this kind of measure is the electrostatic probes, also known as Langmuir probe (in the following discussions both terms will be used). The basic principle through which plasma can be measured via electrostatic probes is a simple IV reading, giving thus to this kind of measurement the possibility to be developed and taylored to specific cases.

2.1 Plasma

In early school it is taught that matter can only assume three states, being solid, liquid and gas. However, this information is incomplete, since there is at least one more state worth mentioning: the plasma state. It consist of ionized gas, characterized by the presence of charged particles, being ions and electrons, that gives it conductive properties. Characteristic of plasma are the high temperatures which can span several order of magnitude. Temperature can range from those of cold plasma, around $(2 \div 10)\ eV$ to those of fusion plasma, being in the order of tens of keV. Also the density can change quite a bit, depending which plasma is considered and what is its purpose. Typical density range in laboratory plasma can be estimated between $10^{13} m^{-3}$ and $10^{20} m^{-3}$, even though there are plasma with density that exceed these values. Based on temperature and density, plasma can be divided into two categories. Cold plasma, characterized by low temperatures ($(1.5 \div 10)\ eV$) and low densities ($(10^{13} \div 10^{17})\ m^{-3}$), are used in a vast variety of industrial process. Fusion plasmas, characterized by high temperatures (several keV) and high densities (up to $10^{20}\ m^{-3}$), are found in nuclear fusion experiments. The plasma to be measured in MITICA, at the beam source, at the neutralizer and at the residual ion dump falls in the category of cold plasmas.

2.2 Particle flux - Langmuir probes

Among all possible ways to measure a plasma, the use of Langmuir probes is certainly the simplest, consisting in just sticking a (suitably sized) wire in it and measuring the current flowing through the wire itself at various applied voltages. However, the drawback for being a relatively simple approach lies in two main issues: 1) the probe can be a perturbative diagnostic since usually it is much larger than the electrostatic shielding distance (Debye length) and 2) the interpretation of the resulting curve is of relative difficulty and requires many steps. The former issue addresses the need for the wire to be quite robust, due to the harsh environment within which is inserted, and designed so as to not interfere with the plasma. The last one is related to the measurement itself and can be far from trivial. Nevertheless, such inconveniences can be overcome with some due effort.

There exist different shapes of probes, spanning from spherical to flat-tip ones. However, for the extent of this work, only the cylindrical shaped are considered. In Figure 2.1 is shown a possible implementation of a cylindrical Langmuir probe. Despite being the probe a rather simple

Figure 2.1: Cylindrical Langmuir probe.

piece of equipment, the physics laws governing its behavior are quite complex. Nonetheless, a good understanding of these laws is required in order to create a model of the probe. An overall basic view is hence offered in the following paragraphs.

2.2.1 General theory

As a first approach, consider the I-V relationship of the probe, curve that is reported in Figure 2.2. From the plot there are two principal information that can be derived: the first is that the total current generated by the probe is given by the contribution of both ions and electrons. The

second details that jump in the eyes is that the plot can be divided into three sections. From Figure 2.2 there are some useful parameters, such as the plasma potential, or space potential, V_s (in Figure 2.2 it is defined as the voltage at which there is the electron saturation knee) and the floating potential V_f, that is the voltage at which the probe current is zero. Usually $V_s \simeq 5T_e/q$, in which T_e is the electron temperature expressed in eV. There is a third potential that has to be taken into account: the biasing voltage V_{bias}. This latter is the voltage at which the probe is polarized. Once these three voltages are defined, an analysis of the plot of Figure 2.2 can be carried out. The adopted convention is to consider negative the ion current and positive the

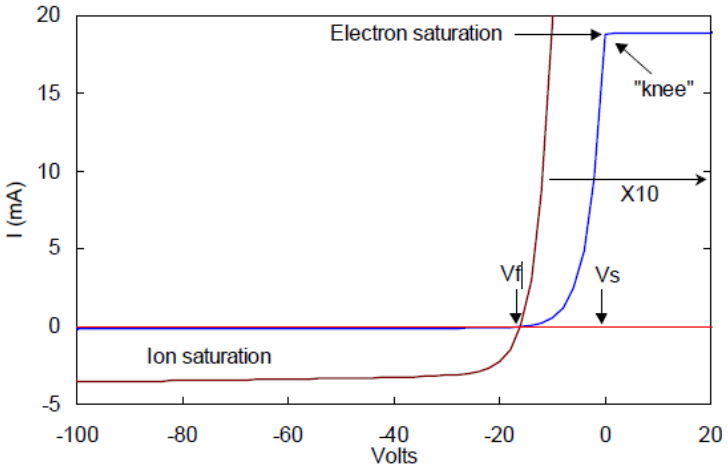

Figure 2.2: Ideal IV-curve of a Langmuir probe [7].

electron current. Taking as a reference the space potential V_s, at $V_{bias} >> V_s$, all the ions are repelled and an electron saturation current is encountered while at $V_{bias} << V_f$ the ion saturation current prevails on the electron current, the latter can be neglected. The characteristic is now thus divided into three region: the ion saturation region (ISR) at $V_{bias} < V_f$, the transition region (TR) at $V_f < V_{bias} < V_s$ and the electron saturation region (ESR) at $V_{bias} > V_s$.

Sheath

Usually the plasma is generated inside a vacuum chamber with finite size, that is, the plasma is confined. The walls of the chamber within which such plasma is contained behave like a charged surface and therefore interact with the plasma itself. The quantity that will be affected the most is the plasma potential, in this section called Φ. As a reference for the following discussion, the Figure 2.3 can be taken into account, in which the bespoke consideration is restricted to a one dimensional model with no magnetic field [8] [9]. To understand why Φ has a non-linear distribution and is not constant within the section of the chamber, a good start is to look at the ions and electrons velocities:

$$\begin{cases} v_i = \sqrt{\frac{2E_i}{m_i}} \\ v_e = \sqrt{\frac{kT_e}{2\pi m_e}} \end{cases} \tag{2.1}$$

where the subscript "i" and "e" stand respectively for ions and electrons. The ion velocity v_i is treated as a monochromatic particle beam, while the electron velocity v_e comes from a normalized thermal distribution. From the equation above, taking the ration between v_i and v_e one obtains $v_i \propto v_e\sqrt{m_e/m_i}$, leading to the conclusion that the ion velocity is much smaller that the electron velocity, since the $m_i >> m_e$. Even though it seems that this results has no practical meaning, the higher electron speed allows them to reach the external walls faster than the ions and therefore charging negatively the surface against which they collide, with respect to the bulk plasma. Thus, the wall potential Φ_W will be negative, attracting ions to the sheath

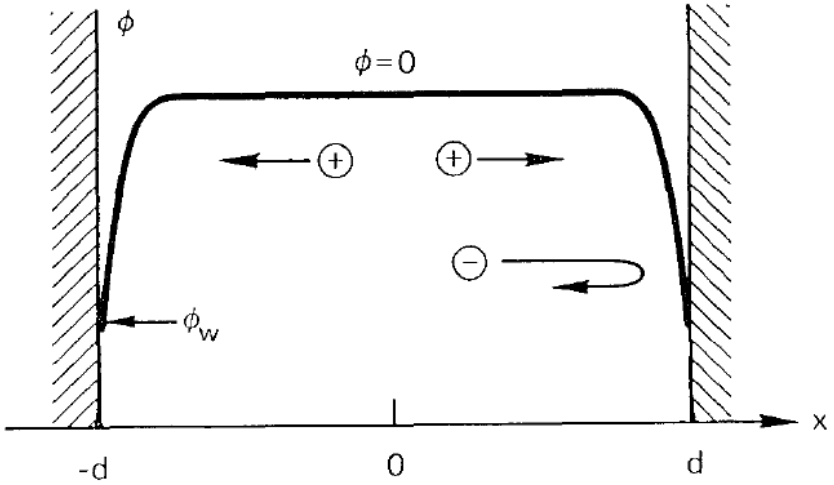

Figure 2.3: Plasma potential variation inside the vacuum chamber.

region, with the extent to balance the presence of the electrons. However, this mechanism is usually limited several Debye lengths. Outside the sheath, Φ is constant, therefore taking the form depicted to Figure 2.3.

Electrostatic probes suffer the same effect, since it's verified whenever a surface is placed in contact with the plasma. The given description of the phenomena is an overview and thus no analytical approach has been used. In a nutshell, the sheath region defines a transition from the plasma core to a solid surface. It's a region of the plasma in which is present a greater density of ions to balance the electron density at the surface of the object with which is in contact. It is important to keep in mind the result discussed are made by implicitly assuming the following conditions:

- The plasma is considered collisionless.
- Electron temperature is considered to be equal to the ion temperature, that is, $T_e = T_i$.
- The plasma has no magnetic field in it.
- The insertion of the probe do not cause disturbances, or, in any case, the disturbances caused can be neglected.
- The electron distribution is Maxwellian.

Ion Saturation Region (ISR)

Whenever the probe is negatively biased, depending on the bias magnitude, a certain amount of ions is attracted towards the surface of the probe. In this situation all the electrons are repelled by the negative bias, hence the electron current can be neglected. Satisfying the Bohm criterion, such current can be estimated as:

$$J_i^{sat} = \alpha q n_i c_s = \alpha q n_i \sqrt{\frac{k_B T_i}{m_i}} \tag{2.2}$$

in which c_s is the sound speed (Bohm criterion says the ion velocity at the sheath edge is simply the sound velocity), $\alpha \simeq 0.5$, q is the elementary charge, n_i is the ion density at the sheath edge. However, such equation defines a constant saturation current, which is true only for flat probes. Usually, cylindrical probes features a slope in it depending on the sheath ratio $\xi = R_P/\lambda_D$.

Transition Region (TR) and Electron Saturation Region (ESR)

The behavior of the current in this region is defined by an exponential law, that comes from the solution of electrostatic Poisson's equation [7], that is, if plotted in a semi-logarithmic scale against the probe voltage V_S should give a straight line. The current follows the equation:

$$J_e = J_e^{sat} e^{\frac{V_{bias}-V_s}{K_B T_e}} \tag{2.3}$$

in which the electron saturation current is give by:

$$J_e^{sat} = q n_e \sqrt{\frac{K_B T_e}{2\pi m_e}} \tag{2.4}$$

The plot in semi-logarithmic scale should have a slope equal to $\frac{1}{T_e}$, giving thus a good measure of the electron temperature T_e. By increasing the voltage up to V_s, the probe should be biased enough to be able to attract all the electrons, thus saturating the electron current. One would expect that such current should be very much greater than the ion saturation current (indeed it is verified in plasma in which the condition above are true), but normally, those approximation are not always true and the curve will change accordingly. Instead of having a sharp knee (see Figure 2.2), there will be a (great) round-off and the supposed constant saturation current will increase. In Figure 2.4 is shown how the probe is expected to behave when brought to its limit. In Figure 2.5 are exposed some I-V characteristic that are quite close to the real behavior of the probe. As it can be seen it is quite difficult to point out the knee of the curve. Minimum

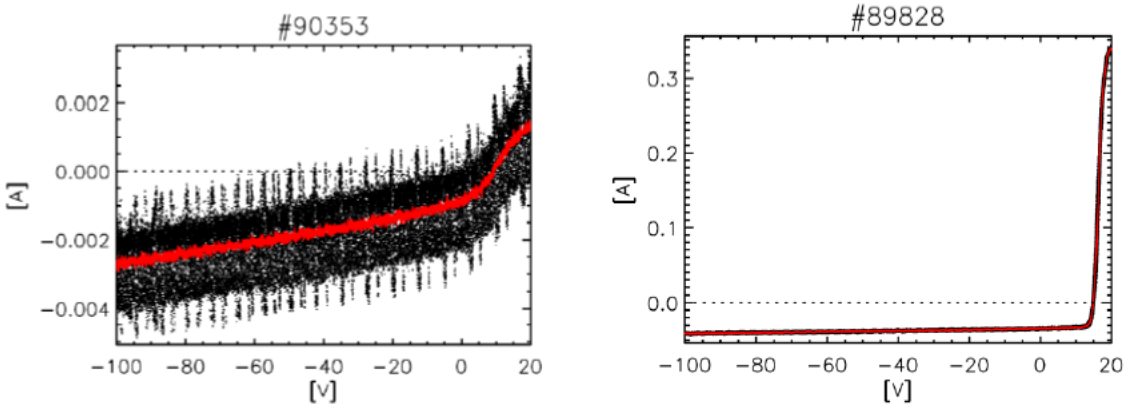

Figure 2.4: Reference Langmuir probe characteristics expected on extreme cases, in the left-image with minimum current range while in the right-image with maximum current range.

and maximum current range can be easily understood by looking at the factor that characterize ion and electron saturation currents. The stronger dependence is given by the density n_x, while smaller dependence are given by the temperature T_x and the ion mass m_i. Thus, the minimum current range is found with n_x^{min}, T_x^{min} and m_i^{max}, while the maximum is found with n_x^{max}, T_x^{max} and m_i^{min}.

Total current

As said at the beginning of the section when explaining the I-V curve relationship, the total current of the probe is defined as the algebraic sum of all the currents within, accordingly to the

adopted convention. Thus, the total current can be written as:

$$\begin{aligned} I_p &= A_p(J_e - J_i^{sat}) \\ &= A_p\left(J_e^{sat} e^{\frac{V_{bias}-V_s}{k_B T_e}} - \alpha n_i q c_s\right) \\ &= A_p\left(q n_e \sqrt{\frac{k_B T_e}{2\pi m_e}} e^{\frac{V_{bias}-V_s}{K_B T_e}} - \alpha q n_i \sqrt{\frac{k_B T_i}{m_i}}\right) \\ &= \alpha A_p q n \sqrt{\frac{k_B T_i}{m_i}}\left(\frac{1}{\alpha}\sqrt{\frac{m_i}{2\pi m_e}} e^{\frac{V_{bias}-V_s}{k_B T_e}} - 1\right) \\ &= A_p J_i^{sat}\left(\frac{1}{\alpha}\sqrt{\frac{m_i}{2\pi m_e}} e^{\frac{V_{bias}-V_s}{k_B T_e}} - 1\right) \end{aligned} \tag{2.5}$$

in which A_p is the area of the probe. In the derivation above the same approximations discussed in the sheath paragraph where made, and thus they have validity only in those conditions. However, when creating the probe model, such constraints will be relaxed a bit, allowing for different temperatures, densities and species in the same plasma.

2.3 Probe modeling

The basic model presented so far, while is good for understanding the basic features of the Langmuir probe measurement is too crude for being used in the satisfactory analysis of the measurement circuit discussed in this thesis. We will use a more adequate model found in literature, which takes into account more physics and has been explicitly developed for circuit simulation [10]. Such a model takes also into account the sheath ratio $\xi = R_P/\lambda_D$, allowing for a better resemblance with the real behavior of the probe. The model is defined as in the following:

$$I_P = \sum I_{sat_j} F(\Phi_{s_j}) \tag{2.6}$$

and as it can be easily understood, the total current generated by the probe is the sum of all the species' currents multiplied by a collection factor $F(\cdot)$, which is a function of the biasing voltage. The latter function can be written as:

$$F(\Phi_{S_j}) = \begin{cases} e^{\Phi_{s_j}} & for \quad \Phi_{s_j} \leq 0 \\ \xi_P erf(\tilde{\Phi}_{s_j}) + e^{\Phi_{s_j}} erfc(\xi_P \tilde{\Phi}_{s_j}) & for \quad \Phi_{s_j} > 0 \end{cases} \tag{2.7}$$

in which:

$$I_{sat_j} = q A_P n_j \sqrt{\frac{k_B T_j}{2\pi m_j}}; \quad \Phi_{s_j} = \frac{-(V_{bias} - V_s)}{k_B T_j}; \quad \tilde{\Phi}_{s_j} = \sqrt{\frac{\Phi_{s_j}}{\xi_P^2 - 1}}; \quad \xi_P = \frac{1}{\xi} \tag{2.8}$$

Having all the formulae needed, it is possible to implement such model with an algorithm. Different iteration have been performed, in order to have an idea of how the probe behave with different kind of plasma characteristics. The model equations had been implemented in python and some results of interest obtained are shown in Figure 2.5. The plot in Figure 2.5a shows that the bigger impact on the current is given by the contribution of plasma density, conclusion which is quite easy to attain also by looking at the formulae in (2.8). Comparing this latter plot with that in Figure 2.5c, it can be seen that little change is introduced by changing the plasma ion species. The only appreciable change is in the ion saturation current, as shown in Figure 2.5d. Finally, the change in the electron temperature just has a medium impact on the behavior, changing only the space potential.

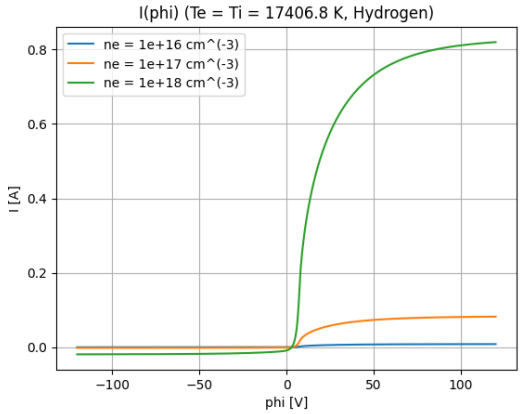

(a) Current generated with different densities.

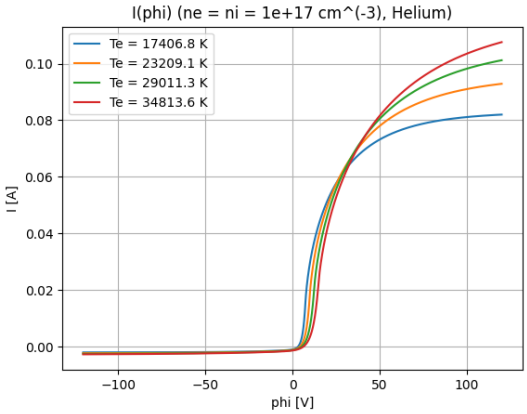

(b) Current generated with different temperatures.

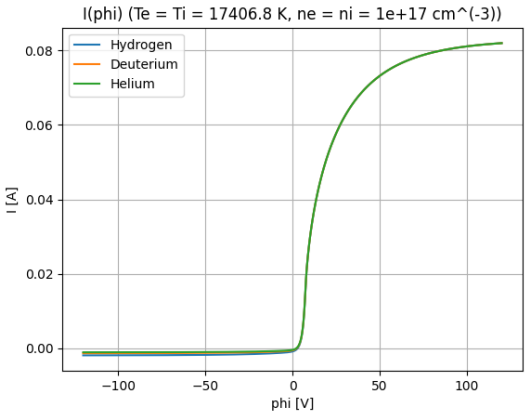

(c) Current generated with different species.

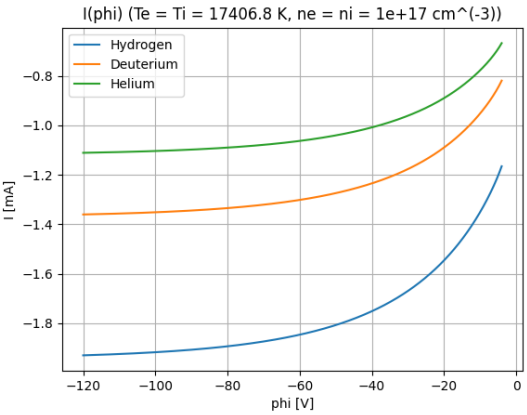

(d) Current generated with different species.

Figure 2.5: Plots of the probe current according to the model defined above. The probe area $A_p = 5 \cdot 10^{-6} m^2$

Chapter 3

Electrostatic Probe Integrated Conditioning and data Acquisition module - EPICA

As mentioned in Chapter 1 and Chapter 2, the need of a reliable diagnostic system is of paramount importance. The development of such a system can be challenging, since the environment in which it has to operate is hostile, specially from the ElectroMagnetic Interference (EMI) point of view. However, the experience gained previously in SPIDER, combined with the technological development of recent years have made it possible to improve many drawbacks and to better manage production costs and timing.

3.1 MITICA

MITICA, which is the acronym for Megavolt ITER Injector and Concept Advancement, is, as previously described, the 1:1 scale prototype of the Neutral Beam Injector (NBI) for ITER currently in an advancement state of construction at the NBTF facility in the premises of the Consorzion RFX in Padua. The focus of this section is not so much to give a description of its characteristics but to provide a description of its anatomy, which is much more useful for understanding how the diagnostic system will be implemented and the reason behind certain design decisions. Figure 3.1 shows the components of MITICA.

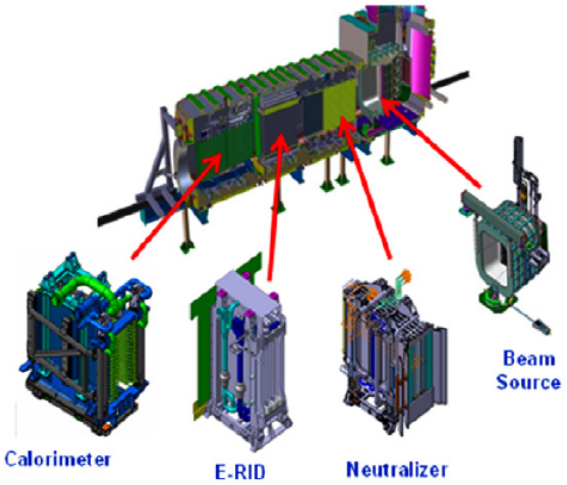

Figure 3.1: MITICA composition.

Ion source The first component is the beam source. This source is a replica of the prototype previously tested in the same facility and known as SPIDER. It is responsible for creating the negative ion beam and operates at 1MV. The ions are accelerated through five 200kV acceleration phases. The source is designed to produce a 46A Hydrogen ion beam or a 40A Deuterium ion beam.

Neutralizer The neutralizer is the component assigned to make the negative particle beam neutral, using a neutral gas of the same type. It is able to absorb a total of 5MW of power. However, since the efficiency of the high energy negative beam neutralization is 50%, there is the need to filter out a significant amount of positive and negative ions.

Residual Ion Dump (RID) Right after the neutralizer, there is the Residual Ion Dump (RID), which is able to remove positive and negative charged particles by applying a transverse electric field. This field is able to collect the charged particles, but has no effect on the neutral ones, thus leaving them untouched. It is designed to absorb a total power of 19MW and to withstand power densities up to $8MW/m^2$.

Calorimeter The last component serves as a "gate". It consists of two walls of water-cooled pipes. When the walls are closed, they assume a "V-shape" configuration and they serves as the beam target, allowing for power measurement. When the walls are open, they let the beam to exit undisturbed from the injector. It is designed to absorb and withstand a power of up to 18MW.

3.2 Measurements types and configuration

The relevant plasma parameters can be indirectly measured by analyzing the probe characteristic. The classical method consist in sweeping the biasing voltage within a defined range, as an example the one defined in Chapter 2, and plotting the corresponding current in a I-V plane. To accomplish this task, different measurement configuration are being implemented, thanks to a switch module, which allows the system to change between the configurations listed below.

3.2.1 Single probe characteristic

The probe characteristic is of paramount importance to this kind of diagnostic, and having a simple, yet effective way through which it be retrieved is as important. The circuital configu-

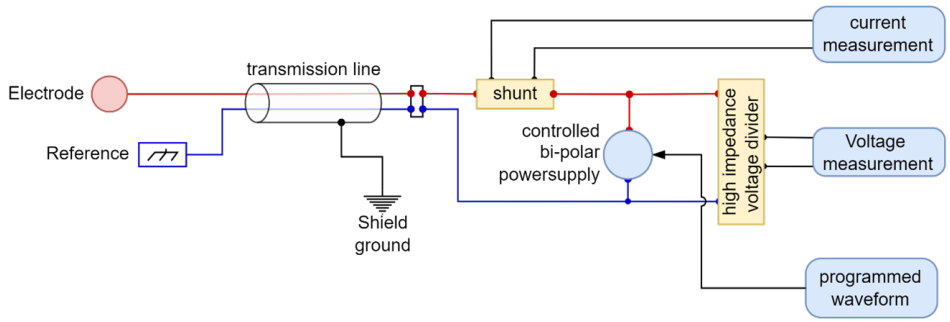

Figure 3.2: Single probe characteristic measurement set up.

ration used is that of Figure 3.2, while the characteristic to be plotted is shown in Figure 3.3. From this kind of measurement, the relevant parameter that can be extrapolated directly from the plot are the ion saturation current I_i^{sat}, the floating potential V_f and the electron saturation

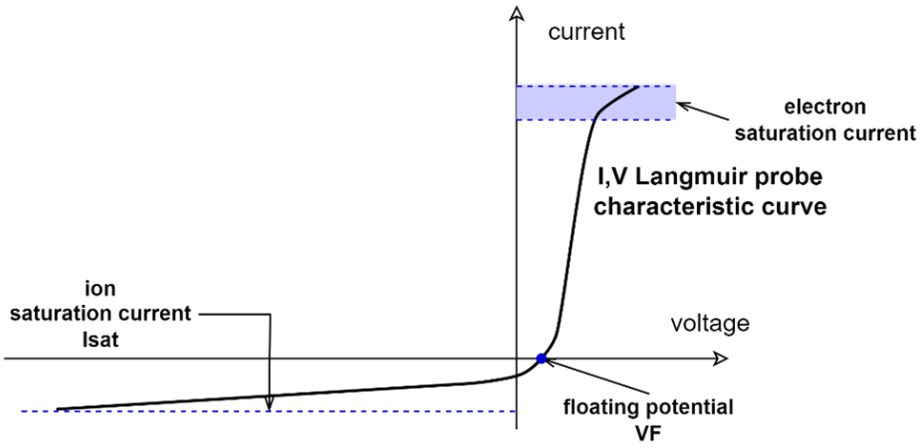

Figure 3.3: Example of an ideal single probe characteristic.

current I_e^{sat}. The latter, however, can be troublesome to measure and dangerous to manage due to sheath effect that can increase the current to values not accounted for. For the present purpose the current at the maximum meaningful voltage applied to the electrode is considered.

3.2.2 Single probe floating potential

The typical set up of a floating potential measurement is shown in Figure 3.4. It is of ease implementation and reliable and for this reasons it is widely used, even though the measurement itself is not precise. Due to the high electron saturation current that can damage the probe

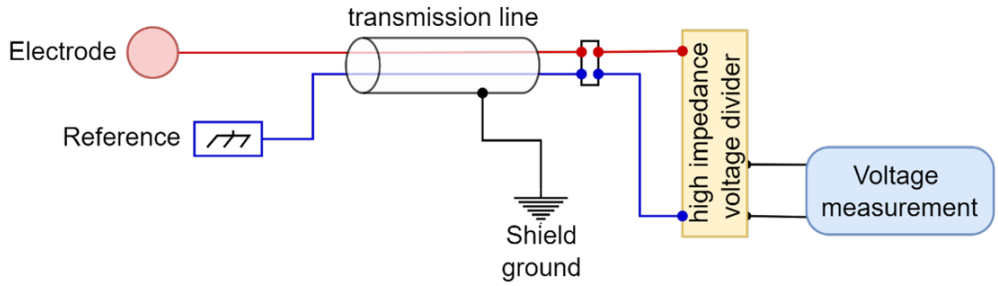

Figure 3.4: Schematic setup for practical floating potential measurement.

electrode and that V_f can be either positive or negative, this measure helps in defining a safe sweep range for the probe and its characteristic.

3.2.3 Single probe ion saturation current

The ion saturation current, being less susceptible to sheath phenomena, offers a good estimation of the plasma density. It requires a single, negative DC source that can be generated forcing the biasing power supply to its minimum output voltage value, i.e. $-100V$. The schematic if this configuration is shown in Figure 3.5 The advantage of this configuration is its ability to give a measurement of plasma density fluctuations with high time resolution.

3.2.4 Double probe characteristic

A more safe way to measure a characteristic curve for a probe, without incurring in the issues relative to high electron saturation current, is the double probe configuration. The reliability of

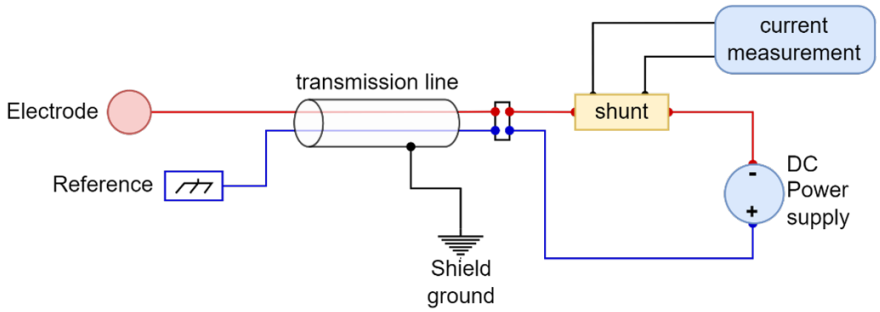

Figure 3.5: Schematic setup for a single probe ion saturation current measurement.

this set up is an intrinsic current limitation due to the configuration itself. However, its sensitivity to current leakages, especially in poorly arranged setups, makes it of no easy realization. Thus, having floating potential power supply and galvanic isolation to minimize current leakages become essential features. In Figure 3.6 the schematic set up and its characteristic are reported. The double probe characteristic can still be used to estimate the electron temperature Te, even if it trades its robustness with a less precise measurement.

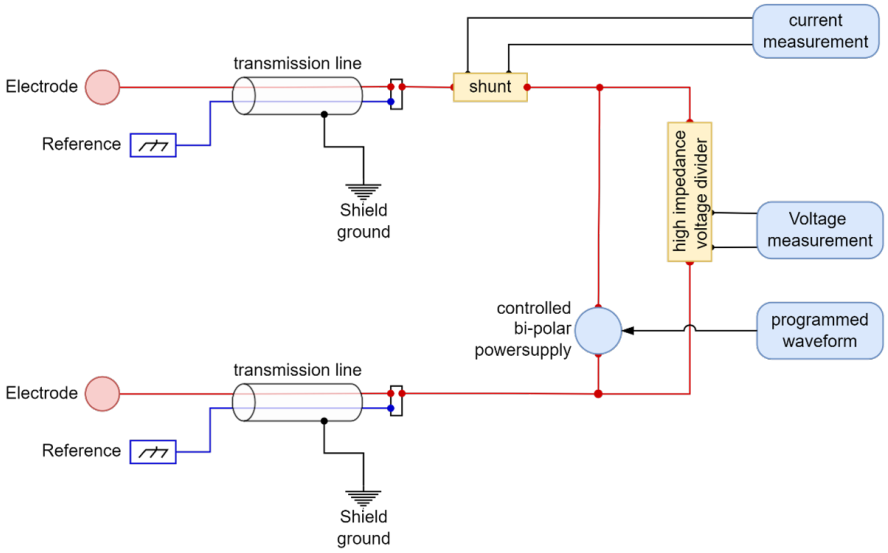

(a) Double probe characteristic measurement set up.

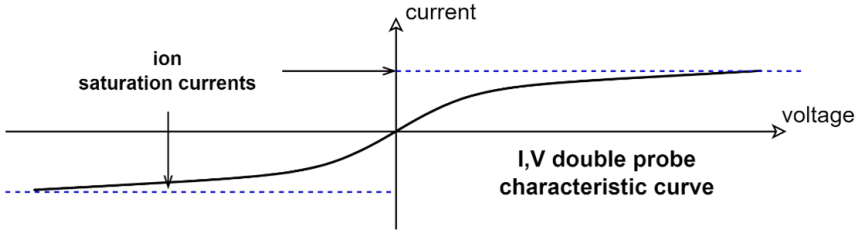

(b) Example of an ideal double probe characteristic.

Figure 3.6: Double probe measurement set up and its corresponding characteristic.

3.3 General system description

EPICA is part of the diagnostic system of MITICA. The purpose of EPICA is to manage several simultaneous voltage-current measurements, in compliance with the ITER CODAS standards and constraints. As mentioned in the introduction of the chapter, the environment in which the measurements have to be carried out is a highly EMI environment, where continuous Radio Frequency (RF) disturbance and random high-voltage spikes, due to the proximity of arc-discharges phenomena, are constantly present during the measurements. A direct consequence is the generation of high voltage random electric potential differences between the reference ground of the probes and that of the data acquisition system which, if not properly handled, can affect the measurement and damage the surrounding electronic. The traditional approach of using differential high impedance inputs doesn't appear the best choice. This method, largely used in the past thanks to a combination of low costs and relative simplicity in the realization, suffers, however, from high frequency disturbance. Moreover, the need of protection components at the input hamper the measurements. Nowadays, dedicated integrated circuit (IC) components for high voltage isolation handling of signal and power control are attractive, combining competitive price and ease of use.

3.3.1 Module management

The first point to consider for the design the total number of sensors. These sensors are installed on MITICA in three components: 1) The neutralizer, in which are used 62 probes, for a total of 4 modules, 2) The Residual Ion Dump, in which 3 modules are used, for a total of 48 probes and 3) The Calorimeter, in which 14 modules manage 102 probes. Table 3.1 sums up the data listed. A

MITICA component	Probe number	Modules number
Neutralizer	62	4
Residual Ion Dump	48	3
Calorimeter	102	14

Table 3.1: Plasma diagnostic techniques.

reasonable choice in terms of feasibility for installation is to have each module managing a total of 16 probes. Because several probes are foreseen to be also used in "double probe" configuration,

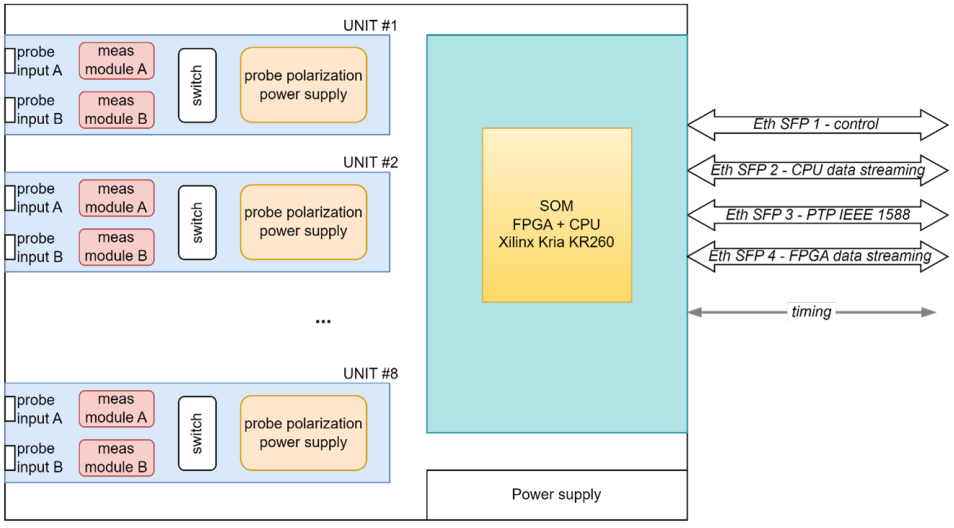

Figure 3.7: MITICA module anatomy.

to reduce the size and cost of the system, it has been decided to use one single biasing power supply for each couple of probes. The choice poses some limitations for the connections of the probes, but had been deemed manageable. So the decision of the number of probes per module is a tradeoff between cost and flexibility of a system itself. Figure 3.7 shows the anatomy of the module. The three main part of the system are explained in the following. Two channel (2CH) units are discussed more in details in the following two chapters.

3.3.2 SOM - Data interface

The core of the the module is the System On Module, which is a combination of both a CPU and a FPGA. The integration of the two digital devices allows the system to manage a great amount of external stimuli and task without incurring in memory saturation or slowdowns of the system. Device configuration and data transfer take place via Ethernet, in compliance with the general ITER CODAS specifications [12] [13]. The system shall provide four different Ethernet interfaces, each one used for a specific role:

- Device configuration and management
- Bulk diagnostic data transmission
- Timing through PTP/IEEE 1588
- Real time data transfer

In addition, a micro-SD holder will be placed, along a USB port, so as to allow for software upgrade and debugging. Along with a dedicated Ethernet line for timing purposes, also two additional lines, to be used for testing and possible simplified set ups, are to be placed in the final design: one allowing for clock input/synchronization and the other one used as trigger. These inputs are linked into the FPGA, leaving the possibility to redefine their capability for handling different synchronization standards. In addition, one of the Ethernet port has to be assigned to allow the system for a proper management of data stamping using IEEE-1588 Precision Time Protocol (PTP) standard as an absolute timing reference.

3.3.3 2CH unit description

As described above, each module is composed by 8, fully independent, two channels (2CH) units. The 2CH unit is the board in charge of managing the probe and the analog to digital signal conversion. It is composed by the probes' input, the measuring modules, the switch section,

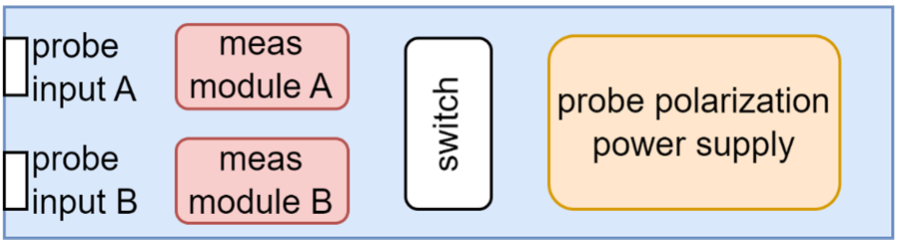

Figure 3.8: 2C unit board.

through which different kind of measurement can be performed and the probes' biasing power supply (see Figure 3.8). Each measuring module is composed by two $\Sigma\Delta$ ADCs, which carry out the voltage and current reading for the probe characteristic. Figure 3.9 shows the block scheme of the circuit to be developed. Further analysis is carried out in Chapter 4. The probe polarization power supply has the responsibility to generate the biasing voltage of the probe and to perform the voltage sweep to define the I-V probe's characteristic. The system is developed

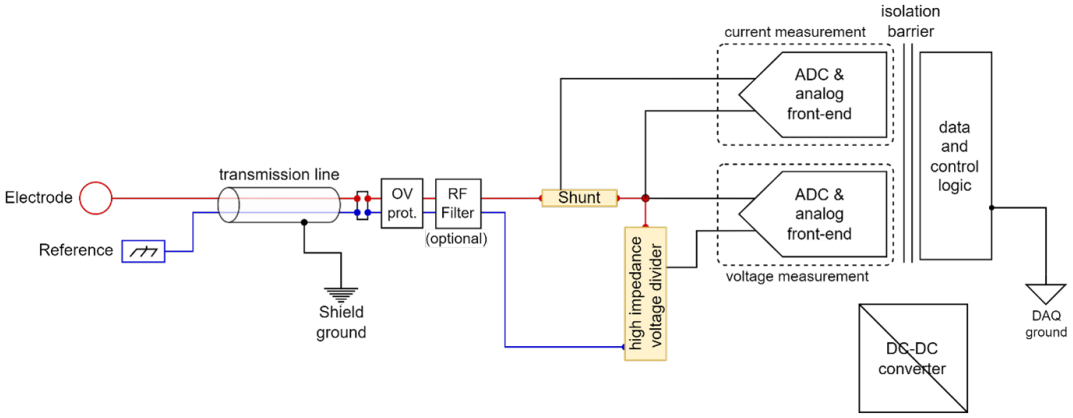

Figure 3.9: Single channel block scheme implementation. The DC/DC converter showed is for isolated power supply and is not the biasing power supply of the probes.

with the capability to sustain an high voltage range, spanning from $-100V$ to $100V$, even though in some cases the maximum voltage available to the probe is not greater than $30V$ (this situation in found in the electron saturation region, in which high currents can be encountered). Power ratings, however, are not prohibitive: the maximum output power is estimated to be $10W$. The sweeping frequency is set to be $50Hz - 100Hz$, even though it can go lower for high-density plasma. A proper management of the probe is needed, since it is an active power component: low voltage and current can be troublesome, therefore a bleeding resistor can be of use. Also for the biasing power supply, further analysis is proposed in Chapter 5.

3.3.4 Module power supply

The power supply of the module is a classical AC/DC converter: AC) 110-240V, 50 or 60 Hz, DC) up to 24V. An additional separate screw connector for the shielding ground shall be made available. In addition, possible optional features could include a "Wake-on-LAN" mechanism and an external DC power supply from a battery to provide a complete system galvanic isolation if needed.

Chapter 4

I-V curve measuring system

Through the measure of the probe's I-V characteristic it is possible to determine some important parameters relative to the plasma status, i.e., the plasma density, the ion and electron saturation currents and the electron temperature. As described in Chapter 2, from the probe characteristic,

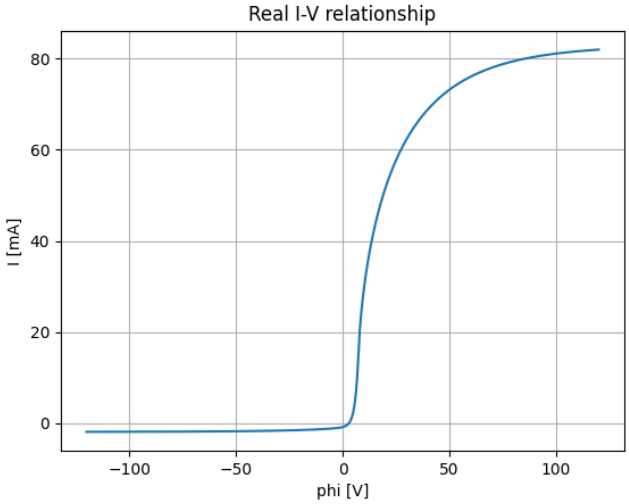

Figure 4.1: Typical I-V curve characteristic

depicted in Figure 4.1, all the data needed to understand the plasma status can be drawn, even though such derivation is not as straightforward as it may seem. However, in order to derive the above plot, a combined reading of both voltage and current is needed. In this chapter, a description of the work done to obtain a circuit that allows measuring the probe biasing voltage and output current as precisely as possible, taking as a starting point the constraints defined, is exposed, then supported by numerical simulations, with the extent to verify, at least in this early stage of the development, how the circuit behaves.

4.1 Sensing stage development

Figure 4.2 shows the basic layout scheme used as reference for designing the sensing stage of the diagnostic board. In the current reading, the ideal transfer function should be just the shunt resistance, giving:

$$V_{m1} = i_m \cdot R_S \rightarrow TF_1 = \frac{V_{m1}}{i_m} = R_S \tag{4.1}$$

in which i_m is the current generated by the probe. Applying the same line of thought to the voltage divider, one obtains:

$$V_{m2} = \frac{R_{v1}}{R_{v1} + R_{v2}} \cdot V_{bias} \rightarrow TF_2 = \frac{V_{m2}}{V_{bias}} = \frac{R_{v1}}{R_{v1} + R_{v2}} \tag{4.2}$$

in which V_{bias} is the bias voltage imposed by the power supply system, which value changes over time with a frequency of $50Hz - 100Hz$. Both the transfer functions do not take into account the loading effects of the ADC, which will then affect the measure, possibly leading the circuit out from the specifications above which it was developed.

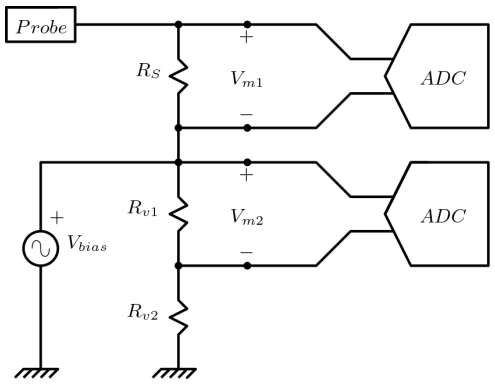

Figure 4.2: Basic implementation of the sensing stage.

4.1.1 Analog to Digital Converter (ADC)

Since the data collected are to be stored into a database, from which can then be retrieved to perform data analysis, there is the need to convert the analog signal into a digital one. The choice of the ADC to be employed is of paramount importance, since the accuracy and the precision both of the system and the measure depend on it. Moreover, due to the different references used and the high amount of noise coming from all the surrounding environment, it plays a key-role in the overall performance of the apparatus. Other important features of the ADC should be considered from the point of view of speed and precision of the measurement. The acquisition speed, i.e. the sampling frequency, has to be chosen so as to satisfy the time requirements, while trading for a number of bit so as to obtain the sought resolution. In addition, the effective signal bandwidth is not known, therefore, the latter is considered to be equal to the sampling frequency $f_S/2$. The ADC employed is a $\Sigma\Delta$ ADC and its building blocks are reported is Figure

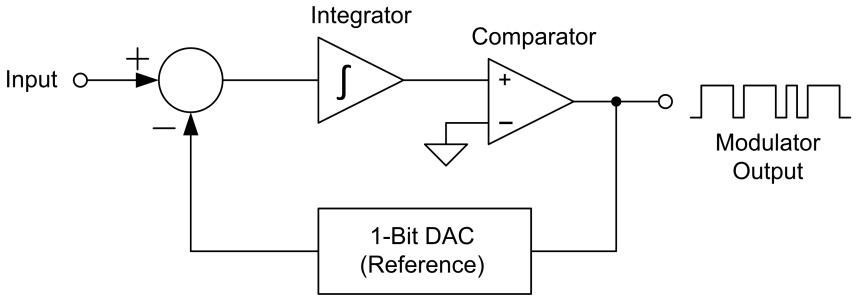

Figure 4.3: $\Sigma\Delta$ ADC block scheme.

4.3. Such family of ADCs can reach very good performances, even though a single-bit comparator is used. The sampling frequency is evaluated by applying the oversampling principle, in which the effective signal sampling frequency is given by:

$$f_S = \frac{F_{clk}}{OSR} \tag{4.3}$$

where OSR is the Over Sampling Ratio and F_{clk} is the frequency at which the 1-bit comparator is working. The output is a digital signal which is defined by a train of impulses. The instantaneous mean value of the output should be equal to the instantaneous amplitude of the input signal. To extract the wanted value, a low-pass filter is needed. However, taking into account the consideration made on the signal bandwidth, that doesn't satisfy the Nyquist-Shannon condition, there will be aliasing and the noise will be folded up around f_S.

Among a wide variety of possible ADCs, the choice fell upon the AD7405 of the Analog Devices. It is a 16 bit ADC which allows for a clock frequency ranging from $5MHz$ to $20MHz$. Moreover, such converter has the capability to perform differential voltage measurements. Another important feature of this ADC is the isolation between the input and the output channel. With this particular configuration the converted signal will not be affected by the same noise affecting the input. In addition, the digital electronic is safe from random voltage spikes that typically happens when dealing with plasma sources. Figure 4.4 describes the equivalent model of the input branch of the ADC. Such model allows for better simulation and results that are as

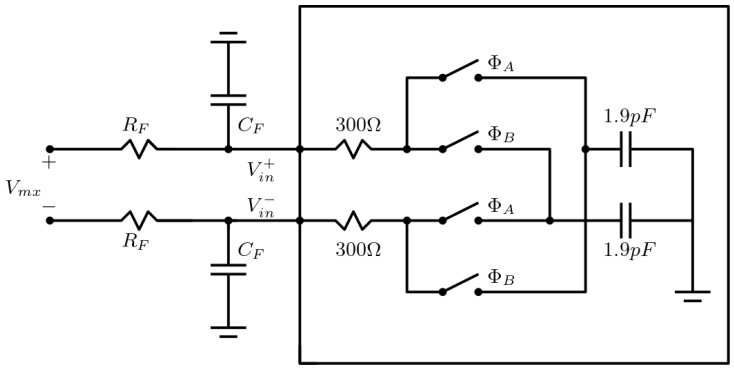

Figure 4.4: ADC input stage equivalent model. The sampling of the signal is made by means of two switched capacitors.

close as possible to the reality. The presence of the switched capacitors is source of a switching noise that propagates form the input back to the circuit, generating a ripple in the quantities to be measured. However, this latter part is addressed in a following paragraph.

4.1.2 Filtering and Bandwidth of the signal

The filtering is made by means of a digital implementation, through the use of a FPGA. The clock frequency is set to be at it's maximum value, i.e $20MHz$. Choosing the OSR directly affect the measure accuracy, since the rms-noise generated by the circuit is proportional to the square root of the bandwidth. In addition, also the effective number of bits changes in function of the OSR, as shown in Figure 4.5. A possible implementation of the acquisition system is to set different bandwidth so as to have the targeted accuracy for each measurement range (see Table 4.1). The bandwidth of interest are, however, $BW_1 = 50kHz$, $BW_2 = 78.125kHz$ and $BW_3 = 100kHz$. The data reported in the datasheet are referred to the performances of the ADC without $OSR = 256$. Therefore, a relation between OSR and the effective number of bits has to be exploited, if one wants to implement different bandwidth from those already found in the datasheet. Table 4.1 summarizes the main data for the ADC at the given frequencies. The

	$OSR = 200$	$OSR = 256$	$OSR = 400$
$f_S[kHz]$	100	78.125	50
$ENOB[bit]$	13.9	14.2	15

Table 4.1: ADC characteristics at different OSR.

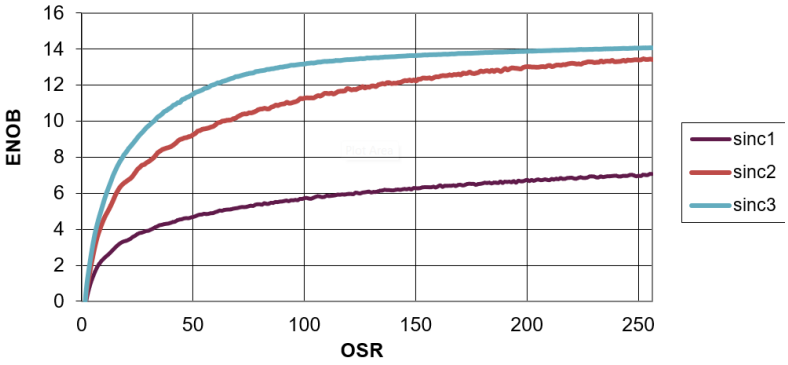

Figure 4.5: Variation of the ENOB in function of the over sampling ration OSR (courtesy of Texas Instrument).

red-colored number is extrapolated from the plot of Figure 4.5 by applying a linear law:

$$ENOB\Big|_{OSR=400} = 13.9 + \frac{14.2 - 13.9}{256 - 200} \cdot (400 - 200) = 15 \tag{4.4}$$

which is an approximation of the real behavior of the curve. As a reference for the following discussion, the case in which $OSR = 256$ is taken into account.

4.1.3 Current sensing

The measure performed to determine the current's magnitude generated by the probe is made by means of a shunt resistor. The resulting differential voltage is then sampled at a frequency f_S by a the ADC above mentioned and then transmitted to the FPGA. In Table 4.2 the requirements for the current measure are reported. It can be seen that a single shunt-resistance cannot be employed, since a current of $i_m = 1A$ flowing through a resistance of tens of Ohm would generate a differential voltage far above the maximum allowable by the ADC. Thus, a series of switched resistors has been used to overcome the problem. Each resistor has a value such that if the

Measurement Range	Minimum Nominal Resolution	Maximum Residual Noise
$\pm 1mA$	$0.5\mu A$	$0.15\mu Arms$
$\pm 10mA$	$5\mu A$	$1.5\mu Arms$
$\pm 100mA$	$50\mu A$	$15\mu Arms$
$\pm 1A$	$0.5mA$	$0.15mArms$

Table 4.2: Current measurements requirements.

maximum corresponding current is flowing through it, then the differential voltage at its ends doesn't exceed V_M. The system should operate at a maximum temperature of $323K$, which is thus taken to evaluate the Worst Case Scenario (WCS).

The system is designed to reach a maximum nominal value of $V_M = \pm 300mV$, even though the differential FSR for the AD7405 is $FSR = \pm 320mV$, leaving the remaining voltage to account for possible fluctuation. Given the ADC's FSR, the minimum readable change of the shunt voltage is given by:

$$\Delta_V = \frac{FSR}{2^{ENOB}} \simeq 34\mu V \tag{4.5}$$

Such variation has to be converted into a current one, but in order to do so, the shunt resistor values must be chosen. Even though the best performances of the ADC are given in a $\pm 250mV$ range, the FSR has been taken into account due to the full excursion of the measured signal,

that is in fact $\pm 320mV$. Even though the best resolution is given in the specified range, good performances can be reached also within all FSR.

The noise generated by the resistance, taking into account the WCS, has to be smaller than the one reported in Table 4.2. Also, the same noise has to be much smaller than Δ_V, otherwise we would loose the effective 14.2 bits of the ADC. Those two considerations translate into a system of inequalities:

$$\begin{cases} \sqrt{4k_BTR_S}\sqrt{BW} \leq R_S \cdot 0.15 \cdot 10^{-6} Arms \\ \sqrt{4k_BTR_S}\sqrt{BW} \leq \frac{\Delta_V}{10} << \Delta_V \end{cases} \tag{4.6}$$

in which R_S is the unknown shunt resistance value and BW is the bandwidth taken into account. Solving the inequalities for R_S gives an upper and a lower bound for the possible values, which spans several orders of magnitude:

$$77m\Omega \leq R_S \leq 6.7k\Omega \tag{4.7}$$

Having a broad range of possible values, the only constraint, and the most important, left to satisfy is having a maximum differential shunt voltage $\leq V_M$, limit that leads to choose the values reported in Table 4.3. Talking of apparatus meant to satisfy strict standards, the resistors need to be of niche performances. More in detail, a small tolerance is required due to both the high sensitivity of the measure and to the ability of the system to measure small-magnitude currents. Also the temperature drift has to be taken into account, since for the same reasons mentioned, resistors values cannot vary significantly. All this constraints leads to choose the resistors with accuracy. A good choice is to use metal film resistors, which features small tolerances and small TCR (Temperature Coefficient of Resistor). With such values, the minimum current resolution the ADC can measure with no background noise is $\Delta_I = \Delta_V / R_1 = 113nA$. The same values can

Measurement Range	Resistance
$\pm 1mA$	$R_1 = 300\Omega$
$\pm 10mA$	$R_2 = 30\Omega$
$\pm 100mA$	$R_3 = 3\Omega$
$\pm 1A$	$R_4 = 0.3\Omega$

Table 4.3: Shunt resistors values.

be chosen with the different OSR previously given. The only difference is that, for $OSR = 400$, the "much smaller" condition in Eq. 4.6 is not satisfied.

In figure 4.6, two possible configuration for the shunt resistances placement are shown. The switching between the resistors is performed by a series of relays, suitably controlled by the FPGA. However, the relays have an intrinsic parasitic resistance that can affect the measure of

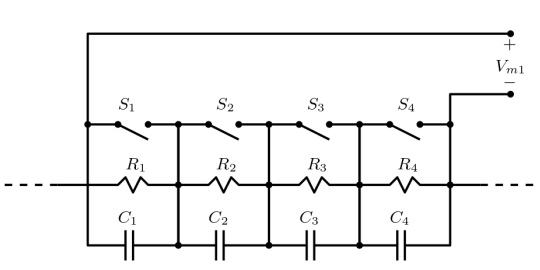

(a) Series implementation.

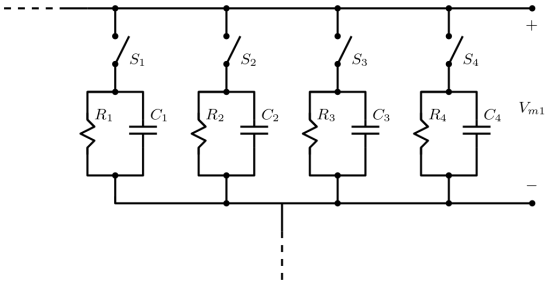

(b) Parallel implementation.

Figure 4.6: Proposed shunt measurement schemes.

the current, specially when small value resistances are selected. As consequence, the schemes proposed in Figure 4.6 are not a suitable solution.

- Figure 4.6a shows a series implementation of the shunt resistors. In order to isolate the resistance needed for the corresponding current range it is necessary to turn off its relay, while keeping active all the other. However, the active relays will result is series with the chosen resistance, thus affecting the entire measure with their contact parasitic resistance (specially when 0.3Ω resistors are employed). Moreover, the power consumption is also matter of discussion, since three out four relays are always in an active state.

- The second implementation shown in Figure 4.6b overcome the power-consumption problem with a parallel implementation. Nevertheless, the presence of the contact resistance of the relay is still affecting the measurement, even though in a small measure with respect to the previous implementation.

The aim to have a measure that is not affected by the presence of the relays, or at least that the effects of such problem aren't of great concern, cannot be achieved through just a single-contact relay. Therefore, a scheme with double-contact relays is preferred in place of single-contact ones, thus allowing for the measure to not be affected by the bespoken resistance, leading to the scheme of figure 4.7. With this configuration, only the filtering resistance is affected by the

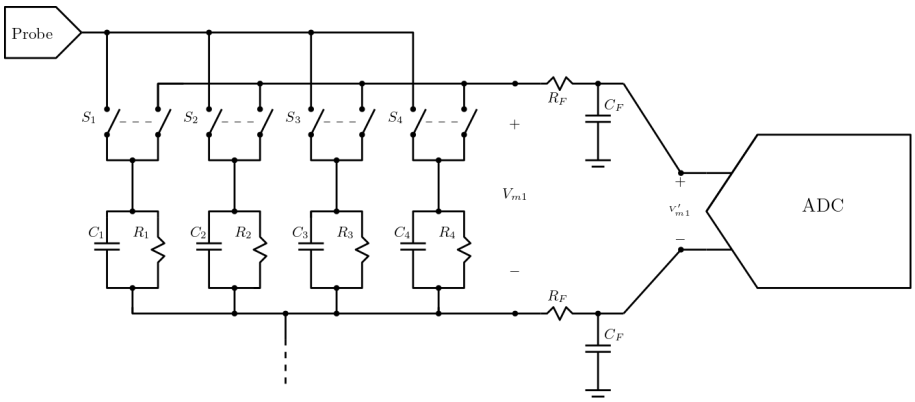

Figure 4.7: Final shunt measurement scheme.

relay's parasitic resistance. The tolerance of the filtering resistor, which has no constraint as strict as the shunt one, should cover this latter effect.

Thermal Noise

In order to determine the thermal noise impact into the measuring system, the WCS is considered. In this way, an idea of the upper bound of such noise is given. The WCS is given when the temperature reaches its maximum value and when the highest-valued resistance is used, that is because the heaviest constraint is specified at the smallest current range. Therefore, the maximum Power Spectral Density (PSD) of the shunt resistance is:

$$PSD_{R_S} = 4kTR_1 = 5.349 \cdot 10^{-18} \frac{Vrms^2}{Hz} \tag{4.8}$$

Also the resistances used to make up the two filters at the ADC's inputs accounts like a noise sources, each one having a PSD equal to:

$$PSD_{R_F} = 4kTR_F = 0.178 \cdot 10^{-18} \frac{Vrms^2}{Hz} \tag{4.9}$$

As mentioned earlier, the sampling frequency is $f_S = 78.125kHz$, which is also the signal's bandwidth BW. For this reason, there will be aliasing, resulting in a noise contribution related to the latter effect after the filter of the $\Sigma\Delta$ ADC. Having placed a low-pass filter at the input of

the ADC, the measuring point is moved after this latter component. In Figure 4.7 the measuring points are named V'_{mx}. However, when dealing with thermal noise, and noise in general, an advisable procedure is to take into account the transfer functions that relate each noise source with the quantities of interest, in this case being V'_{m1} and V'_{m2}. Such point is addressed in a following paragraph.

ADC switching noise

As shown in figure 4.2, the equivalent circuit representing the ADC's input includes two switched capacitors, which can be modeled as an equivalent resistance. Nevertheless, such modeling doesn't take into account for the noise transmitted back from the ADC inputs, generated by the switching of the capacitors. This effect should translate into a ripple in the quantities to be measured, such as the voltage V'_{m1}, V'_{m2} and, thus, i_m. To avoid this inconvenient, a capacitor has been placed in parallel to the selected shunt resistor. The capacitance's values was chosen as to have a cut-off frequency much smaller than the switching frequency $f_{SW} = 20MHz$ ($f_{cut_1} \simeq 2MHz$ should suffice). In Table 4.4 the proposed values for the capacitors, allowing for a cut-off frequency $f_{cut_1} = 1.9MHz$ are reported.

Measurement Range	Resistance [Ω]	Capacitance [nF]
$\pm 1mA$	$R_1 = 300$	$C_1 = 0.47$
$\pm 10mA$	$R_2 = 30$	$C_1 = 4.7$
$\pm 100mA$	$R_3 = 3$	$C_1 = 47$
$\pm 1A$	$R_4 = 0.3$	$C_1 = 470$

Table 4.4: Shunt resistors and filtering capacitors values.

4.1.4 Voltage sensing

In order to determine the probe's biasing voltage it is necessary to place a high-impedance voltage divider, since the differential input of the ADC has a $FSR = \pm 320mV$, and the biasing system voltage spans from $-120V$ to $120V$. The probe biasing is carried out by the controlled voltage source V_{bias} shown in Figure 4.2. The circuit used to perform the measure is shown in figure 4.8, in which also the ADC's input stage is depicted. The requirements for such measure are

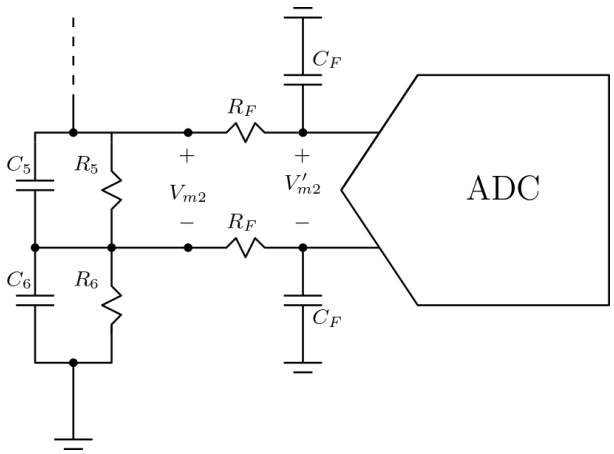

Figure 4.8: Voltage measurement scheme.

reported in Table 4.5. The minimum appreciable voltage variation is still Δ_V, but in this case the constraint related to the noise are not as stringent as for the current. To design the voltage divider, the resistor R_5 was designed so as to reach a voltage of $V_{R_5}^{set} = \pm 250mV$ at its ends

Measurement Range	Minimum Nominal Resolution	Maximum Residual Noise
$\pm 120V$	$50mV$	$15mVrms$

Table 4.5: Voltage measurements requirements.

when the biasing power supply reaches $V_{bias}^{set} = \pm 100V$, and to keep the remaining voltage as a buffer to account for possible fluctuation. Also, the differential voltage should not be greater than the maximum specified by the ADC datasheet, but the two constraints may not converge to a solution. A trade off must be found between the two restrictions. Sizing the components with the maximum allowed differential voltage should give a satisfying compromise:

$$R_5 = R_6 \frac{\frac{V_{R_5}^{max}}{V_{bias}^{max}}}{1 - \frac{V_{R_5}^{max}}{V_{bias}^{max}}} = \alpha R_6 \tag{4.10}$$

and, by setting the value for R_6, R_5 will come as easy. The values found are reported in Table 4.6. Since the biasing power supply sweeps form $-120V$ to $120V$, it's advisable to ensure that V_{m2} doesn't surpass $320mV$, hence:

$$V_{m2}^{max} = \frac{R_5}{R_5 + R_6} |V_{bias}^{max}| = 319mV \tag{4.11}$$

which ensures the safe operation of the ADC. Two capacitor are placed in parallel to R_5 and R_6 with the purpose to filter out possible noise generated from the biasing power supply system, from the resistors itself and from other noise sources. The chosen values respect the proportionality between the two resistances, according to the physical law that rule the capacitive voltage divider. The values also are reported in Table 4.6. The resulting cut-off frequency will then be equal for

R_5 $[\Omega]$	$320.85 \rightarrow 320$
R_6 $[k\Omega]$	120
C_5 $[nF]$	5.6
C_6 $[pF]$	15

Table 4.6: Resistances values.

the pair of impedances, being $f_{cut_2} \simeq 88.4KHz$.

Thermal noise

The thermal noise constraints are not as restrictive as for the shunt measure, but still it's a good habit to at least estimate them, always taking into account the WCS.

$$\begin{aligned} PSD_{R_5} &= 4kTR_5 = 5.705 \cdot 10^{-18} \frac{Vrms^2}{Hz} \\ PSD_{R_6} &= 4kTR_6 = 2.139 \cdot 10^{-15} \frac{Vrms^2}{Hz} \end{aligned} \tag{4.12}$$

However, the same consideration done for the shunt measurement has to be done here, since this calculation do not take into account how the noise propagates from the corresponding source to the quantities to be measured.

ADC switching noise

As for the shunt measure, the feedback noise from the ADC can generate some ripple, thus creating an unwanted, potentially significant, background noise. Since the ripple's frequency should be the same as the ADC's switching frequency, the potential problem has been already taken care of by placing the capacitors C_5 and C_6, thus creating the cut-off frequency f_{cut_2}.

4.1.5 Total input noise

By applying the superimposition of effects, the contribution that all the resistors have to the two measurements can be easily estimated. First of all, there are a few coefficient to be defined, being the corresponding transfer function mentioned above:

$$\begin{aligned} \beta_1 &= \frac{R_1}{R_5 + R_6 + R_1} = 2.49 \cdot 10^{-3} \\ \beta_2 &= \frac{R_5}{R_5 + R_6 + R_1} = 2.65 \cdot 10^{-3} \end{aligned} \tag{4.13}$$

The total power spectral density at the port input is found as:

$$\begin{aligned} PSD_{m1'} &= PSD_{R_S} + 2PSD_{R_F} + \beta_1^2 \Big(PSD_{R_5} + PSD_{R_6} \Big) \\ PSD_{m2'} &= PSD_{R_5} + 2PSD_{R_F} + \beta_2^2 \Big(PSD_{R_s} + PSD_{R_6} \Big) \end{aligned} \tag{4.14}$$

Then, by integrating the two function above within the signal bandwidth one obtains:

$$\begin{aligned} Pn_{m1'} &= \int_0^{f_S} \Big[PSD_{R_S} + 2PSD_{R_F} + \beta_1^2 \Big(PSD_{R_5} + PSD_{R_6} \Big) \Big] df \\ &= f_S \Big(PSD_{R_S} + 2PSD_{R_F} + \beta_1^2 \Big(PSD_{R_5} + PSD_{R_6} \Big) \Big) \end{aligned} \tag{4.15}$$

$$\begin{aligned} Pn_{m2'} &= \int_0^{f_S} \Big[PSD_{R_5} + 2PSD_{R_F} + \beta_2^2 \Big(PSD_{R_S} + PSD_{R_6} \Big) \Big] df \\ &= f_S \Big(PSD_{R_5} + 2PSD_{R_F} + \beta_1^2 \Big(PSD_{R_S} + PSD_{R_6} \Big) \Big) \end{aligned} \tag{4.16}$$

From those results, it's quite straightforward to compute the RMS noise voltage as:

$$\begin{aligned} Vn_{m1'} &= \sqrt{Pn_{m1'}} = 668nVrms \\ Vn_{m2'} &= \sqrt{Pn_{m2'}} = 689nVrms \end{aligned} \tag{4.17}$$

In the port number one, i.e. the one relative to the shunt measurement, the current is transformed into a voltage, therefore the RMS noise current is found by:

$$In_{m1'} = \frac{Vn_{m1'}}{R_1} = 2.23nArms \tag{4.18}$$

The assumption of having a constant PSD over the signal bandwidth may lead to an over-estimation of the noise, specially for port 2, i.e $V_{m2'}$. By looking at the plot of Figure 4.13a and 4.13b, one can understand that the PSD is not constant and therefore its transfer function as a function of the frequency is necessary to a precise estimation. As it can be seen, the residual thermal noise account only for a $\sim$ 1.5% of the total noise allowed. It has to be reminded that the case analyzed is the worst-case scenario. Despite having supposed a bandwidth $BW = 78.125kHz$, also estimating the noise contribution at the other two bandwidths listed is advisable. In Table 4.7 are summarized the noise contribution for the system at each frequency. As far as the reconstruction of the signal is concerned, due to not having respected the Nyquuist-Shannon theorem, aliasing is expected. To account also for the overlapping of the noise frequency component, as a rule of thumb, the noise has to be multiplied by a factor of $\sqrt{2}$.

$BW\ [kHz]$	$Vm1'_{rms}\ [nVrms]$	$Vm2'_{rms}\ [nVrms]$	$Im1'_{rms}\ [nArms]$
50	535	551	1.78
78.125	668	689	2.23
100	756	778	2.52

Table 4.7: Noise contribution.

4.2 LTSpice simulation software

LTSpice is a highly reliable spice simulation software that allows for designing analog circuit schematics using a vast array of existing device models (or creating custom ones) and analyzing the circuit at every point through a waveform viewer. The software enables simulating the circuit under various analysis modes, the most important being:

a) Transient simulation, allowing for a non-linear analysis in the time domain

b) AC simulation: performing a small-signal analysis of the circuit by linearizing it around its operating point

c) Noise simulation: performs a stochastic analysis of the circuit's noise, linearized around its operating point

All the simulation performed and discussed and all the models created in this thesis are made possible by means of this software.

4.2.1 Probe SPICE model

Recalling the model explained in Chapter 2, the potential function is composed by the error function, which is not among the available functions of the SPICE. It is necessary thus to approximate such function. A good approximation is given by:

$$erf(x) \simeq erf'(x) = tanh(Ax + Bx^3) \tag{4.19}$$

in which setting $A = 167/148$ and $B = 11/109$ offers an approximation yelding an error smaller than $3.6 \cdot 10^{-4}$ [11]. In Figure 4.9 the error function against its approximation and the relative error are plotted.

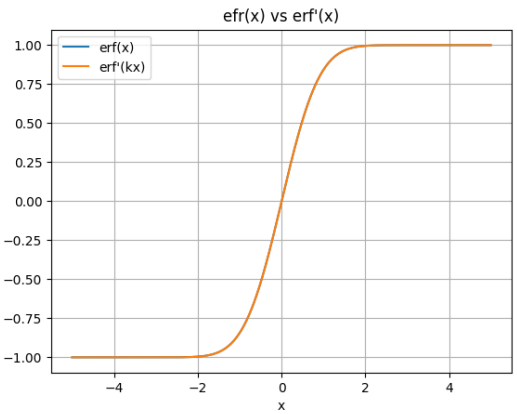

(a) Error function and its approximation.

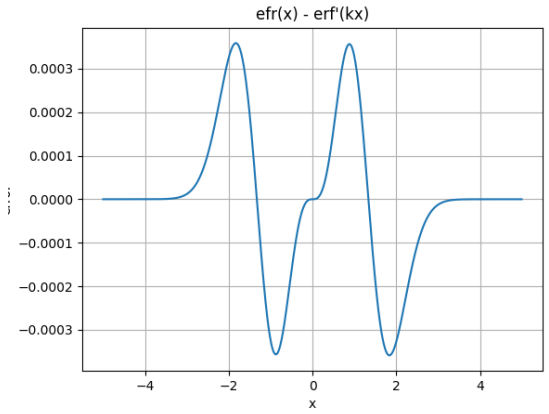

(b) Relative percentage error between the two functions.

Figure 4.9: Verification of the error function.

The circuit in figure 4.10 is used to test the correctness of the SPICE model of the probe. To verify the model operation, parametric simulations were performed and in the plots of Figure 4.11 the curves obtained are exposed. As expected, the characteristics are similar to the ones of Chapter 2. The only discrepancies are due to the SPICE program itself, that cannot handle very well certain operating points.

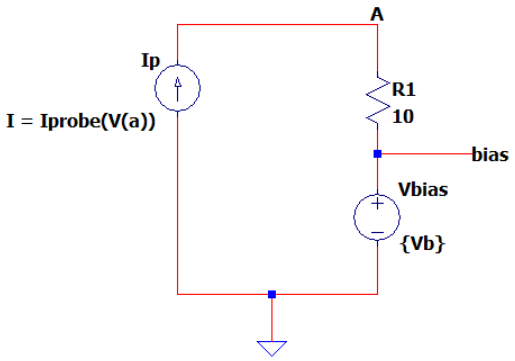

Figure 4.10: Spice probe implementation. Resistor R_1 is for simulation purposes only, thus not being a real component.

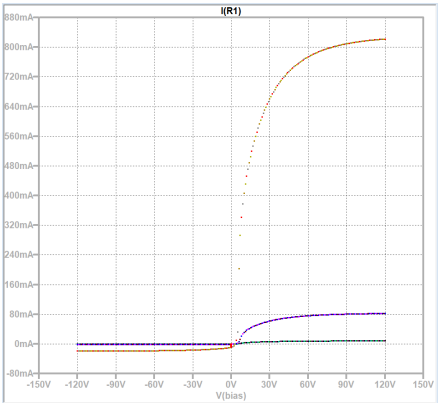

(a) Probe current generated with different densities.

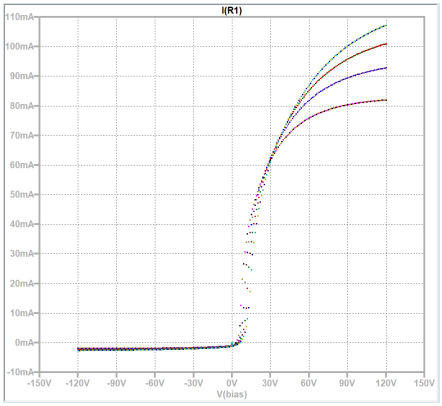

(b) Probe current generated with different temperatures.

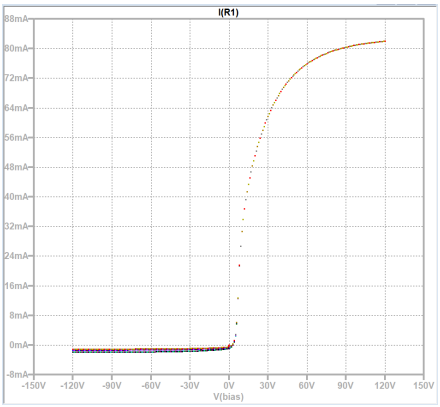

(c) Probe current generated with different ion species.

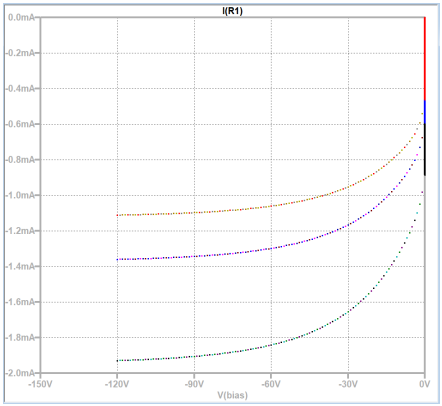

(d) Probe current generated with different ion species (this section is a zoom of the previous image, focused only on the ion saturation region).

Figure 4.11: Currents obtained from the probe SPICE model.

4.2.2 Floating Potential simulation

The purposes of this simulation are multiple: on one hand to verify if the noise constraints are satisfied with the components chosen and on the other hand to understand the frequency response of the system, in order to have an idea of its behavior. To this extent, the probe has been modeled as a variable voltage source, placing in series the sheath resistance. Figure 4.12 shows the circuit model adopted to perform the simulation, as better described in the following paragraphs.

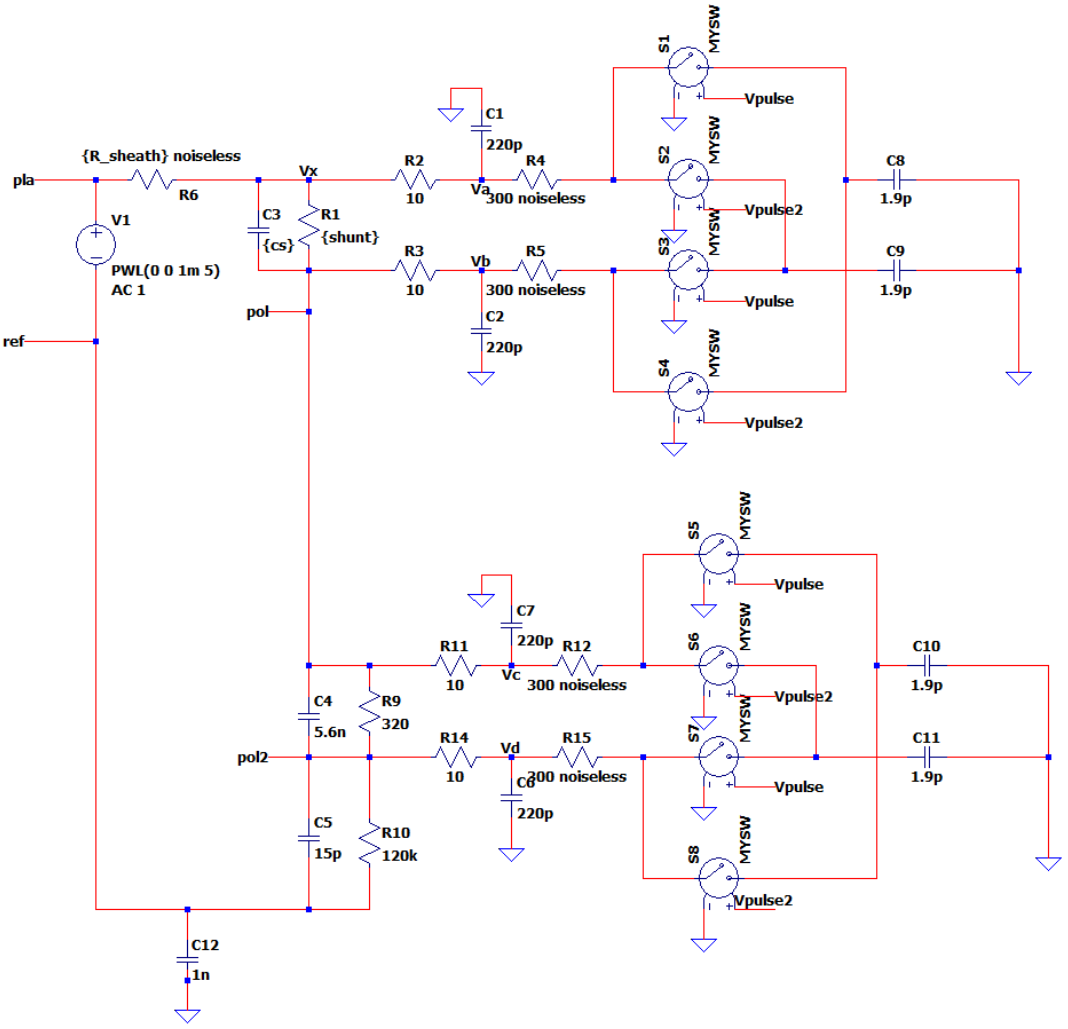

Figure 4.12: Circuit implementation for the floating potential SPICE simulations.

Figure 4.13a and Figure 4.13b highlights results that are coincident with what has been calculated in the previous section: $\sqrt{PSD_{m1'}} \sim 2.4nV/\sqrt{Hz}$ and $\sqrt{PSD_{m2'}} \sim 2.4nV/\sqrt{Hz}$, which give $Vn_{m1'} = 665[nVrms] \rightarrow In_{m1'} = 2.23[nArms]$ and $Vn_{m2'} = 623[nVrms]$. The noise parameter relative to the second port shows a minor contribution respect to what has been found in the previous computation, while the parameters with respect to the first port are coincident. This is due to the transfer functions' dominant poles: in the case of $Vn_{m1'}$, the pole is almost coincident with the bandwidth, not hampering the measure of the noise when integrating. In the case of $Vn_{m2'}$, however, it is shown that the dominant pole is smaller that the bandwidth, thus, the approximation of considering the noise constant is too much of an approximation. In any case, this latter comment is restricted only to BW_2 and BW_3. In the case of BW_1, the pole is far above the value of the bandwidth, therefore the noise can be considered constant without any approximation.

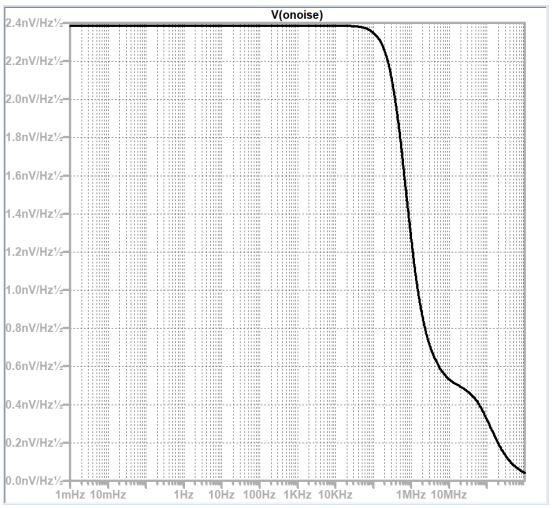

(a) $Noise(V'_{m1})$ with $R_{shunt} = 300\Omega$.

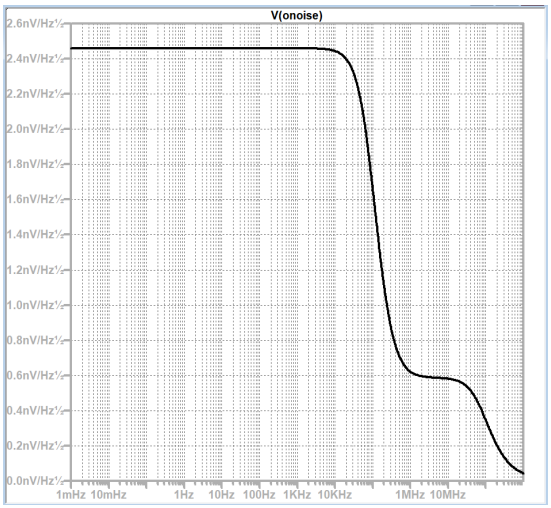

(b) $Noise(V'_{m2})$.

Figure 4.13: Noise plots.

In Figure 4.14a and Figure 4.14b are shown the noise TFs resulting from a parametric simulation, in which the parameters varied are the shunt resistors' values and the shunt filtering capacitance values. Moreover, the variation of such parameters do not affect by any means the transfer function of the high-impedance voltage divider (see Figure 4.14b). From the plots of Figure 4.15 it can be understood the importance of the shunt-resistance filtering capacitance. The attenuation introduced by the filter reduces the current ripple from $176nApp$ to $39nApp$ (Figure 4.15b). Reducing the maximum ripple to a value smaller than the maximum noise allowed ensures that the RMS value of the corresponding noise respects the given constraints. The plot of Figure 4.15a shows the same effect encountered in the shunt measurement on the voltage reading. However, having already placed the filtering capacitance in parallel to the resistor employed, the ripple isn't a concern, being of $1.2\mu V$.

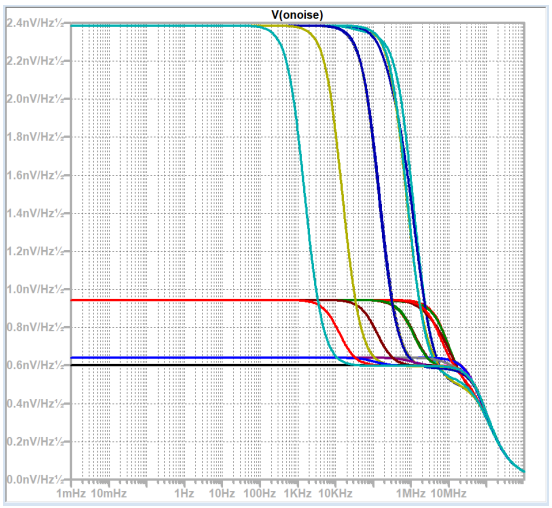

(a) $Noise(V'_{m1})$.

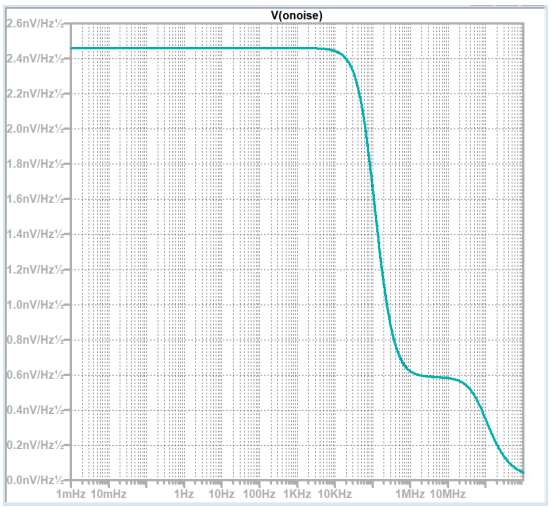

(b) $Noise(V'_{m2})$.

Figure 4.14: Noise plots with parametric simulations.

The last set of figures displays the frequency response of the quantities of interest, i.e. V'_{m1} and V'_{m2}. Regarding to the shunt measurement, the transfer function has a corner point at $1kHz$, after which the response start increasing its magnitude (except for one case only). The same effect happens to the voltage measurement. However, being the voltage sweep performed with a

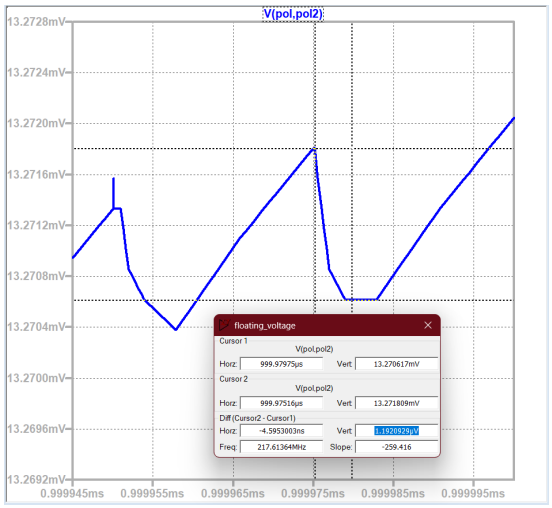

(a) Voltage ripple on the high-impedance voltage divider.

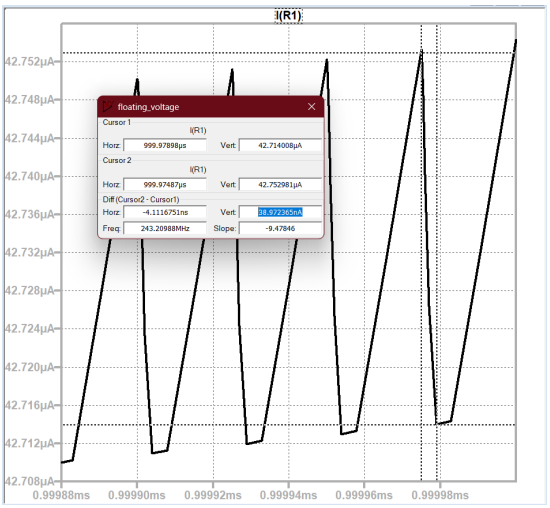

(b) Current ripple on the shut resistance when a filtering capacitance is applied.

Figure 4.15: Current ripple on the shunt resistance.

frequency not greater than $100Hz$, such frequency falls within the region in which the response is constant, thus not affecting the voltage measurement. In Figures 4.16a and 4.16b are shown the parametric simulation, which give an overall idea of the circuit behavior under various aspects.

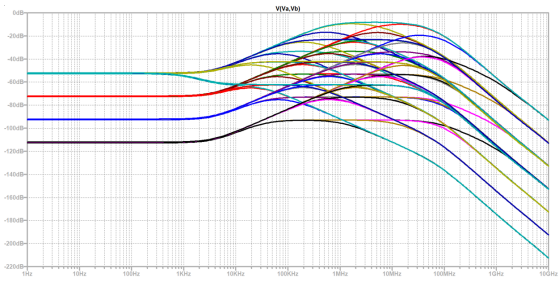

(a) Frequency response of V'_{m1} with the parametric variations.

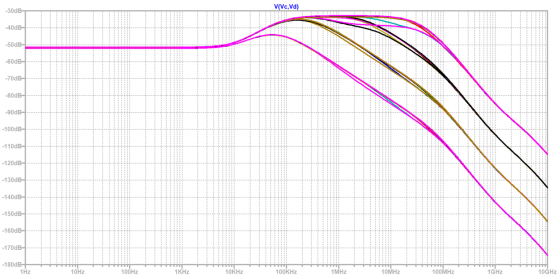

(b) Frequency response of V'_{m2} with the parametric variations.

Figure 4.16: Frequency response of the voltages to be sampled.

Overall, the main results to pay attention to are those relating to the noise, which can be summed up as in the following:

- Thermal noise: coming from the electron movement, it's magnitude is significantly smaller than the specified constraint, even accounting the aliasing effect (that can be seen only in the measuring system), and thus not being a serious problem for the measure itself.
- Switching noise: coming from the ADC input as a "feedback" noise, introduces some ripple in the quantities to be measured, rising some problems specially for the current measurement. To avoid the interference, filtering capacitors have been placed in parallel to the resistors.

4.2.3 Single Probe measurement

For the single probe measurement, the circuit schematic of Figure 4.12 was modified by replacing the voltage source with the probe model and by adding the biasing voltage to its corresponding

point. The circuit is shown in figure 4.17. The objective of this simulation is to analyze if and how the switching noise will impact the reading of the quantities of interest, hence to verify if the rationale of the design process is correct. On the other hand, a second purpose is to verify the behavior of the circuit when pushed to its limit, that is, in condition of high currents and high biasing voltages.

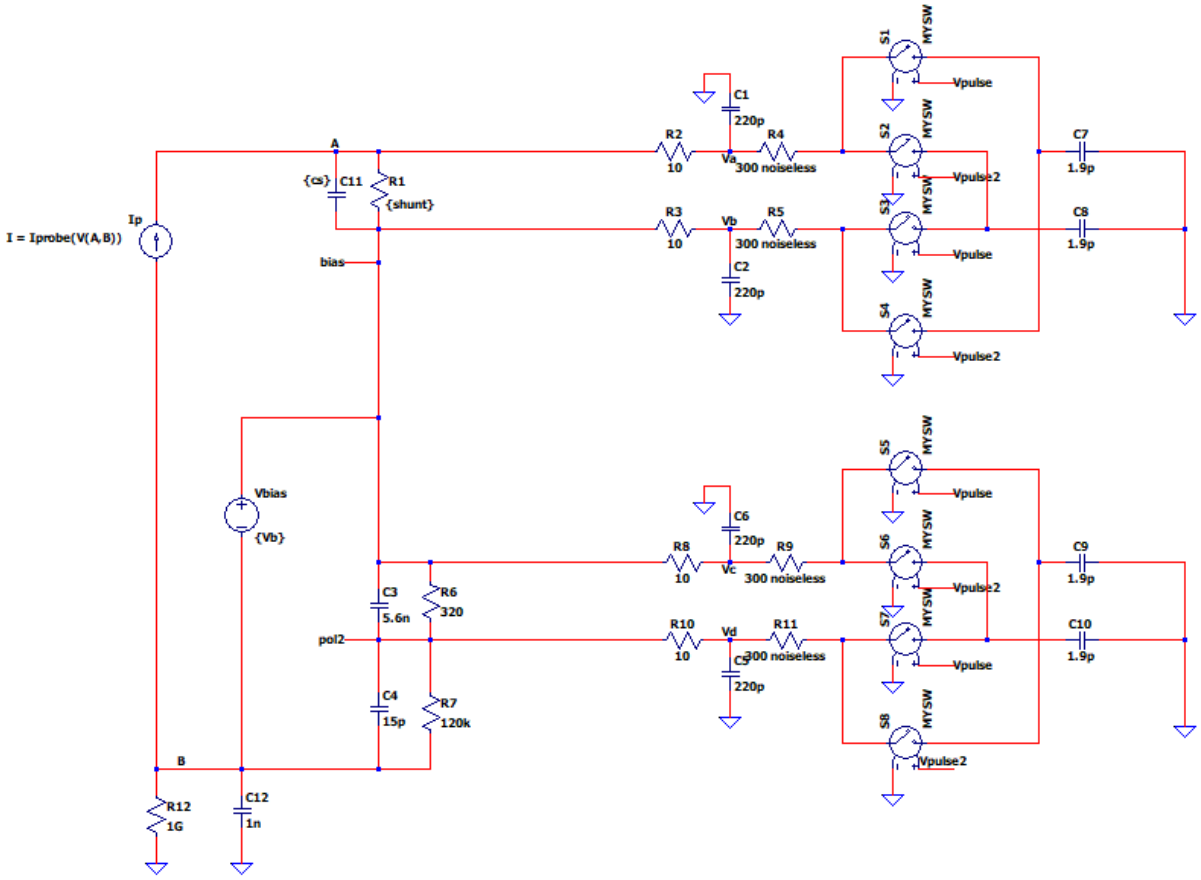

Figure 4.17: Circuit implementation for the single probe SPICE simulations.

The first problematic is found to be of great impact whenever small currents are observed to be generated from the probe, that is, when the electron temperature T_e and the plasma densities n_e and n_i are the lowest possible. To determine the magnitude of this disturbance the peak to peak value of the shunt current is evaluated with respect to the biasing voltage. In figure 4.18 the variation of the current ripple as a function of the applied voltage is reported, showing $I_{PP} \simeq 0.2\mu App$ with the ion saturation current and $I_{PP} \simeq 1\mu App$ with the electron saturation current. Two simulation were performed, so as to have a characterization of the current ripple because the current exceeded the maximum threshold value of $1mA$ (that is the switching point at which there is the change between two shunt resistors - see Table 4.4). The second issue addressed is the behavior of the circuit at its limits. Looking that such boundaries are satisfied is the object of this simulation. The plots shown in Figures 4.19 and 4.20 shows the maximum and minimum values reached during the voltage sweep: Figure 4.19 shows the voltage behavior across the shunt resistance while Figure 4.20 shows the voltage behavior across the high-impedance voltage divider. Both plots show a good behavior, i.e., the constraints imposed during the designing phase of the project are respected. In Figure 4.19 the change of slope of the second line with respect to the first one is due to the change of the shunt resistance, but in any case the absolute maximum voltage do not exceed $V_{m1}^{max} = \pm 300mV$. By looking at Figure 4.20 it can be stated that the maximum voltage reached is $V_{m2}^{max} \pm 320mV$, as expected.

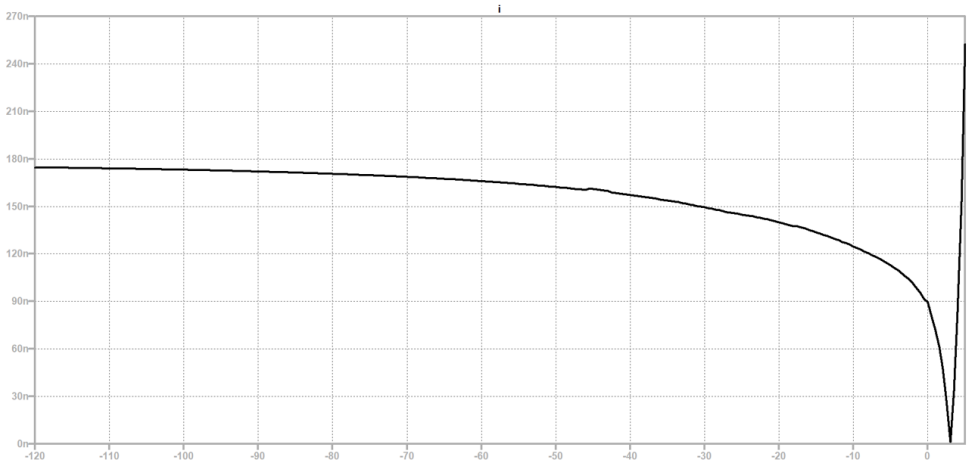

(a) Peak to peak current variation measured in the shunt resistance as a function of the applied voltage. $R_S = 300\Omega$ and $C_S = 470pF$ - The current is below the upper limit of $1mA$. The plot after the ripple goes to zero is not reliable, since the current values may reach values greater that $1mA$.

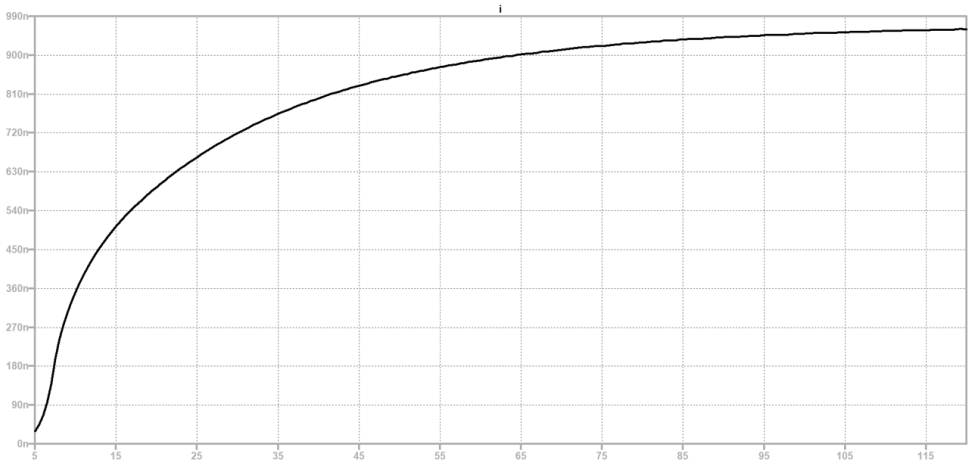

(b) Peak to peak current variation measured in the shunt resistance as a function of the applied voltage. $R_S = 30\Omega$ and $C_S = 4.7nF$ - The current is above the upper limit of $1mA$.

Figure 4.18: Ripple constraints verification.

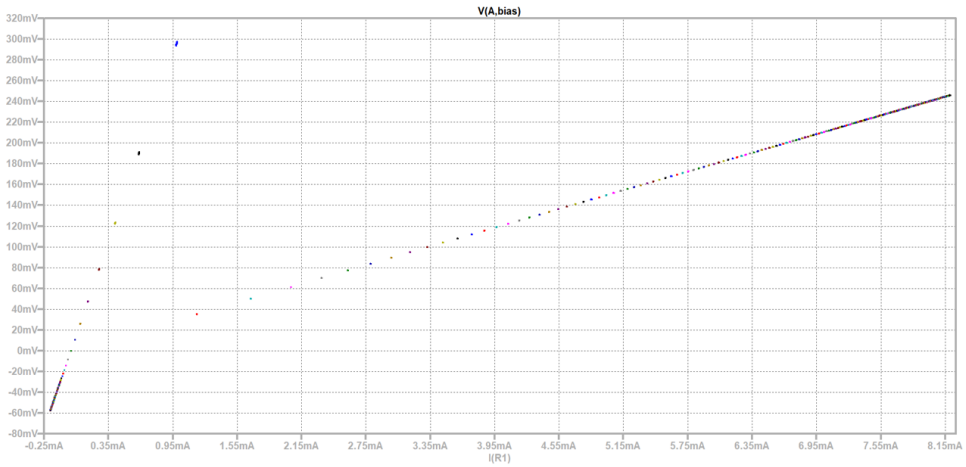

Figure 4.19: Voltage at the shunt differential input.

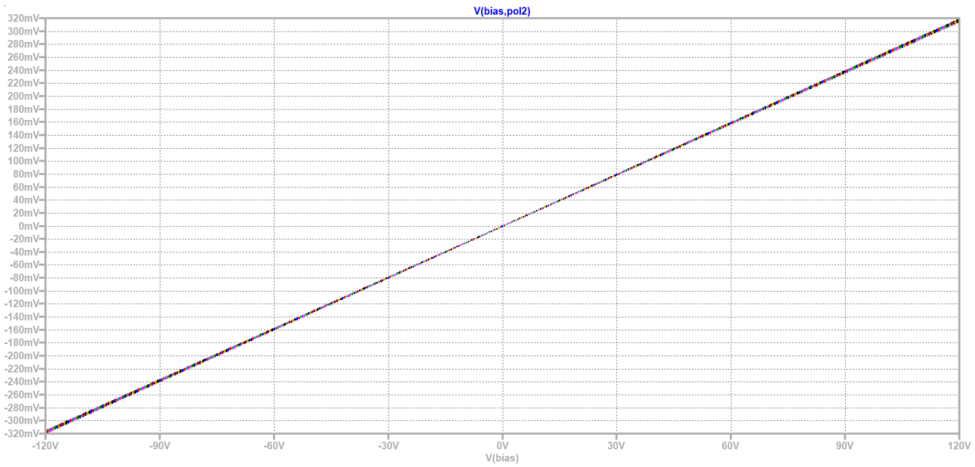

Figure 4.20: Voltage at the voltage divider differential input.

4.2.4 Double probe measurement

The double probe measurement is, as described in Chapter 3, an optimal procedure to retrieve plasma data without incurring in high electron saturation currents, that could be dangerous for the electronic. The electrical model differs from that of the single probe due to the presence of a second current generator (that is the second probe), placed in anti-series to the first one. In

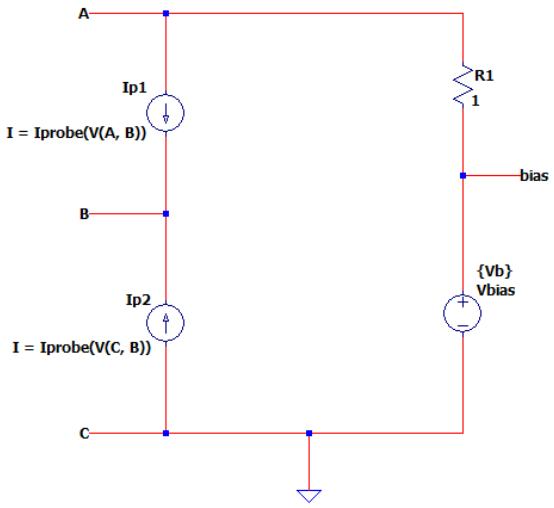

Figure 4.21: Double probe electrical model.

figure 4.21, contrary to what has been done with the single probe, R_1's current direction was taken positive if flowing toward Ip1. According to the measurement schematics, the voltages across each probe should be related by the following law:

$$\begin{aligned} V_{bias} &= V_{p1} - V_{p2} \\ &= V(A,B) - (-V(B)) \end{aligned} \tag{4.20}$$

The characteristic found is then the one shown in Figure 4.22.

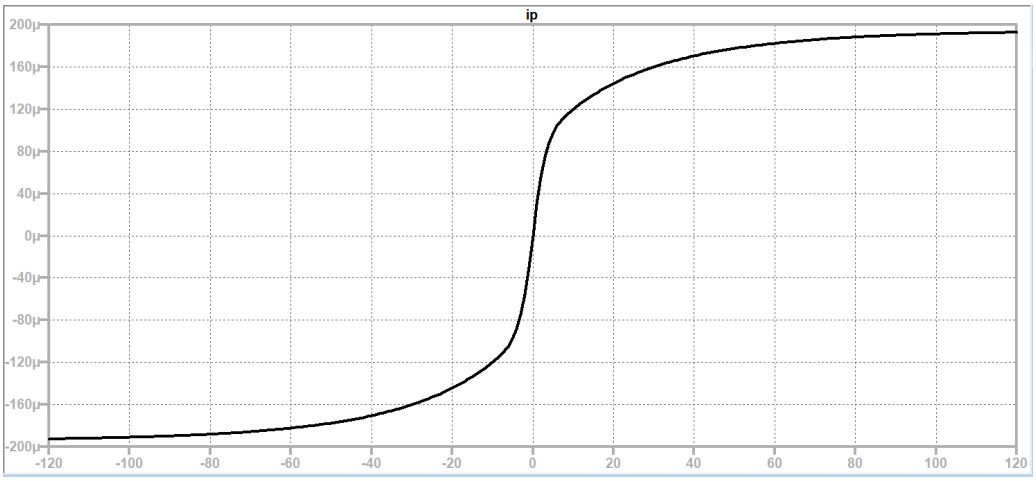

Figure 4.22: Double probe I-V characteristic.

4.3 Sum-Up Tables

The data reported in the following tables are extrapolated from the simulations as previously described and, therefore, are the one to be expected during real operation analysis. It has to

	Type of Meas.	Vn_{RMS}	In_{RMS}	N_{SW}
$BW = 50kHz$				
	Current	533 $nVrms$	1.78 $nArms$	39 $nApp$
	Voltage	525 $nVrms$	NR	1.2 μVpp
$BW = 78.125kHz$				
	Current	665 $nVrms$	2.48 $nArms$	39 $nApp$
	Voltage	623 $nVrms$	NR	1.2 μVpp
$BW = 100kHz$				
	Current	751 $nVrms$	2.5 $nArms$	39 $nApp$
	Voltage	675 $nVrms$	NR	1.2 μVpp

Table 4.8: Noise parameters found from the simulation with a different bandwidths.

	Type of Meas.	Vn_{RMS}	In_{RMS}	N_{SW}
$BW = 50kHz$				
	Current	754 $nVrms$	2.51 $nArms$	39 $nApp$
	Voltage	742 $nVrms$	NR	1.2 μVpp
$BW = 78.125kHz$				
	Current	940 $nVrms$	3.13 $nArms$	39 $nApp$
	Voltage	881 $nVrms$	NR	1.2 μVpp
$BW = 100kHz$				
	Current	1062 $nVrms$	3.54 $nArms$	39 $nApp$
	Voltage	955 $nVrms$	NR	1.2 μVpp

Table 4.9: Noise parameters derived from the previous ones, accounting for the $\sqrt{2}$ aliasing factor.

be reminded that the noise parameters found in Table 4.9 are an estimation, therefore in the analysis of the real circuit, the measured values may not coincide with what it is reported.

4.4 Circuit Schematics

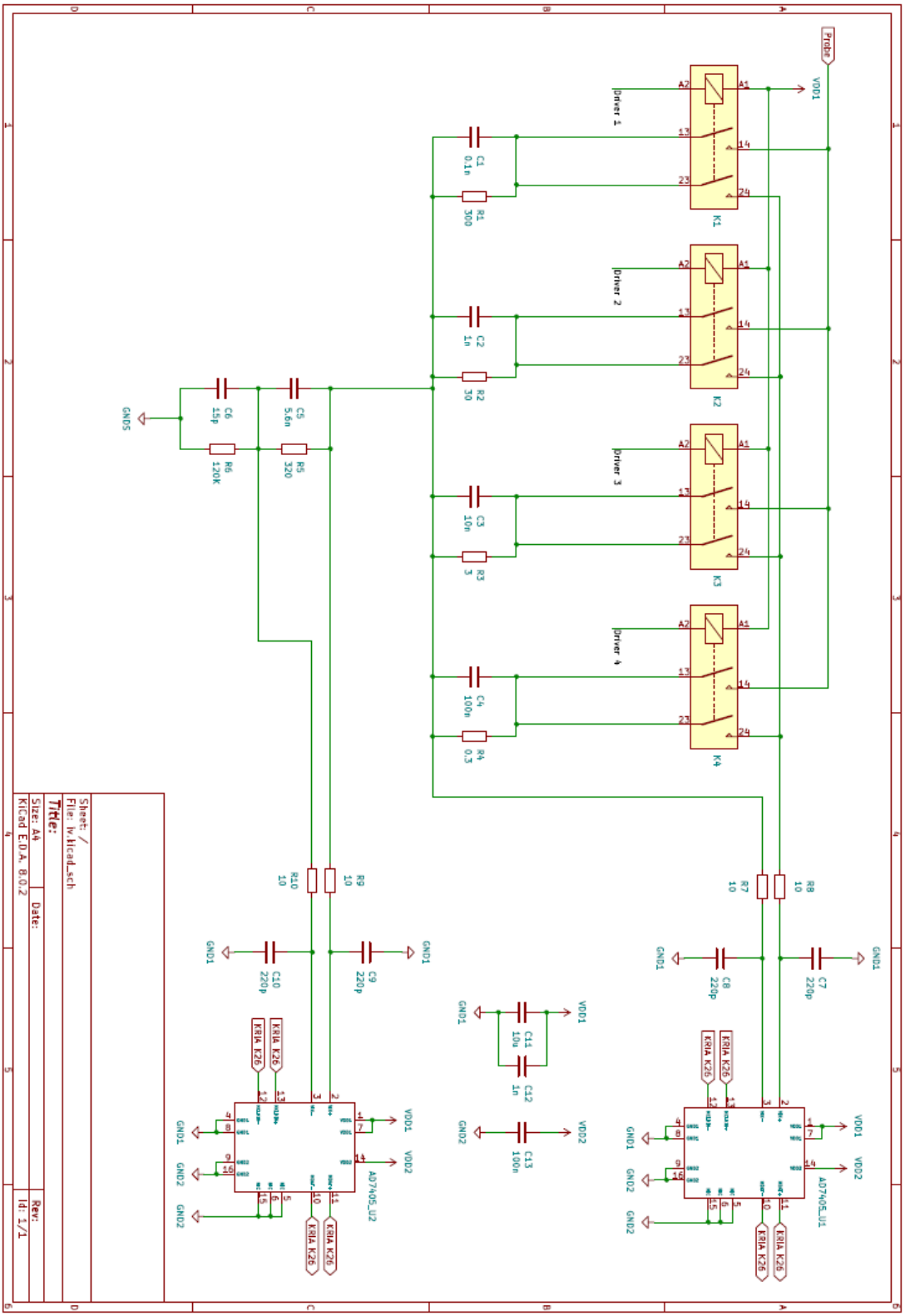

Figure 4.23: Circuit schematic.

Chapter 5

Biasing power supply

The power-core of the probe-to-ADC system is the biasing power supply which allows for the probe to be polarized and thus to generate the current needed to plot the I-V characteristic. The challenge is to develop a DC-DC converter that allows for the probe to be biased within a range of $\pm 120V$, even though in the final implementation the bespoke range is $V_{min} = -100V \div +100 = V_{max}$. The sweep frequency should not be above $f_{sweep} = 100Hz$. In Figure 5.1 is shown the scheme implemented to built up the biasing power supply. The circuit's core is the high-frequency power transformer.

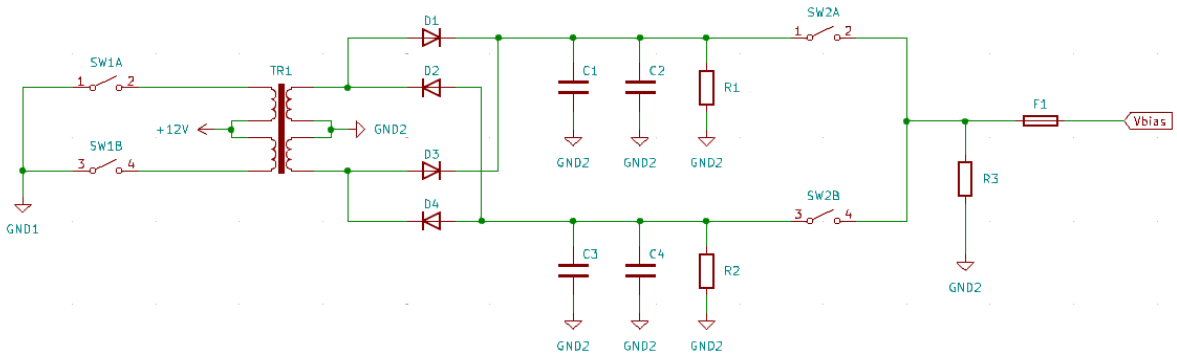

Figure 5.1: Proposed biasing power supply circuit.

Figure 5.1 proposes a DC-DC converter which allows the generation of a dual power supply. $SW1A$ and $SW1B$, in practice then realized with two MOSFETS, are responsible for the creation of a square wave which is then amplified by the transformer, rectified and filtered and then fed to the probe. While the presence and the role of the rectifying bridge and the filter may seem easy to understand, the same cannot be said about $SW1A$ & $SW1B$ and $SW2A$ & $SW2B$. The first couple of switches is responsible for the creation of a square wave but also for the PWM modulation through which the sweep is carried out. In fact, varying the duty cycle will also vary the mean value output by the filter, and therefore the biasing voltage at the circuit output. The role of the last two switches, also realized with two MOSFETS, is to change the polarity of the output biasing voltage once the sweep reaches $0V$.

5.1 Transformer: general theory

The magnetic transformer is a machine that, in an ideal case and without any mechanical movements, transfers electrical energy from its input winding, via a magnetic filed, to its output winding according to Faraday's law. It consist of two coils coupled together by a ferromagnetic core. This latter plays an important role in the transmission of the magnetic flux from one coil

to another. The equation that relates the input and the output voltage can be easily found if

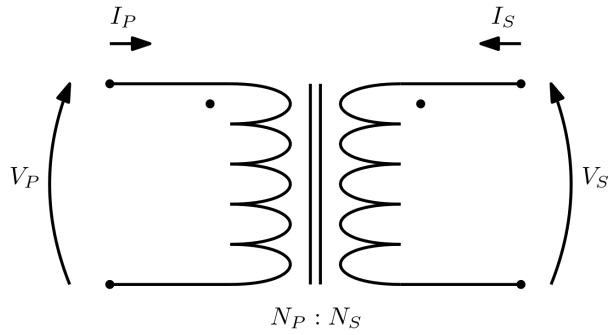

Figure 5.2: Transformer bipolar model.

one considers that all the magnetic flux generated by the primary solenoid is picked up by the secondary, i.e., there are no losses:

$$\begin{cases} V_S(t) = -N_S \frac{d\phi(t)}{dt} \\ V_P(t) = -N_P \frac{d\phi(t)}{dt} \end{cases} \tag{5.1}$$

It is straightforward to understand that such a machine is working only if the magnetic flux $\phi(t)$ is varying over time, that is:

$$\frac{d\phi(t)}{dt} = L\frac{dI(t)}{dt} = L\dot{I} \tag{5.2}$$

in which L is the self-inductance of the coil through which the current flows. Having a DC source at the input will not results in any energy transfer from the primary to the secondary side, hence no voltage can be measured at the output. The equation relating $V_S(t)$ and $V_S(t)$ is then:

$$\frac{V_P(t)}{V_S(t)} = \frac{N_P}{N_S} = n \tag{5.3}$$

Also, considering that the transformer is a passive components, there will not be any power amplification:

$$\begin{gathered} I_P(t)V_P(t) = I_S(t)V_S(t) = I_S(t)\frac{V_P(t)}{n} \\ \rightarrow \frac{I_P(t)}{I_S(t)} = \frac{1}{n} \end{gathered} \tag{5.4}$$

highlighting an inverse relationship with respect to the voltages.

5.1.1 Mathematical model

Being an electrical component that should be placed inside a circuit, it's necessary to create a model to understand how the transformer behaves. The following characterization is carried out according to the model shown in Figure 5.2.

An intrinsic characteristic of a winding is its self-inductance L, which is that inductance that results from the magnetic field generated by the coil current acting on the coil itself. It can be found directly from the Faraday's law:

$$emf(t) = -N\dot{\phi} = -NA_e\dot{B} = -NA_e\mu\dot{H} \tag{5.5}$$

in which $\mu = \mu_0\mu_r$ is the permeability of the portion of space in which the coil is placed and H is the magnetic fiel and B is the magnetic induction. Ampere's law states:

$$H = \frac{NI}{l} \tag{5.6}$$

in which l is the length of the coil. Therefore, the electromotive force generated by the coil is given by:

$$emf(t) = -\frac{N^2 A_e \mu}{l}\dot{I} = -N^2 A_L \dot{I} = -L\dot{I} \tag{5.7}$$

in which L expresses the self inductance of a coil with an effective area A_e, a length of l and a number N of windings. A_L is a characteristic of the medium in which the coil is placed.

When two or more solenoids are coupled together there is an action of mutual inductance in which the magnetic field generated by the first coil affects the second one and vice-versa. From Ampere's law:

$$\begin{cases} \phi_P(t) = N_P(t) I_P(t) \\ \phi_S(t) = N_S(t) I_S(t) \\ \phi_{SP}(t) = \phi_{PS}(t) = N_P(t) I_P(t) + N_S(t) I_S(t) \end{cases} \tag{5.8}$$

and from Faraday's law one can write:

$$\begin{cases} V_P(t) = N_P \frac{d(\phi_P + \phi_{SP})(t)}{dt} \\ V_S(t) = N_S \frac{d(\phi_S + \phi_{PS})(t)}{dt} \end{cases} \rightarrow \begin{cases} V_P(t) = L_P \frac{dI_P(t)}{dt} + M \frac{dI_S(t)}{dt} \\ V_S(t) = M \frac{dI_P(t)}{dt} + L_S \frac{dI_S(t)}{dt} \end{cases} \tag{5.9}$$

in which $M = \sqrt{L_P L_S}$. The above equations constitute the model of the transformer and can be rewritten in a more compact form:

$$\begin{pmatrix} V_S \\ V_S \end{pmatrix} = \begin{pmatrix} L_P & M \\ M & L_S \end{pmatrix} \begin{pmatrix} \dot{I}_P \\ \dot{I}_S \end{pmatrix} \tag{5.10}$$

5.1.2 Circuital model

The discussion made so far only takes into account an ideal transformer, that is, without considering the real components by which is composed. Such non-ideality may give rise to behaviors not accounted for that may invalidate the circuit itself. A first, non-ideal effect is the coupling factor that characterizes the mutual inductance M. Previously, this latter component was introduced as:

$$M = \sqrt{L_P L_S} \tag{5.11}$$

and it was found assuming that all the primary magnetic flux was entirely caught up by the secondary coil. However, close it may be to the ideal case, there are always losses to take into account. The mutual inductance is then modified as:

$$M = k\sqrt{L_P L_S} \tag{5.12}$$

in which $0 \leq k \leq 1$ is the coupling factor of the real transformer. A direct effect of the presence of k is the appearance of a leaking inductance L_{P/S_L}. Then, the sum of L_{P/S_L} and $L'_{P/S}$ should be equal to the self inductance of the coil. Thus, starting from the mutual inductance:

$$M = \sqrt{L'_P L'_S} = k\sqrt{L_P L_S} \rightarrow \begin{cases} L'_P = kL_P \\ L'_S = kL_S \end{cases} \tag{5.13}$$

and, therefore, the leaking inductance can be found as:

$$\begin{cases} L_{P_L} = L_P(1-k) \\ L_{S_L} = L_S(1-k) \end{cases} \tag{5.14}$$

The windings used to create the coil have an intrinsic resistance, being a wire of finite length and area. Such resistance, namely called $R_{P/S}$, has to be then added in series to the coils in the model. The contact between the coils and the transformer's core will give rise to a parasitic

capacitance. Such capacitance accounts also for the equivalent one arising from the turns of the same coil. However, not so much the leaking inductance but the capacitance, is quite difficult to estimate. For this reason, it is preferred an equivalent RLC model. In Figure 5.3 is shown the bespoke model. Since the coupling factor k is usually very close to one, the leakage inductance are omitted from the model once it is implemented. The characterization of the parasitic components was however carried out by experimental analysis performed with the help of some instruments (different kinds of LCR meters).

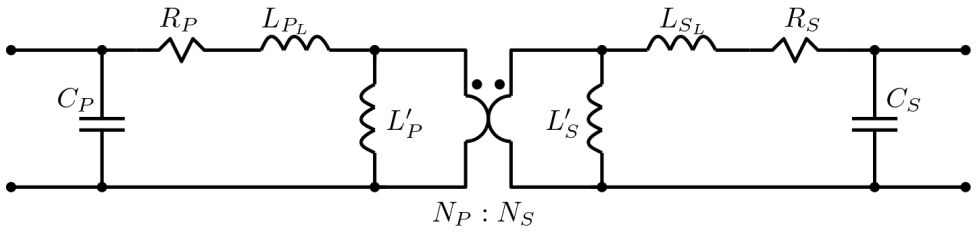

Figure 5.3: Circuital model of the transformer.

5.1.3 Core saturation

The core of the transformer is made up by a material that is sensible to the magnetic filed, that is, a ferromagnetic material. A typical relation between the magnetic flux density (B) and the magnetizing field (H) is described by the characteristic of Figure 5.4. Considering now a material

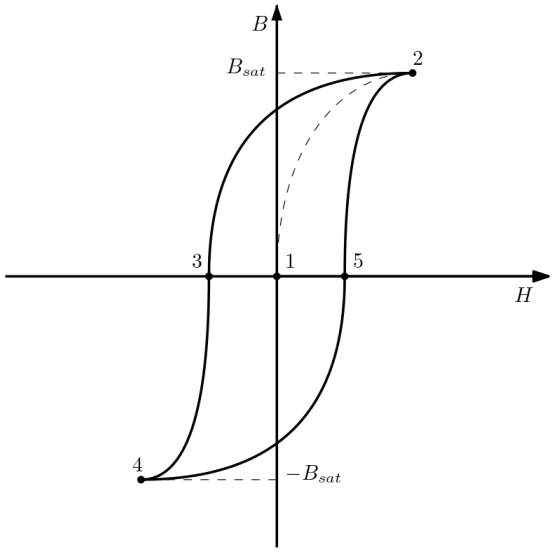

Figure 5.4: Ferromagnetic material characteristic: B as a function of H.

that is not yet magnetized, that is starting at the point $(0, 0)$ of the plot of the above Figure, and increasing the magnetizing current H, the characteristic is described by the section $1 - 2$ of the curve. If H keep increasing, then B reaches a point at which increases only with slope mu0 as a function of H. This point is called saturation point and is marked with the number 2. Then, if H decreases, the path that B follows is $2 - 3 - 4$. Again, 4 is considered a saturation point. If H starts increasing again, it reaches the saturation point 2 through the $4 - 5 - 2$ path. To be noted is that the characteristic do not pass through point 1 again. This behavior is called hysteresis.

B_{sat} yelds an important information about the maximum current the transformer can sustain before reaching the saturation point. It is advisable then to maintain the current below such

value. Taking into account Equation 5.5 and Equation 5.7, B can be found as:

$$\dot{B} = -\frac{emf(t)}{NA_e} = \frac{\mu N}{l}\dot{I} \tag{5.15}$$

and, by recalling:

$$\dot{B} = \frac{dB}{dt} \tag{5.16}$$

Equation 5.15 can be rewritten so as to find B:

$$\begin{gathered} \int \frac{dB}{dt}dt = \int dB = \frac{\mu N}{l}\int \frac{dI}{dt}dt = \int dI \\ \rightarrow B = \frac{\mu N}{l}I \end{gathered} \tag{5.17}$$

Usually, in the datasheet of a transformer (or of the magnetic core) is not reported directly l, but is reported instead A_L:

$$A_L = \mu\frac{A_e}{l} \rightarrow l = \mu\frac{A_e}{A_L} \tag{5.18}$$

and now, by combining Equation 5.17 and Equation 5.18, the relation between B and I can be written as:

$$B = \frac{NA_L}{A_e}I \tag{5.19}$$

The saturation current can now be found as:

$$I_{sat} = B_{sat}\frac{A_e}{NA_L} \tag{5.20}$$

From the data acquired by the datasheet of the particular transformer chosen, it was found:

$$\begin{cases} I_{sat-p} = 3.71A \\ I_{sat-s} = 0.53A \end{cases} \tag{5.21}$$

Taking as a reference the maximum ratings of the biasing power supply, that are $-100V$ and $100mA$ when the probe is in ion saturation region and $30V$ and $300mA$ when the probe is in electron saturation region, it can be said that the transformer won't reach magnetic saturation. The transformer operates well below its limits.

5.1.4 Coupling factor derivation

In order to derive the coupling factor k, a mathematical approach can be adopted. By looking at the model of Equation 5.10 it can bee seen that, if one of the two voltages is shorted, for instance the one at the secondary, the primary voltage is a function of the derivative of the currents:

$$\begin{cases} V_P(t) = L_P\dot{I_P} + M\dot{I_S} \\ 0 = M\dot{I_P} + L_S\dot{I_S} \end{cases} \tag{5.22}$$

from which it easy to find the expression defining the voltage at the primary side $V_P(t)$:

$$V_P(t) = \dot{I_P}\left(L_P - \frac{M^2}{L_S}\right) = \dot{I_P}L_{eq-p} \tag{5.23}$$

in which L_{eq-p} is the equivalent inductance measured at the primary when the secondary is shorted. Accounting for the latter equality, one can write:

$$M^2 = (L_P - L_{eq-p})L_S = k^2 L_P L_S \tag{5.24}$$

form which k is easily found as:

$$k = +\sqrt{1 - \frac{L_{eq-p}}{L_P}} \tag{5.25}$$

However, also by shorting the primary side and doing the math all over again the value of k can be found, which expression is then:

$$k = +\sqrt{1 - \frac{L_{eq-s}}{L_S}} \tag{5.26}$$

in which L_{eq-s} is the equivalent inductance measured at the secondary when the primary is shorted.

5.2 Transformer characterization

In order to have a usable and working model of the transformer, it is necessary to derive the needed parameters from the physical transformer. This section takes care of this problematic and exposes a general procedure to characterize a transformer. The main parameters of the latter are $L_P = 14.56\mu H$ and $N_P = 4$ for the primary and $L_S = 1.05mH$ and $N_S = 34$ for the secondary. However, the data measured may differ from the one reported in the datasheet due to mismatches in the fabrication specification and the given constraints. The transformer employed, however, features a different configuration from the model of Figure 5.2. A better model is that of Figure 5.1, in which there are two windings for each side of the transformer. The characterization thus proceeds to create three models: one for each primary-secondary (p-s) coil couple and one for the case in which the coils at each side are connected in a series configuration.

5.2.1 Parameters extrapolation

To proceed with the transformer's characterization, that is the first step then to create the circuital model described in Figure 5.3, it is needed of the coupling factor k. The methodology applied is that of Equation 5.25. For this analysis, k is assumed to be invariant with the frequency, even though slight changes can be observed. The switching frequency was also assumed to be $f_s = 500kHz$. From a measurement performed with the LCR meter:

$$\begin{cases} L_{P1} = 17.5\mu H \\ L_{eq_P} = 0.276\mu H \end{cases} \rightarrow k = 0.992 \tag{5.27}$$

The characterization of the parasitic capacitance and of the parasitic resistance are made by means of an impedance / gain-phase analyzer (HP-4194 A). By performing a frequency sweep and then fitting the parameters with a RLC network, the data sought can be extrapolated. In Table 5.1 are reported the data relative to the primary and secondary side of the transformer.

	L_{Px} $[\mu H]$	R_{Px} $[\Omega]$	C_{Px} $[nF]$	L_{Sx} $[\mu H]$	R_{Sx} $[\Omega]$	C_{Sx} $[pF]$
$x = 1$	17.13	1.64	1.57	793	61	34.18
$x = 2$	17.15	1.4	1.58	794	60.1	34.25

Table 5.1: Equivalent parameters of the transformer circuital model. x refers to the coil number.

Figures 5.5a and 5.5b show the set up of the instrumentation to perform the measurements. The transformer was locked into a rigid support in order to not damage it and with the extent to isolate it from the surrounding, and thus to not affect the measure. Figure 5.5c reports the measured characteristic alongside with the equivalent ones derived from the equivalent circuit of Figure 5.5d. It is highlighted a peak of resonance at a frequency f_{rpx} in which the impedance

assumes high values compared to those at the working frequency. A similar effect happens at the secondary coil (as highlighted in Figure 5.5e), in which there is a resonance peak at the frequencies f_{rsx}.

$$\begin{cases} f_{rp1} = \frac{1}{2\pi\sqrt{L_{P1}C_{P1}}} \simeq 970kHz \\ f_{rp2} = \frac{1}{2\pi\sqrt{L_{P2}C_{P2}}} \simeq 966kHz \end{cases} \quad \begin{cases} f_{rs1} = \frac{1}{2\pi\sqrt{L_{S1}C_{S1}}} \simeq 967kHz \\ f_{rs2} = \frac{1}{2\pi\sqrt{L_{S2}C_{S2}}} \simeq 965kHz \end{cases} \tag{5.28}$$

The values are quite close to those found during the measurement. An advisable procedure is to double check the results obtained with a second measurement. This was done by means of the HIOKI-3536 LCR meter, via which a frequency sweep was performed, the data collected and then plotted. The data obtained from the instrument shows a resonant frequency that

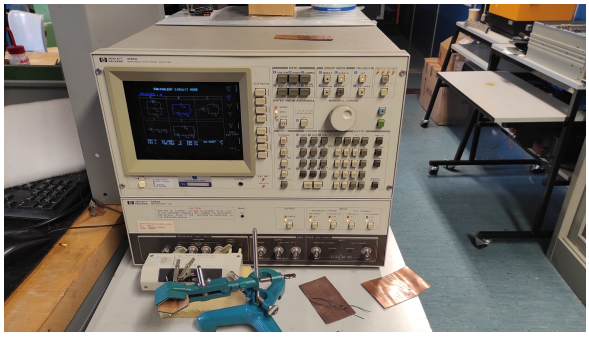

(a) Instrumentation set up: instrument overall view.

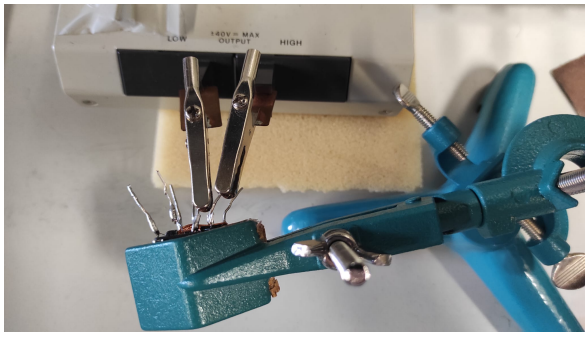

(b) Instrumentation set up: transformer connection.

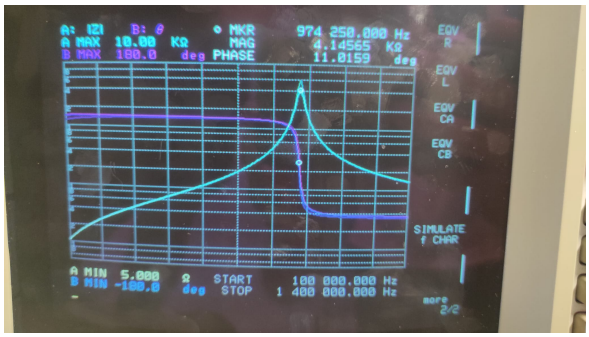

(c) Characteristic seen from the primary side of the transformer.

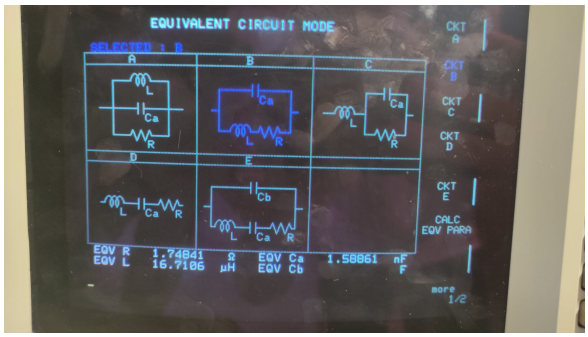

(d) Equivalent circuit with relative parameters of the primary side of the transformer.

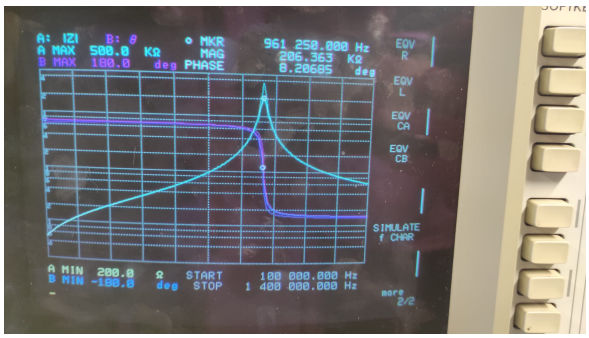

(e) Characteristic seen from the secondary side of the transformer.

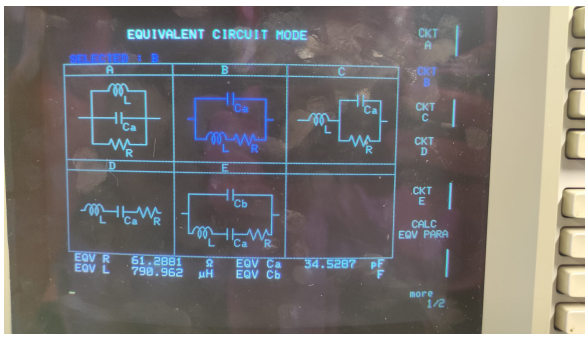

(f) Equivalent circuit with relative parameters of the primary side of the transformer.

Figure 5.5: Instrumentation set up, equivalent circuits and characteristics of the transformer.

is around $890kHz$ (see Figure 5.6). This mismatch can be found in the different instruments used and in the fact that the two measurements were carried out in two different time periods.

However, despite the small discrepancies, the plots are in agreement with the results previously obtained. In the above figures, the resonance frequencies and the impedance are $f_{rp} = 974kHz$ and $Z_P = 4.15k\Omega$ for the primary and $f_{rs} = 961kHz$ and $Z_S = 206k\Omega$ for the secondary.

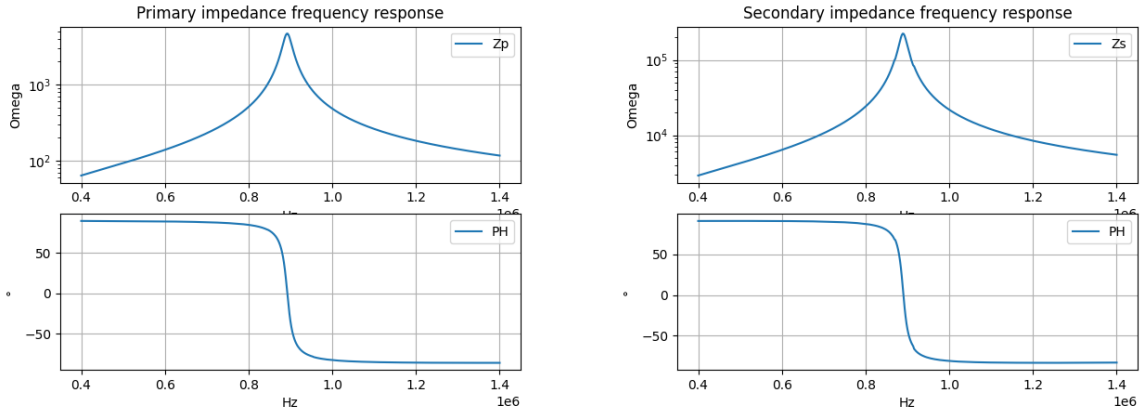

Figure 5.6: Characterization of the transformer's impedance of only one p-s coil couple.

The second characterization was aimed to measure the equivalent parameters of both the primary and secondary side when the two coils of each side are connected in a series configuration, that is, when L_{P1} is in series with L_{P2} and L_{S1} is in series with L_{S2} The data acquired is reported in Table 5.2. and the resonance frequencies found are:

L_P $[\mu H]$	R_P $[\Omega]$	C_P $[pF]$	L_S $[mH]$	R_S $[\Omega]$	C_S $[pF]$
69.55	4.98	402	3.233	136.8	29.2

Table 5.2: Equivalent parameters of the transformer circuital model.

$$\begin{cases} f_{rp} = 952kHz \\ f_{rs} = 518kHz \end{cases} \tag{5.29}$$

It is curious to note that the two frequencies are not coincident as happened with the previous analysis. The reason might be found in the stress placed in transformer pins (specially those at the secondary coils), therefore damaging them and thus invalidating the measure.

5.2.2 Equivalent model

With the data collected so far it is possible to built the spice model of the transformer and run some test in order to align it with the reality so as to have a close-to-reality model to use in future simulations. In figure 5.7 are shown the two implementation of the transformer model used to derive the plots of Figure 5.8. Figure 5.8 shows the characteristic of the impedance as a function of the frequency. Nevertheless, it has to be reminded that the model adopted is an equivalent model, thus some parameters hardly have a correspondence with the reality.

The last simulation gave results not coincident with what it was found during the measurement on the real transformer. This characterization was performed to find out the equivalent components of the transformer when the two windings at the primary and secondary side are placed in a series configuration. However, the data collected suggest the equivalent model resulting from the merging of the two half models found earlier (see Figure 5.9) is not equal to the one measured. Simulation results point out that the resonance frequency, with the configuration adopted in Figure 5.9, is around $690kHz$ which is in contradiction with what reported by the

measurements carried out. The reason is that the model created so far takes into account only partially the coupling effects between the two sides. A proper procedure is, with the experience

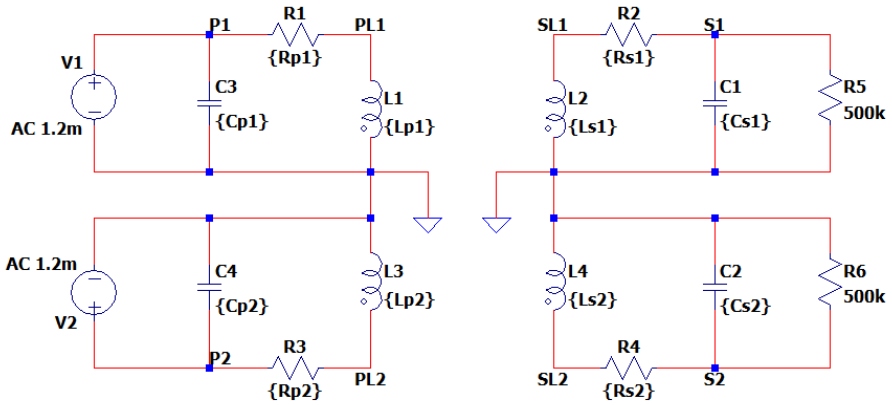

(a) Primary coil characterization circuit.

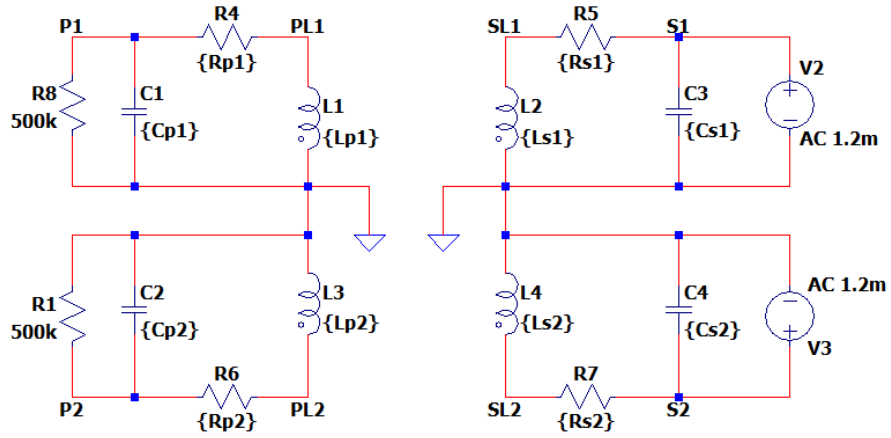

(b) Secondary coil characterization circuit.

Figure 5.7: Circuital models implemented. The two middle terminals are connected to ground in order to isolate the two windings.

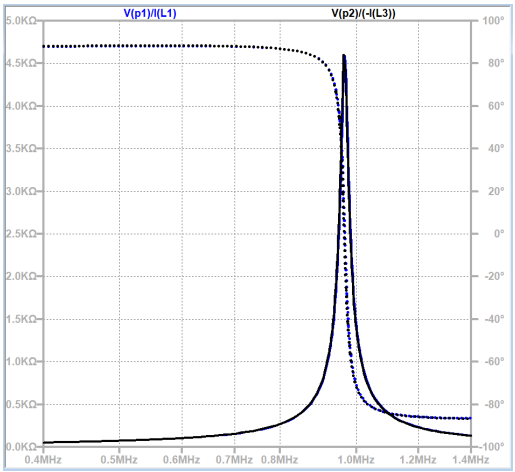

(a) Primary coil characteristic.

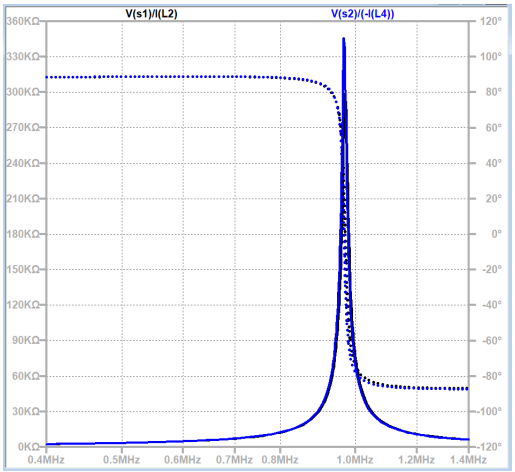

(b) Secondary coil characteristic.

Figure 5.8: Characterization of the transformer's impedance via simulation.

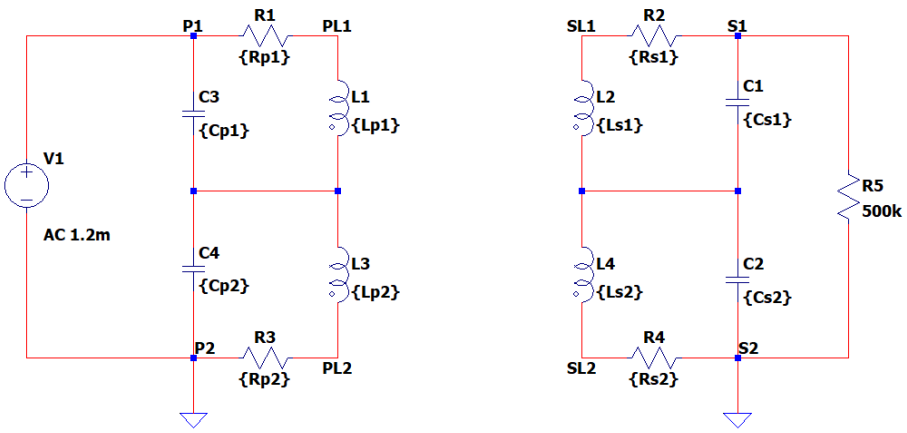

(a) Primary coil characterization circuit.

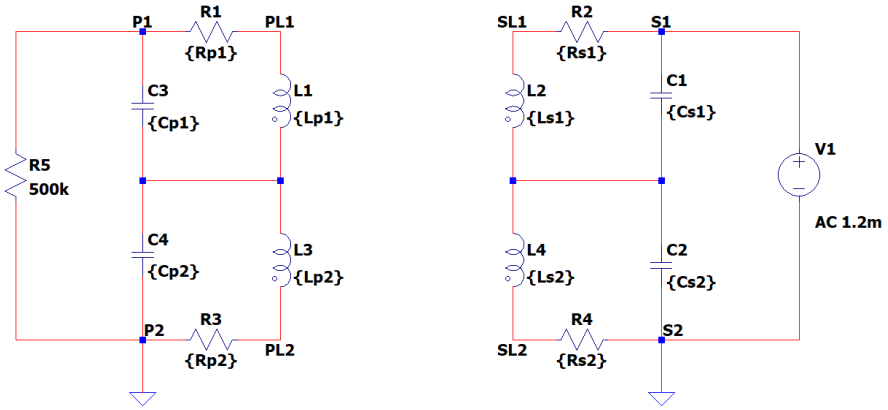

(b) Secondary coil characterization circuit.

Figure 5.9: Circuital models implemented. The two coils of the primary and secondary side are placed in series.

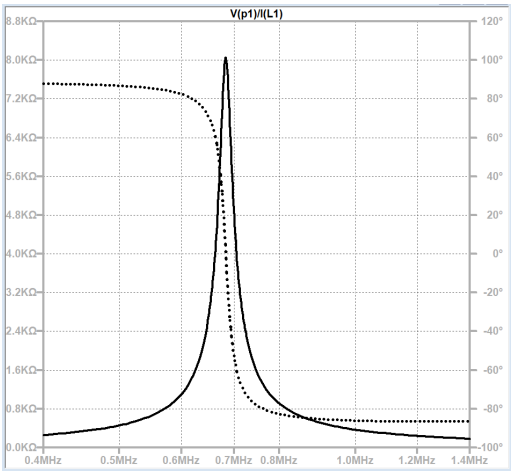

(a) Primary coil characteristic.

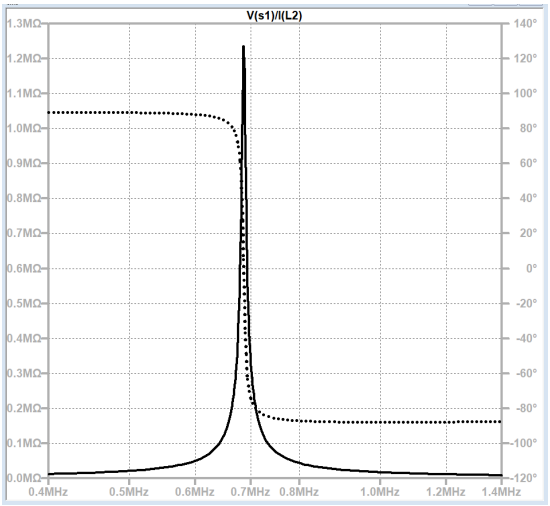

(b) Secondary coil characteristic.

Figure 5.10: Characterization of the transformer's impedance via simulation.

collected with this analysis, to carry out a thorough analysis of the transformer, with the aim have a better characterization of the coupling effect ao as create a close-to-reality model (without incurring in inconveniences such as broken pins, etc...).

5.3 Biasing power supply simulation

Once the model of the two halves of the transformer are completely characterized, it is possible to implement via LTSpice the complete circuit and verify its behavior. Not being able, however, to characterize all the possible working aspect of the circuit, some estimates were necessary. In this specific case, not having characterized the impedance of the probe, a load resistance of $R_L = 3.5k\Omega$ was placed in order for the circuit to work in quasi real-life condition. The aim of this section is to analyze and verify the circuit behavior and to isolate possible criticism in the future implementation of the latter.

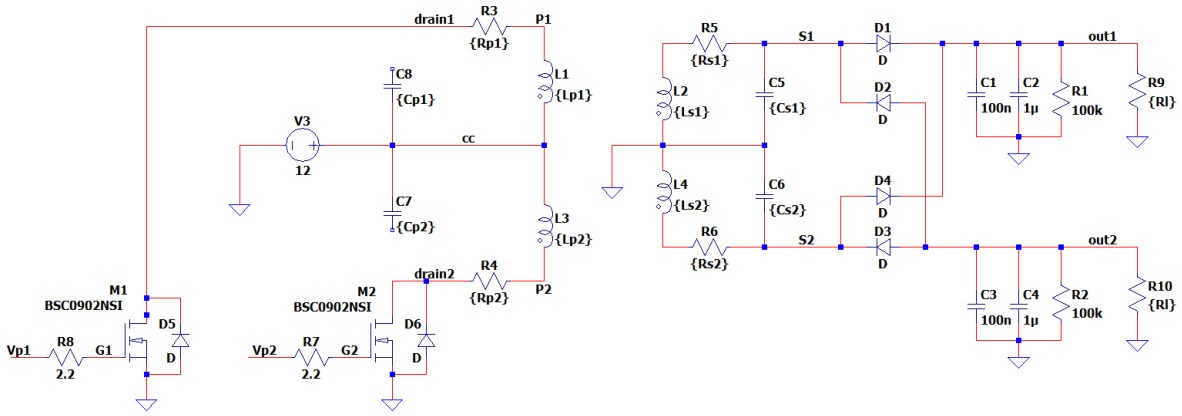

Figure 5.11: Circuital model of the biasing power supply.

5.3.1 Circuit analysis

Within this first set of simulations, the MOSFETs' switching frequency is set to $f_{sw} = 500kHz$ while the duty cycle is set to $D = 50\%$.

A first, quick and useful look can be given to the MOSFETs behavior. In figure 5.12 are shown the classical waveform that can be expected when looking at MOSFETs used as switches. V_{p1} and V_{p2} are the driving voltages and their amplitude was chosen accordingly with the employed FPGA specification and the driving circuit used. V_{g1} and V_{g2} are instead the MOSFETS' gate voltages. As expected, the characteristic waveforms highlight the Miller's plateau effect both when the driving voltage is rising up to its working value and when is going down to its steady value. Thi latter voltages, as far plots of Figure 5.12 are concerned, are perfectly overlapped (Without having a smaller time-span they cannot be distinguished, but they are not the focus of this simulations). In the latter part, there is also a small ringing effect due to the parasitic components of the MOSFET. Also, the switches are driven with opposite phases.

More interesting waveforms are obtained if one looks at the voltage across the windings of the primary side of the transformer, being also shown in Figure 5.12 (respectively called $V(drain1, cc)$ and $V(drain2, cc)$). Both current and voltage exhibit a ringing behavior during the transistor turn-off. A better idea of the impact of this overshoot is shown by looking at the drain' voltage. The first overshoot in the voltage waveform reaches approximately $34V$, therefore the transistor must be chosen so as to withstand such stress without damaging it. The resonance frequency, in any case, is not the one highlighted for the transformer: even though the inductance is the same, the parasitic capacitance is different due to the presence of the transistors. This latter element can be estimated, having measured the frequency $f_{res} = 18MHz$ from the plot of Figure 5.12, as:

$$\begin{aligned} C_{par-eq} &= \frac{1}{L_{P1}(2\pi f_{res})^2} = \frac{1}{L_{P2}(2\pi f_{res})^2} \\ &\simeq 4.56pF \end{aligned} \tag{5.30}$$

Depending on the presence of a load, ringing effects can be found also at the secondary side of the transformer.

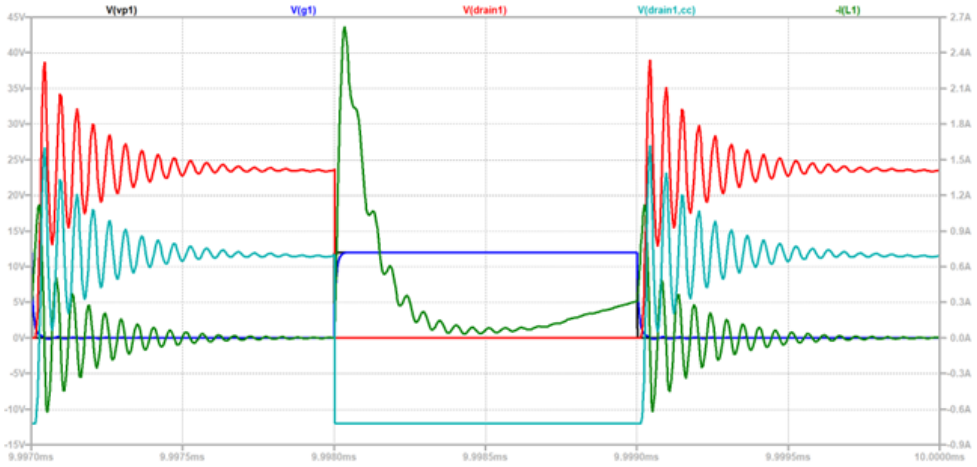

(a) Channel 1 characteristic waveforms.

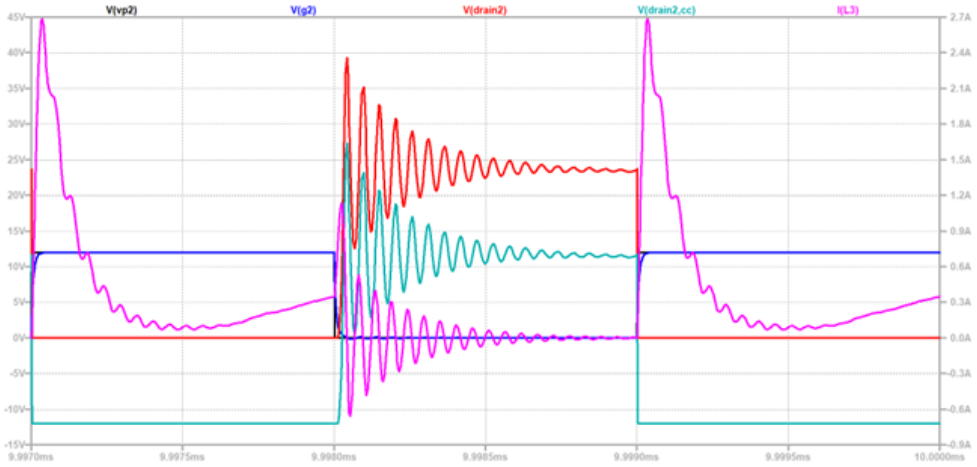

(b) Channel 2 characteristic waveforms.

Figure 5.12: Characteristic waveforms of the transistors and of the transformer's coils.

The waveforms of the transformer secondary side (see Figures 5.13a) are quite similar to those found at the primary side. In this case the waveform is smoothed with respect to the primary side due to the presence of a non-zero output current, that is, due to the presence of a load. Nevertheless, by cutting the connection between the coil and the rectifying bridge, voltage peaks that can be dangerous for the circuit itself and for the surrounding electronic. Simulations results highlighted peaks up to $200V$ against a nominal voltage of $80V$, as shown in figure 5.13b.

The last set of simulations was aimed to verify the output voltage behavior, the settling time from a start-up of the system and its general characteristic. Figure 5.14a shows how the output voltage behave when the system is turned on. The settling time in this case is about $2mS$. Figure 5.14b shows instead the response of the output voltage to various loads, marking different behaviors. The load resistance was set to vary between 100Ω to $100k\Omega$, to cover all possible cases. The minimum settling time measured is $0.5mS$, in the case of $R_L = 100\Omega$, while the maximum amount cannot is more than ten times its minimum values (this is the case with $R_L = 100k\Omega$). Another important parameter to estimate is the output voltage ripple, which can rise some problems when talking about the overall system's accuracy. As shown in Figure 5.15, the ripple of the positive high voltage branch is in opposition of phase with respect to the the one of the negative high voltage branch, as expected from the driving method of the transistors.

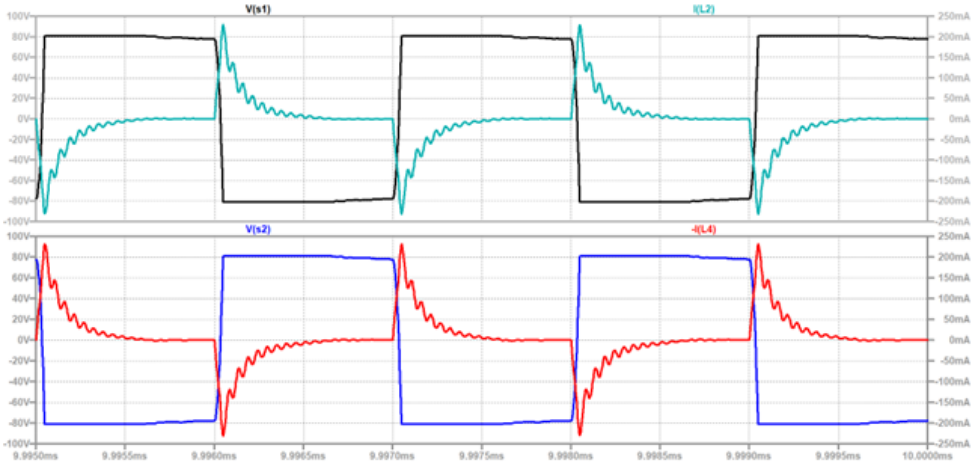

(a) Expected current and voltage waveforms across the secondary winding of the transformer.

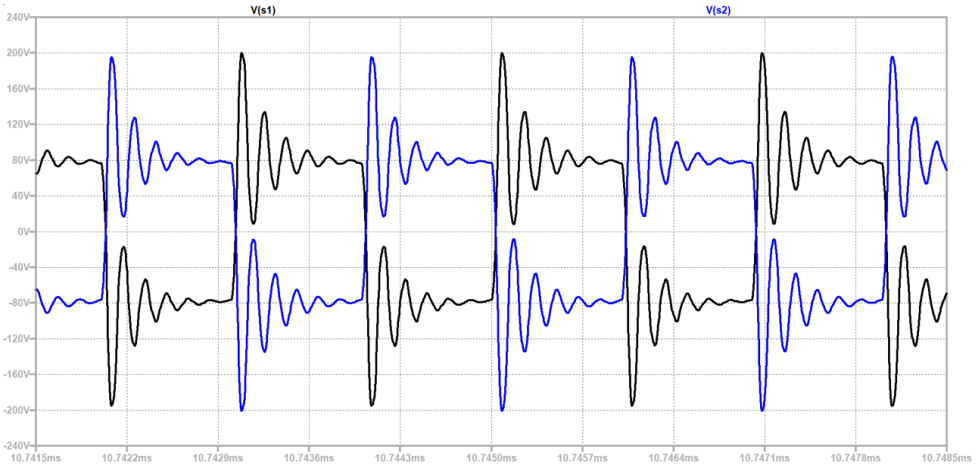

(b) Voltage peaks at infinite load operations.

Figure 5.13: Characteristic waveforms of the transformer secondary side under different working condition: infinite load and $R_L = 3.5k\Omega$.

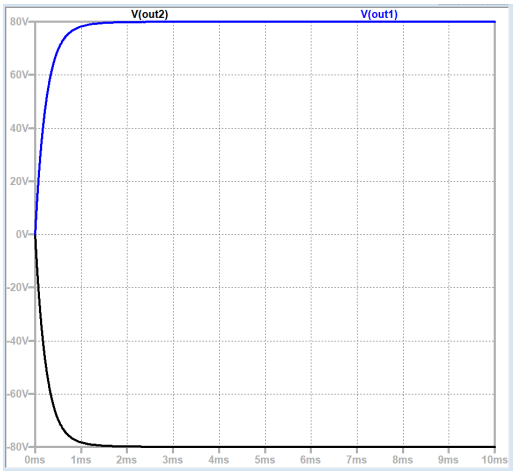

(a) Dual Output voltage characteristic with a load $R_L = 3.5k\Omega$.

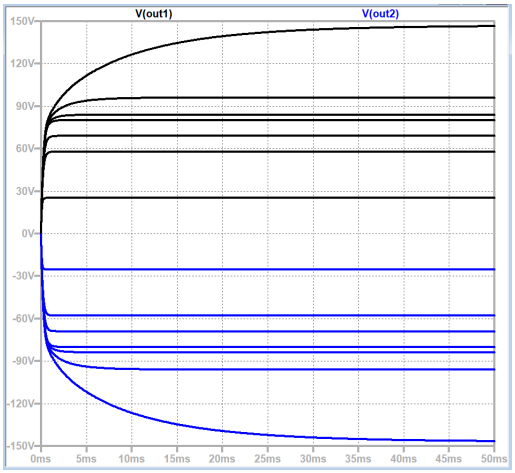

(b) Dual Output voltage characteristic with different loads.

Figure 5.14: Expected settling times of the output voltage.

The ripple frequency is estimated to be twice the switching frequency, that is $f_{ripple} = 1MHz$, while the ripple magnitude is $\Delta_{V-ripple} = 13mV$. Significant changes in this latter quantity were measured with a change of duty-cycle or a combination of $R_L\&D$, highlighting ripples up to $\Delta_{V-ripple} \simeq 70mV$. A feasible solution, in order to suppress the output ripple, is to place a

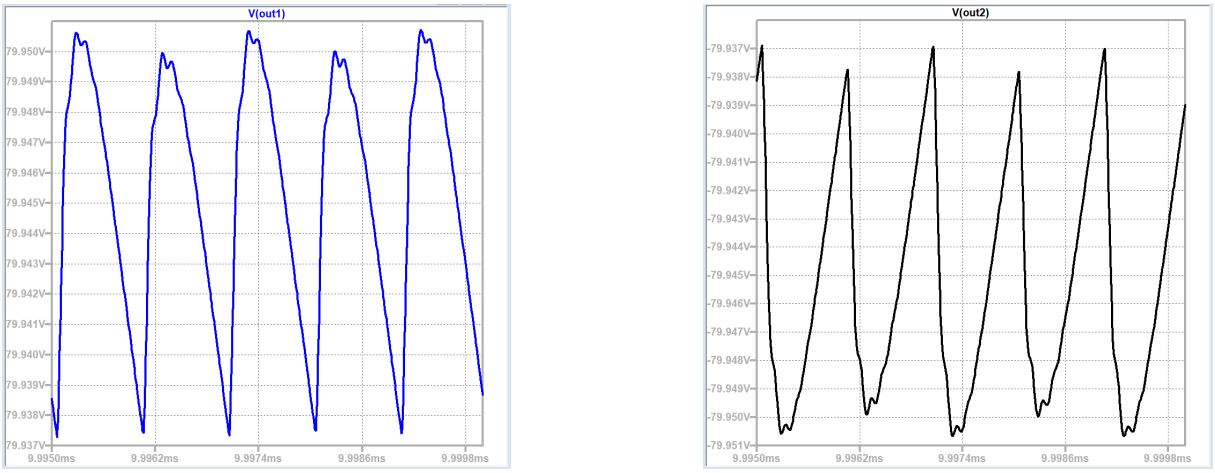

(a) Voltage ripple at the positive branch.

(b) Voltage ripple at the negative branch.

Figure 5.15: Voltage ripple at the high voltage outputs.

low-pass non-dissipative LC filter with a cut-off frequency f_{lc} significantly lower than that of the ripple frequency. By setting the $f_{lc} = 50kHz$, the relation between the L and C is given by:

$$L_f = \frac{1}{C_f(2\pi f_{lc})^2} \tag{5.31}$$

C_f $[nF]$	L_f $[mH]$
100	0.1
1000	0.01

Table 5.3: Proposed values for the LC low-pass filter with $f_{lc} = 50kHz$.

With this implementation (see Figure 5.16), the ripple is reduced to $\Delta_{V-ripple} = 350uV$. Anyway, any change in duty cycle D or in the load R_L (that results on a change in the output current) will result in a change in the ripple. There are two things to be kept in mind when analyzing

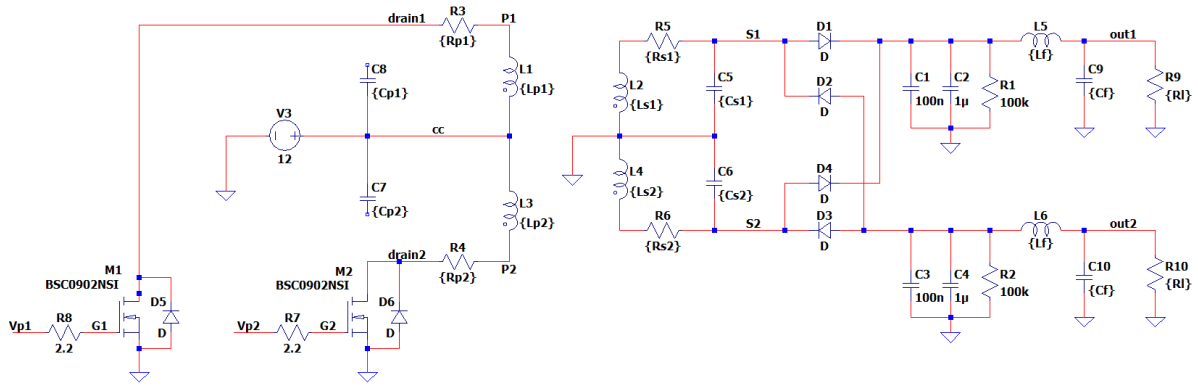

Figure 5.16: Circuital model of the biasing power supply with the filter applied.

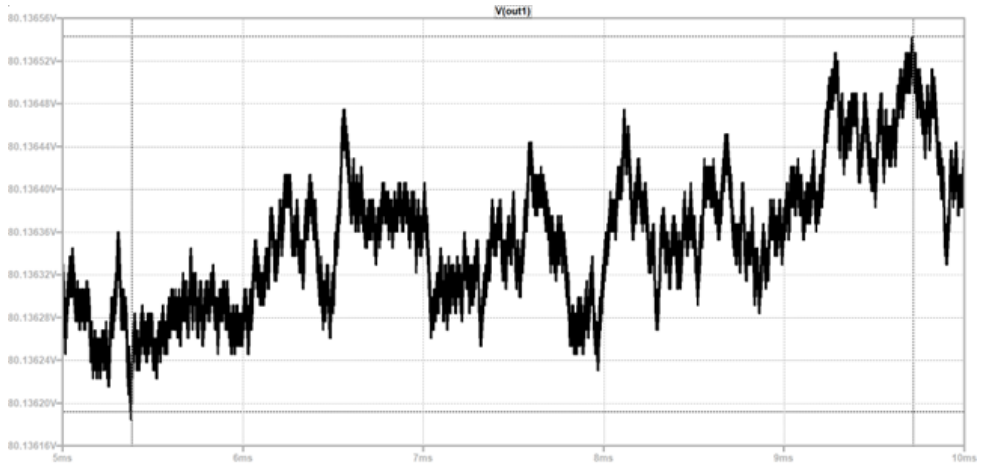

Figure 5.17: Ripple voltage with the filter applied.

and trying to understand the plots produced so far: 1) the circuit is behaving in a open-loop configuration when it is instead supposed to work with a feedback, that is, to regulate the PWM accordingly to the desired output and 2) the load attached is a "fake" load since the probe's impedance is everything but constant and doesn't act linearly. A better and more complete characterization can be done once the prototype is ready, so as to have a real-life circuit to work with.

5.3.2 PWM modulation & voltage sweep

In order to sweep the voltage within the specified range, a PWM modulation technique is adopted. The switches $M1$ and $M2$ are driven by PWM signal that modifies, accordingly to what the user needs, the mean values the filter extrapolates. Even though the PWM modulation is performed through software by the FPGA, an analog equivalent is needed in order to perform the sweep in the simulation. To that extent, the circuit of Figure 5.18 was added to replace the square-wave generator previously used. To avoid the two transistors to work simultaneously, the duty cycle

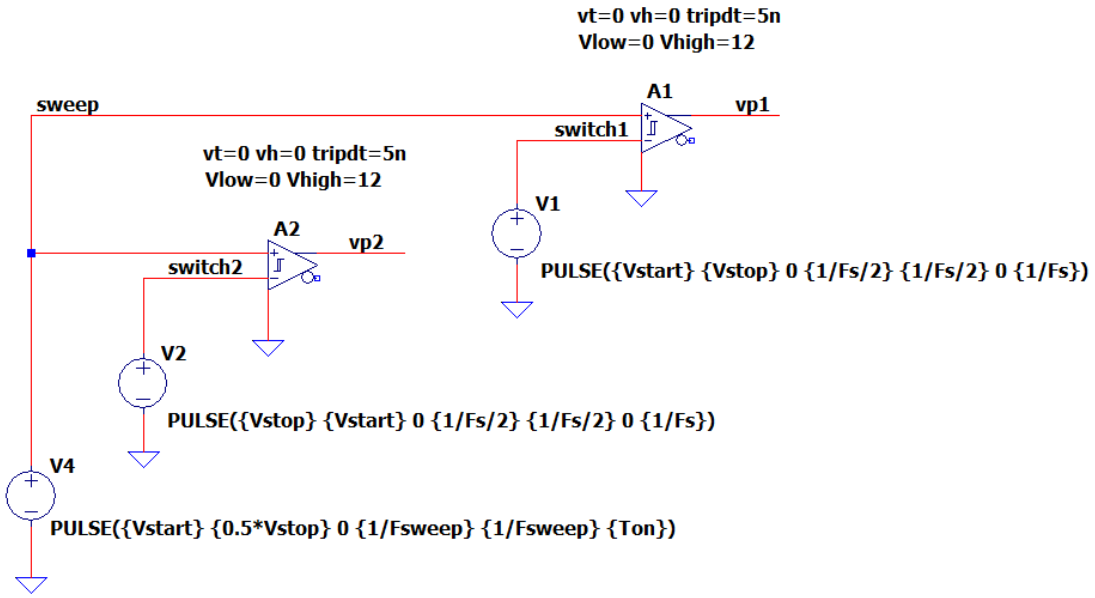

Figure 5.18: Analog PWM generation circuit.

was set to reach a maximum value of 50%, hence the $\frac{1}{2}Vstop$ at the sweep generator ($V4$ in Figure 5.18). If this condition is not met and the two transistor overlap their working time period, both the primary windings will be magnetized, hence creating a short period in which there will be a current spike, both at the primary and the secondary, that will increment the output voltage to a value not well defined, that may affect negatively the measure as well as damage the electronic. In Figure 5.19 are shown the sweep waveform used to test the circuit and the respective PWM modulation in which it can be clearly seen that the duty cycle does not rise up above 50%. In this simulation, the switching frequency was set to $1kHz$ with the intent to allow the human eye to appreciate the entire time interval. The modulating voltage, as

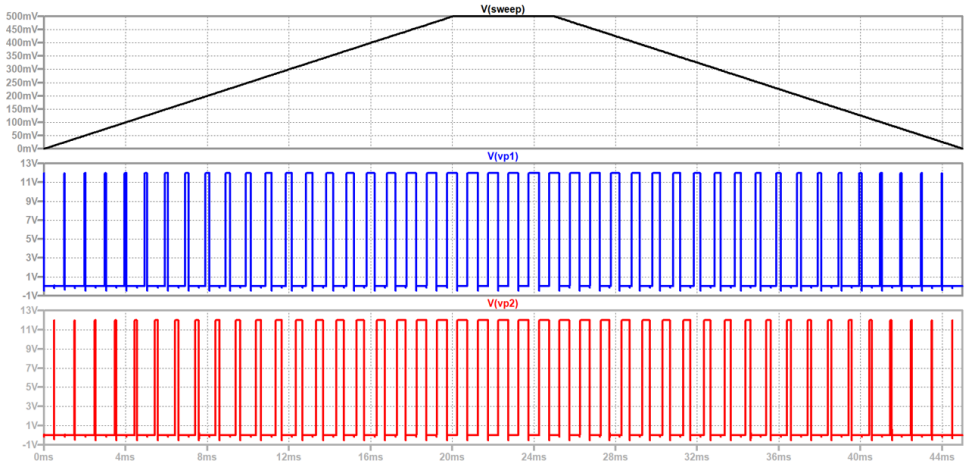

Figure 5.19: PWM generation according to the modulating signal.

explained earlier, reaches only half of its values, in order to allow for the PWM to not get above 50%. In the following simulation results, the load impedance was kept constant, due to the lack of a component modeling the probe's impedance. Due to this limitation, the circuit behaves in a different way and the results have to be red keeping in mind this important condition. Moreover, due to the perfect symmetry of the circuit, only the positive half is exposed, but the same results and conclusions can be obtained by looking at the second half of the circuit.

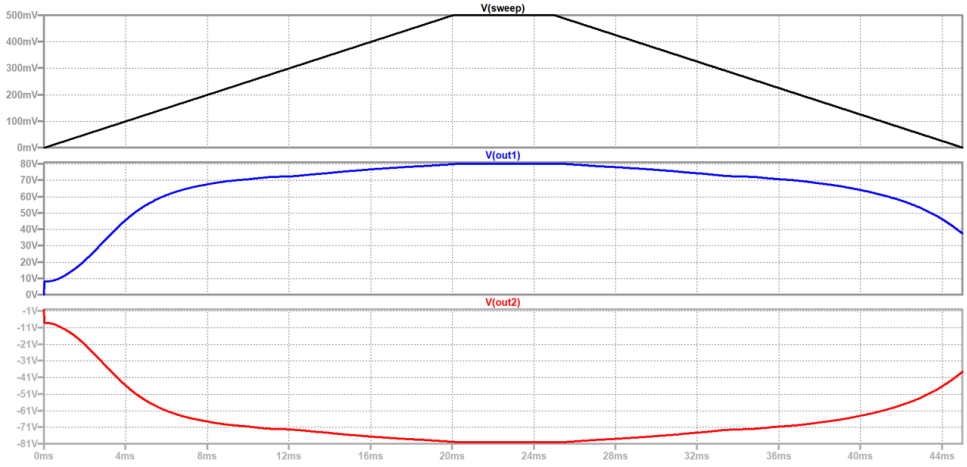

Figure 5.20: Output characteristic obtained when performing a PWM sweep ($V(out1)$ and $V(out2)$ are that of Figure 5.16)).

Figure 5.20 exposes how the circuit behaves when a DC sweep is performed. Except for the first transitory amount of time, even at the end of the sweep period, the output voltage never reaches $0V$. This is due to both the working conditions of the simulation circuit, that aren't the same of

the real circuit that will be implemented, and the current drawn from the output channel that is not enough to discharge all the energy accumulated during the operation of the system. This situation is quite problematic specially when the current generated form the probe, and therefore required by the power supply, is of small magnitude (for example when we the probe is in the ion saturation region or when a double probe measurement is required). There are some feasible solutions to solve the problem, each one with its pros and cons.

- Double stage power supply: A first possible solution is to place a second DC-DC converter in series to the already existent one in order to increase the range of the output voltage. Even though it may seem the most reliable and easy solution to implement, it will ask for greater PCB space and cost, as well as increasing significantly the complexity of the circuit.

- Bleeding resistor: More easy solution is to place a bleeding resistor that will be activated, by means of a switch when small current and voltages are required by the probe. It is important to remind that the insertion of a bleeding resistance in parallel to the probe will not affect the measure in by any means since the probe behave like a voltage controlled current source, and therefore imposes its own current. However, the bleeding resistor has to be sized so as to not require a current such to saturate the transformer's core. In Figure

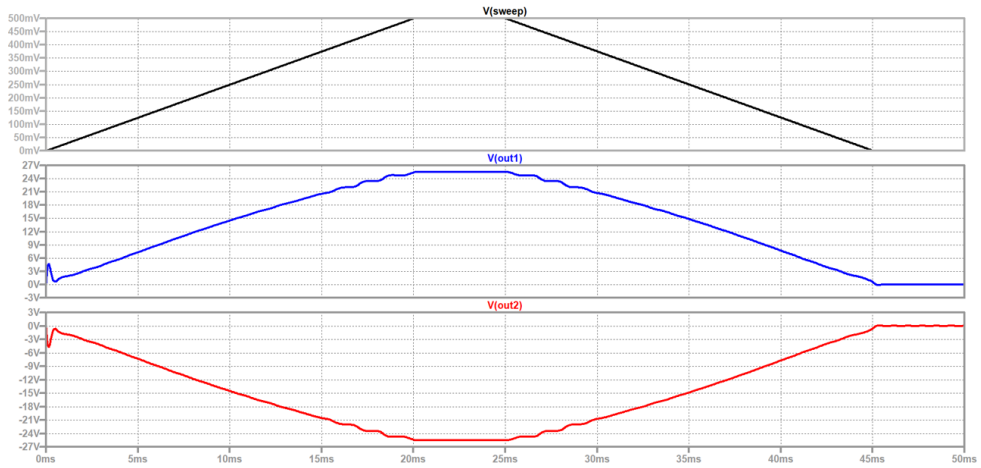

(a) Output characteristic obtained when performing a PWM sweep with a bleeding resistor of 100Ω.

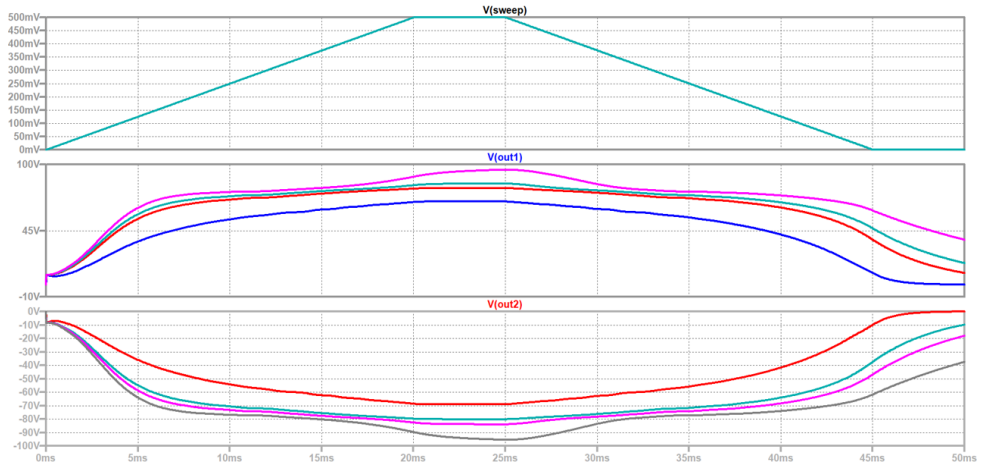

(b) Output characteristics obtained when performing a parametric simulation varying the bleeding resistor.

Figure 5.21: Output characteristic.

5.21a is reported how the output voltage behaves when a bleeding resistor of 100Ω is placed, while in Figure 5.21b are reported various plots obtained from a parametric simulation in which the bleeding resistance was set to different values: $1k\Omega, 3.5k\Omega, 5k\Omega, 10k\Omega$ (Increasing the value of the load resistor increases also the output value and the settling time). The presence of a low-value resistance helps with the reaching of a $0V$-output signal. In spite of having a simpler circuit, the control algorithm will be more complex than the one needed with the previous solution. It has to be reminded that the waveforms in here are taken in a open loop configuration and therefore they may not fully coincide with what can be found in a feedback configuration.

- Power supply turn-off: This solution doesn't require any components additions. It simply consist in keeping the power supply in its off-state for a long enough amount of time so as to reach $0V$, or a value close enough. In Figure 5.22 is proposed an alternative modulating signal, via which the output voltage reaches values as closed to zero as $1mV$. In any case,

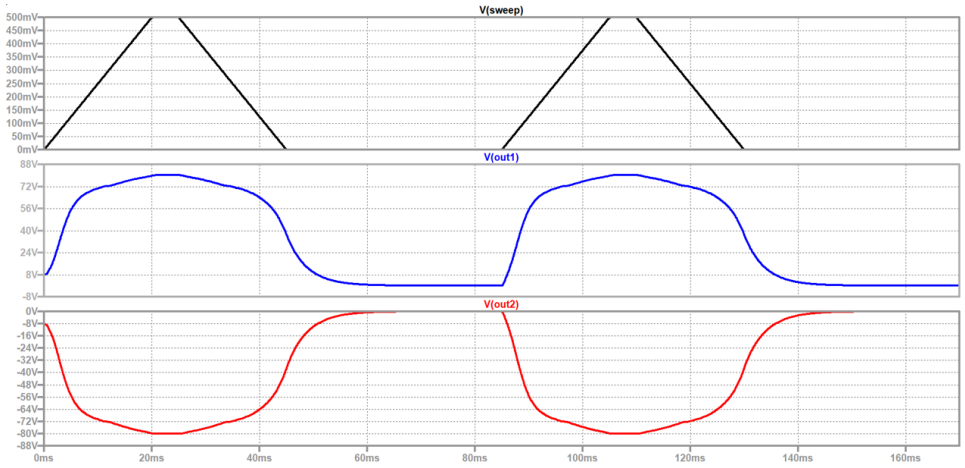

Figure 5.22: Output characteristic obtained when performing a PWM sweep with a final off-state.

the modulating signal can be modified as the user needs, providing that the off-state is long enough for the power supply to reach a close-to-zero value satisfying enough.

Nevertheless, nothing takes away the possibility of using a combination of the solutions proposed above. In the following are reported some useful waveforms attained at different PWM values.

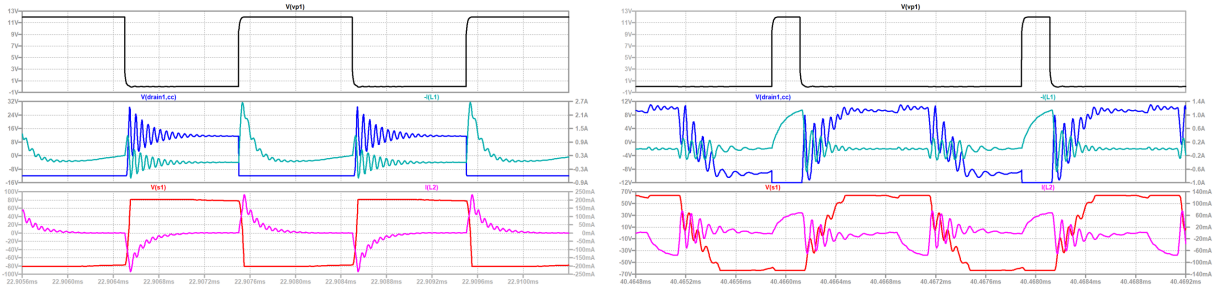

(a) Useful waveforms with $D = 0.5$.

(b) Useful waveforms with $D \sim 0.2$.

Figure 5.23: Characteristic waveforms of the transistors with two different duty cycle values.

5.4 Circuit Schematics

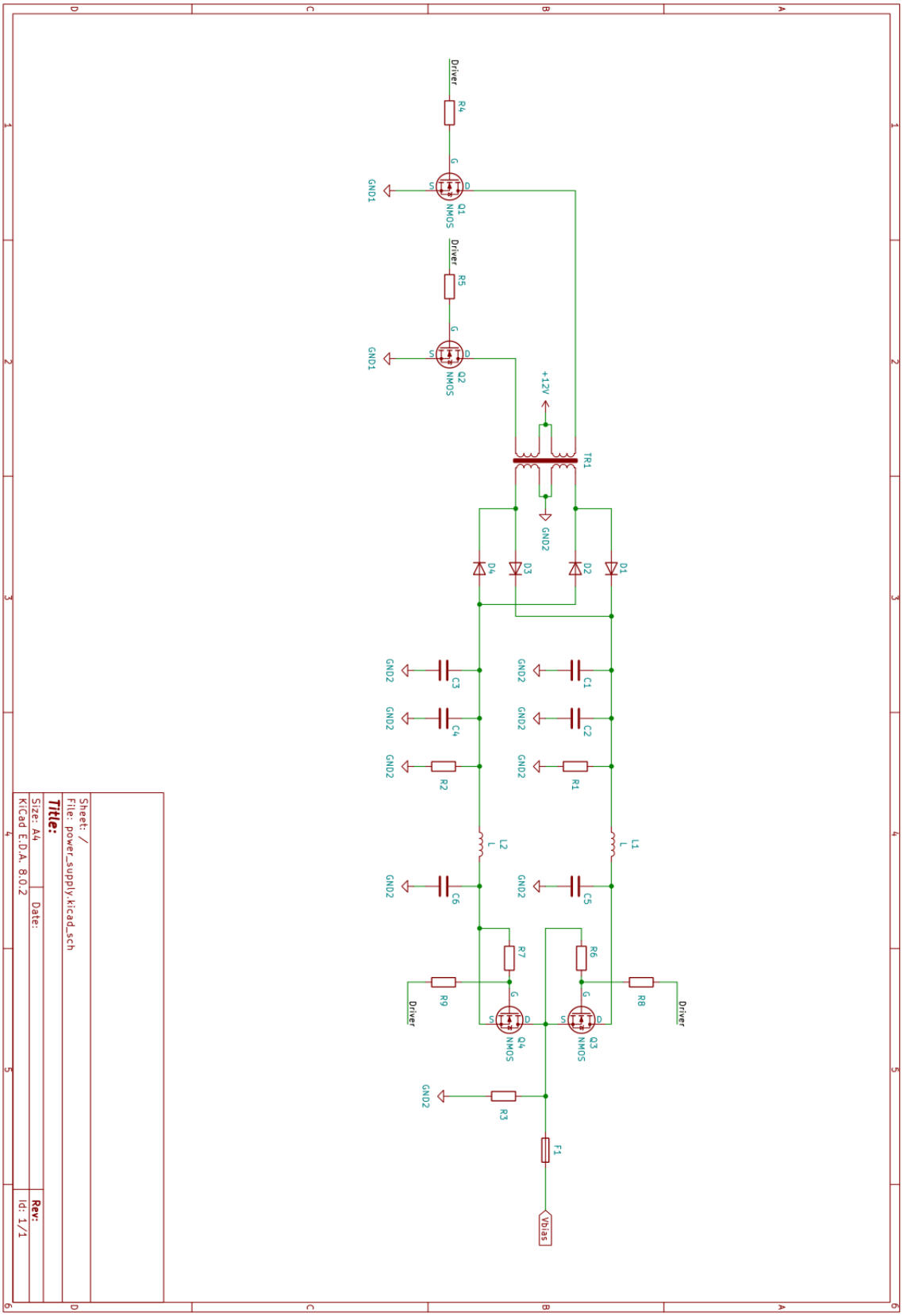

Figure 5.24: Circuit schematic proposed.

Chapter 6

Conclusions

The work done so far was aimed to analyze various aspect of the diagnostic system and to introduce, by components characterization and simulations, the much larger topic, that is the entire chain of development of custom-made diagnostic systems. Even though the results obtained are satisfying and point out few, easily solvable issues, the analysis performed needs to be further deepened and expanded so as to have a full characterization of the analyzed system and of other, not yet introduced, diagnostic systems. This effort, however, can result in the continuation of studies and research, which can be the subject of a PhD thesis. In the following paragraphs are exposed the conclusions reached through the analysis of the described system, i.e. EPICA.

6.1 Digital-To-Analog acquisition system

Even though this system was designed relying on the experience gained with previous experiments (such RFX and SPIDER), the design was completely renewed thanks to the introduction of isolated ADCs. This latter components allowed for a less complex design, while reducing cost, development time and space management. Moreover, the decision to implement a custom-made DC/DC converter instead of relying on bulky and off-the-shelf power supply reduced the amount of space and cost, especially when the number of probes is high, as in this case. The keynote of the ongoing discussion is weather the system will behave as expected from the simulation or not, when it comes to test the first prototypes. Few important things weren't taken into account:

- Power supply switching noise, generated by the transistors during their operation, will generate electromagnetic fields that will propagate using the board itself as a propagation medium. Having random spikes not accounted for and an unpredictable background noise is something that has to be avoided, if the quality of the measure and the reliability of the system are to be preserved.
- Being the probe's environment prohibitive for this kind of electronic, usually the conditioning and acquisition system is placed far enough and the probes are connected to it through a transmission line. This latter is quite difficult to deal with and the signal can be affected by reflection distortion. In addition the line act as an antenna, able to pick up noise coming from all around the environment.
- Surrounding environmental noise generally are those of the power line fed to electronic. In addition to those, other sources coming from other apparatus working placed nearby the system may affect the system itself.

All this not-so-foreseeable factors will certainly affect the measure, but it will be through a dedicated and thorough analysis that this aspects will be fully characterized and the system will be improved accordingly. In addition, also the implementation of the SOM and all the digital like the optimization of the FIR filters for the ADCs, the proper control of the biasing switching

converter nad possibly the real-time signal analysis of the acquired probe characteristics are relevant elements worth of further developments.

6.2 Biasing power supply

The characterization done so far only took in account the transformer, which is the core of the system, since it allows the conversion from small to high voltage. Nevertheless, there are other important things to consider.

- The switching noise generated by the transistor can, as explained in the previous section, generate interference, thus creating a model to be implemented in the simulations could be a first solution to at least estimate the impact on the measure.
- The model of the transformer takes into account marginal effects of the physics behind and can be further developed also by characterizing the ferromagnetic core.

Developing a DC/DC converter while complying with strict constraints in term of noise and EMI is no easy task, but can be achieved through a thorough analysis of the prototype and consequent improvements.

Bibliography

[1] https://it.wikipedia.org/wiki/Fusione_nucleare

[2] https://en.wikipedia.org/wiki/Lawson_criterion

[3] ONGENA, Jozef, et al. Magnetic-confinement fusion. Nature Physics, 2016, 12.5: 398-410.

[4] BODIN, H. A. B. The reversed field pinch. Nuclear Fusion, 1990, 30.9: 1717.

[5] MEYER-TER-VEHN, Jürgen; ATZENI, Stefano; RAMIS, Rafael. Inertial confinement fusion. Europhysics news, 1998, 29.6: 202-205.

[6] MENDEL JR, Clifford W.; SCHAMILOGLU, Edl. Plasma diagnostic techniques. the Encyclopedia of Physical Science and Technology„ 2002, 12: 391.

[7] Chen, Francis F. "Langmuir probe diagnostics." IEEE-ICOPS Meeting, Jeju, Korea. Vol. 2. No. 6. 2003.

[8] Chen, Francis F. Introduction to plasma physics and controlled fusion. Vol. 1. New York: Plenum press, 1984.

[9] Hutchinson, Ian H. Principles of plasma diagnostics. Plasma Physics and Controlled Fusion, 2002, 44.12: 2603-2603.

[10] Powell, Jason. "An Analytical Approach to Modeling Spacecraft Potentials in SPICE." (2021).

[11] Vedder, John D. "Simple approximations for the error function and its inverse." American Journal of Physics 55.8 (1987): 762-763.

[12] *The ITER CODAS conceptual design*, Lister, JB and Farthing, JW and Greenwald, M and Yonekawa, I, 2007

[13] LIU, Guoming; MAKIJARVI, Petri; PONS, Nicolas. The ITER CODAC network design. Fusion Engineering and Design, 2018, 130: 6-10.

[14] Liu, Guoming, Petri Makijarvi, and Nicolas Pons. "The ITER CODAC network design." Fusion Engineering and Design 130 (2018): 6-10.

[15] Marconato, Nicolò, et al. "Accurate magnetic sensor system integrated design." Sensors 20.10 (2020): 2929.

[16] Bonotto, Matteo, et al. "Design and analysis of halo current diagnostic for RFX-mod2." IEEE Transactions on Plasma Science 50.11 (2022): 4096-4101.

[17] Baruzzo, Matteo, et al. "Conceptual design of DTT magnetic diagnostics." (2019).

[18] Spagnolo, Silvia, et al. "Final design of electrostatic probes for MITICA beam line components." Fusion Engineering and Design 166 (2021): 112265.

[19] Spolaore, Monica, et al. "Design of a system of electrostatic probes for the RF negative ion source of the SPIDER experiment." Journal of Physics D: Applied Physics 43.12 (2010): 124018.

[20] Witulski, A. F. (1995). Introduction to modeling of transformers and coupled inductors. IEEE Transactions on Power Electronics, 10(3), 349-357.

Acknowledgments

I could say that everything I achieved so far its all my own making. I could say the credit for all the obstacles I've ever overcome is mine alone. I could say all this sort of things and, perhaps, maybe stretching things up a bit, everyone could believe me. But that would not be the truth. It would be a lie. Every single word involving "I" would deceive the reality of things. The truth is that I could never have come so far without the help of the people that were with me at the beginning of my journey and without the help of the people I met throughout it.

In the first place, I wish to thank my mother Michela, my father Gualtiero and my sister Greta. They always managed to keep me on the right path, even though I was no saint and I gave them a little bit of a hell. To them I owe what I've become and what I could ever be in the future.

I want to thank also my uncle Luca, my aunt Federica, my uncle Alberto, my grandfather Lino, my grandmother Vanda, my grandfather Gabriele, my grandmother Annemì and my cousins Anna and Emma. They've always supported me over these years and they will forever have my gratitude, since there is nothing I can do to pay my debt.

Finally, I want to thank Matteo (Zamu), Stefano (Shte), Pietro (Piv), Valentina (Vale), Silvia (Sissi), Giulia, Giulia (Ciurni), Beatrice (L'imperatrice), Francesca (FradB), Federica (Fede), Michele, Alessandro (Shole), Alessandro (Zago), Andrea, Andrea, Carlo (DinoCarlo), Lorenzo (Lollo), Angelo, Chiara, Chiara, Claudia, Emiliano (Eiaaanoo), Enrica, Giuseppe (Beppe), Federico, Filippo (Fil), Francesco (Frado), Houssine (Houss), Federico (Il Griso), Lucia, Mario, Otello, Luca (Quaglia), Raffaele, Serena, Michele (Vegetables Hat), Francesco (Ciccio), Alice and Francesca (FradM). To them I owe most of the smiles and moments of happiness I had in the last years.

I want to thank also the people at Consorzio RFX that helped me during the internship and the writing of the thesis, in particular I want to thank my advisor, prof. Nicolò Marconato, and my tutor, Dr. Roberto Cavazzana.